NOTE TO USERS

uOttawa

L'Université canadienne
Canada's university

FACULTÉ DES ÉTUDES SUPÉRIEURES ET POSTOCTORALES

uOttawa

L'Université canadienne
Canada's university

FACULTY OF GRADUATE AND POSDOCTORAL STUDIES

Ronald Millett
AUTEUR DE LA THÈSE / AUTHOR OF THESIS

M.A.Sc. (Electrical Engineering)
GRADE / DEGREE

School of Information Technology and Engineering
FACULTÉ, ÉCOLE, DÉPARTEMENT / FACULTY, SCHOOL, DEPARTMENT

Design of an SOA-based Integrated Optical Switch

TITRE DE LA THÈSE / TITLE OF THESIS

T. Hall
DIRECTEUR (DIRECTRICE) DE LA THÈSE / THESIS SUPERVISOR

CO-DIRECTEUR (CO-DIRECTRICE) DE LA THÈSE / THESIS CO-SUPERVISOR

EXAMINATEURS (EXAMINATRICES) DE LA THÈSE / THESIS EXAMINERS

J. Armitage

P. Berini

Gary W. Slater
LE DOYEN DE LA FACULTÉ DES ÉTUDES SUPÉRIEURES ET POSTDOCTORALES /
DEAN OF THE FACULTY OF GRADUATE AND POSTDOCORAL STUDIES

Design of an SOA-based Integrated Optical Switch

Ronald Millett, B.Eng

Thesis submitted to the
Faculty of Graduate and Postdoctoral Studies
in partial fulfillment of the requirements
for the M.A.Sc. degree in Electrical Engineering

July 2005

Ottawa-Carleton Institute of Electrical and
Computer Engineering
School of Information Technology and
Engineering
University of Ottawa

Your file Votre référence
ISBN: 0-494-11354-5
Our file Notre référence
ISBN: 0-494-11354-5

I. Abstract

This thesis describes and validates the design of an optical switch that uses a vertically-integrated active/passive waveguide in an InP-based heterostructure. The goal was to design a monolithically integrated proof-of-concept 2x2 switch for use in a reconfigurable optical add-drop module (ROADM). The 1x2 building-block used for this switch consists of a passive 3dB power splitter with two semiconductor optical amplifiers (SOAs) incorporated into each of the output arms. The major contributions are an integrated 3dB power splitter design derived from a validated general design procedure based on a reductionist approach, active waveguide modeling based on evanescent coupling to a weakly-confined SOA region for the switch function, and preliminary layout designs of 2x2 and 4x4 switch fabrics. The performance of the switch was determined through finite-element analysis using FEMLAB, based on material simulations performed using OptiHS, employing post-processing in MATLAB, and validated with beam-propagation analysis using OptiBPM.

II. Acknowledgements

This research was performed at the School of Information Technology and Engineering (SITE), at the University of Ottawa, from January 2003 to August 2005. I am most grateful for the mentoring and daily support of Dr. Henry Schriemer, the supervision of Dr. Trevor J. Hall, further guidance and encouragement by project manager Mirek Florjanczyk (SITE) and the support of MetroPhotonics personnel Valery Tolstikhin, Adam Denesmore and Kirill Pimenov. I would also like to thank my colleagues Jason Taylor and Xia Zhang for their assistance with portions of this research, and the other members of my research group for general conversations.

Financial assistance was provided by the Canadian Institute for Photonic Innovations, National Capital Institute of Telecommunications, NSERC, MetroPhotonics Inc., and the University of Ottawa.

Finally, I would like to thank Holly Smith and my family who have given me so much encouragement and support over the course of my studies.

III. Contents

IV. List of Tables

V. List of Figures

VI. List of Acronyms

ASE – Amplified Spontaneous Emission

BPM – Beam Propagation Method

DOS – Digital Optical Switch

DWDM – Dense Wavelength Division Multiplexing

MMI – Multimode Interference

MOM – Modal Overlap Method

PDL – Polarization Dependent Loss

PLC – Planar Lightwave Circuitry

ROADM – Reconfigurable Optical Add-Drop Multiplexer

SMVI – Single-mode vertically-integrated

SOA – Semiconductor Optical Amplifier

TE – Transverse Electric

TIR – Total Internal Reflection

TM – Transverse Magnetic

1. Introduction

1.1. Technology application and approach

A recent market study has shown that the sales of reconfigurable optical add-drop module (ROADM) enabled equipment in 2004 totaled $100 million, and that revenue is expected to further increase by 81% in 2005 [1]. There are now dozens of companies involved in ROADM manufacture, from established corporations such as JDS Uniphase and DuPont to startups such as Metconnex and MetroPhotonics. Why has the demand for ROADMs grown so substantially? To understand the answer it is necessary to first explain the fundamental operation of ROADMs, and the significant improvement they offer over previous technology.

Dense wavelength division multiplexing (DWDM) allows the complete bandwidth of an optical fiber to be exploited by carrying multiple signals at different wavelengths that do not interfere with each other as they propagate down the optical fiber. The use of DWDM has greatly increased the carrying capacity of optical fiber. Figure 1 shows the architecture of a typical DWDM fixed optical add-drop network node. First, a signal coming from the west is demultiplexed, in this case into four wavelength channels. Two wavelengths are sent directly through the node and the other two wavelengths are dropped. These wavelengths may be regenerated using optical-electrical-optical (OEO) conversion, or they may be sent directly to subscribers. The two added channels, consisting of either a new or a regenerated signal, are multiplexed with the two through channels and sent to the output.

The key weakness of this design is a lack of flexibility. If there is a break in this point-to-point link, or if it is desired to send information to a different destination (for instance, if the $\lambda 3$ channel no longer needed to be

dropped at this node), then it would be difficult to reroute a wavelength channel using this architecture. Rerouting would require labor-intensive manual reprovisioning that at best would be costly, and at worst could interrupt service.

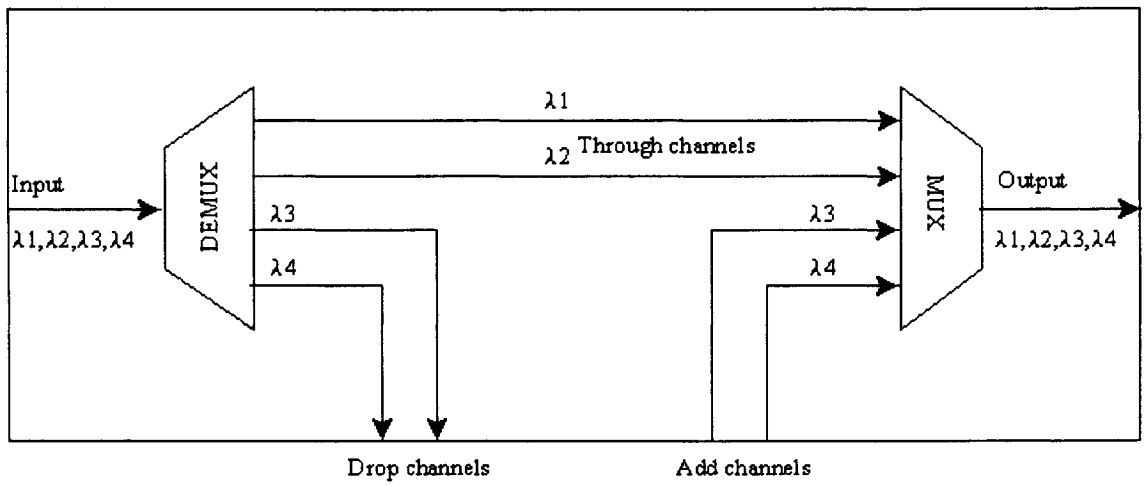

Figure 1 Fixed optical add-drop multiplexer network node configuration

With networks incorporating ROADM devices, it is possible to add or drop wavelength channels individually and dynamically at each network node. Each input channel can be added, dropped, or passed through the network node entirely in the optical domain, without costly OEO conversion. This flexibility will allow network operators to add or reduce capacity wherever it is required, in effect dynamically provisioning channels to ensure maximum network efficiency. It is no longer necessary to maintain a fixed link between two points if there is only an intermittent flow of information between them, or to have a fixed link with insufficient bandwidth.

It is easy to see the improvement in efficiency that is possible by using a ROADM architecture. However, it is only recently that ROADMs have begun to be deployed in significant numbers. One of the reasons for

this is the complicated nature of the ROADM itself. Figure 2 shows the functionality of a possible ROADM network node architecture. The incoming optical signal is first demultiplexed into its constituent wavelengths. These channels are then sent to an optical cross-connect, consisting of a series of optical switches. Finally, the output wavelengths are multiplexed and sent out to the next node of the optical network.

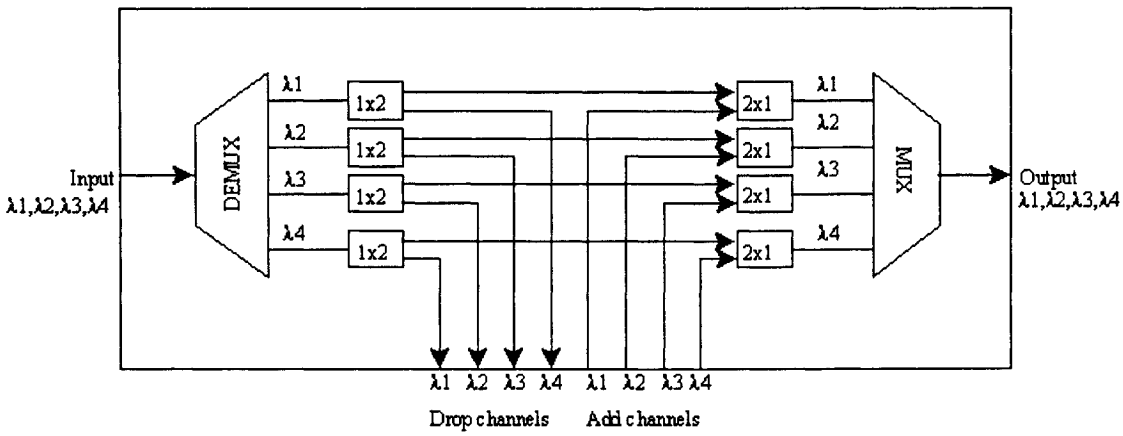

Figure 2 Reconfigurable optical add-drop module (ROADM) network node configuration

It can be seen from Figure 2 that optical switches are an integral part of a ROADM design. These switches must allow any input port to connect to any unused output port, regardless of whatever connections may have already been made. This is known as a *nonblocking* condition and will be discussed further in Section 5 of this thesis. A reliable, low-loss, and easily manufacturable method of switching optical signals is crucial for any modern ROADM design.

The goal of this research was to develop an integrated optical switch using a single-mode vertically-integrated (SMVI) active/passive layer structure that could potentially be used in a ROADM device. Initially a

1x2 switch was developed. Using this building block, 2x2 and 4x4 nonblocking switching fabrics can be created, and there is potential to create switches with an even higher number of ports (i.e., 2n x 2n).

An important trend in optical components is towards increasing integration. Many systems and devices that in the past would have been implemented using separate bulky optical components connected by lossy optical cables can now be manufactured on a single wafer. The advantages of this approach are obvious, as is evident from the success of electronic integrated circuitry. Integrated devices are much smaller, more easily manufactured, and cheaper when compared to discrete components.

There are two main types of integration: hybrid and monolithic. In hybrid integration, components are made on separate wafers and then combined into a single packaged device. In monolithic integration, all the optical components required are combined on a single wafer and fabricated at once. Hybrid integration tends to be more useful for complex custom devices. Each component of the hybrid-integrated system can be tested and optimized separately before they are combined together. It is easier to implement a complex system in such a piecewise fashion, and the savings in packaging costs can be considerable. However, hybrid integration still requires the labor-intensive step of combining each separate component together with fiber. This increases the cost and time to market of hybrid devices. In contrast, monolithically integrated devices have all interconnects included by design. It is also much easier to do large-volume, low-cost manufacturing of standard, simple devices without the need to perform numerous fiber interconnections. However, as systems become more complex, with a higher number of functions, it becomes increasingly difficult to achieve a reasonable manufacturing yield using the current immature monolithic integration technologies, and it again becomes advantageous to be able to separately test and optimize

components. It is probable that hybrid and monolithic integration will continue to coexist for the foreseeable future, and the choice between them will depend upon the application being considered. Since our switch design is relatively simple, there is a clear advantage in implementing it using monolithic integration, and this is in fact the approach we will take in this thesis.

1.2. Thesis Outline

This thesis begins in Section 2 with an overview of integrated optical switching. General optical waveguide properties are described, and the specifications required for our switch are given. Next is a comprehensive review of the current state-of-the-art in integrated optical switching geometries. The switch technologies are compared, and the SOA-based design is found to be the one most suitable for this application. Section 3 deals with the design of the integrated 3 dB power splitter. The Y-branch design is chosen from among the current integrated splitter technologies, including the MMI and directional coupler. A modal overlap design method is used to realize this splitter design, after first being validated with a simple silica buried-core waveguide material system. In Section 4, the active waveguide used for the SOA region of the switch is modeled. Through heterostructure analysis using OptiHS [2] and finite-element analysis using FEMLAB [3], the gain or absorption of a length of this section at various injected carrier densities is determined. Section 5 describes potential layouts for nonblocking 2x2 and 4x4 optical switches. Finally, the switch performance is evaluated and directions for possible future work are discussed in Section 6.

1.3. Summary of Contributions

This thesis provides contributions to the field of integrated optical switching and device design. More specifically, there are four main contributions:

- A comprehensive review of current state-of-the-art integrated switching technologies. This review stimulated our development of an efficient design method that was capable of generating a cost-effective and manufacturable switch architecture that satisfied our technical specifications.
- A new integrated optical switch design incorporating the vertical integration of active and passive components. The fact that the switch is monolithically integrated means that it can be combined with other devices on a single multi-functional chip to perform more complex processes, yet is still simple to manufacture. The design also features a minimal loss and a high extinction ratio, primarily due to the high absorption of the SOA waveguides when reverse-biased.
- The description of the Modal Overlap Method, a method capable of designing optimal and easily manufactured Y-branch power splitters with minimal computational resources. This method was successfully applied to the complex multilayer ridge waveguide used in the vertically-integrated system to design a low-loss power splitter.
- Modeling of the SOA regions of the switch using a combination of heterostructure material analysis using OptiHS and finite-element analysis using FEMLAB.

2. Integrated Optical Switching Overview

2.1. Introduction to Optical Waveguiding

An optical waveguide is used to confine light and direct it along a desired path of propagation. In this thesis it is assumed that propagation occurs along the z-axis, while the x-axis and y-axis are in the transverse direction. A common example of a waveguide is a fibre-optic cable. A typical optical fibre cross-section has a central core region surrounded by a lower-index cladding region. For a sufficiently large refractive index difference between the core and the cladding, total internal reflection will occur and the light will be confined in the core region. As long as there are no sharp bends in the fibre the light will continue to propagate along its length.

In integrated photonic devices, it is more difficult to fabricate optical waveguides that possess the circular symmetry of fibre-optic cables. The epitaxial manufacturing processes used in integrated devices lend themselves instead to planar optical waveguides. A *buried-core waveguide* (shown in Figure 3) is analogous to fiber-optic waveguides, and consists of a high-index (n_2) rectangular core surrounded by a lower-index (n_1) cladding region. The refractive index contrast of the buried core waveguide is quantified by the dielectric contrast, Δ, given by:

$$\Delta = \frac{n_2^2 - n_1^2}{2n_2^2} . \qquad [1]$$

The larger the delta value, the greater the index contrast between the core and cladding. A higher index contrast means a greater confinement of the optical mode in the waveguide.

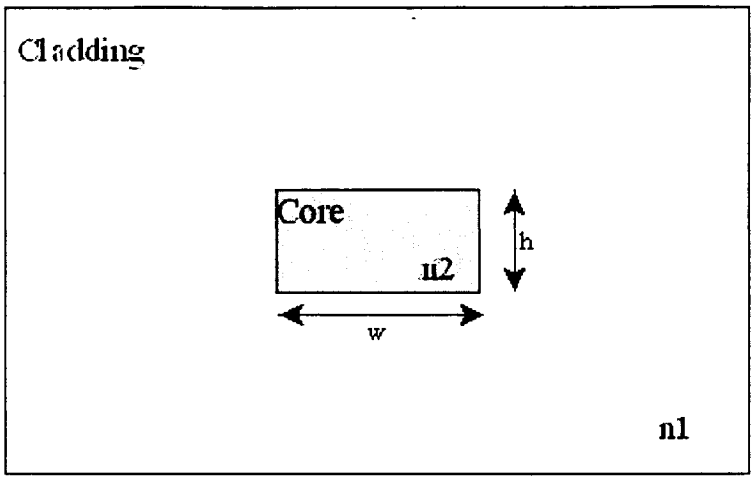

Figure 3 Rectangular buried-core waveguide

As the frequency of the light entering a waveguide is increased, additional optical modes will appear. This is a common feature of all optical waveguides, and it is useful to describe this in general terms, independent of any specific waveguide structure. What is needed is a metric for this property that allows different waveguides to be compared with each other. The *normalized frequency*, V, defined for a buried-core rectangular waveguide of height, h, and a free-space wavelength of λ, is the first general metric:

$$V = \frac{\pi h}{\lambda}\sqrt{n_2^2 - n_1^2} \quad . \qquad [2]$$

The second is the *normalized propagation constant*, b. Each optical mode supported by a waveguide has an eigenvalue associated with it, known as the propagation constant, β, that describes how the mode propagates in the z-direction. The *effective index* of an optical mode is given by $n_{eff}=\beta/k$, where $k=2\pi/\lambda$ is the free-space wave number. The effective index is the refractive index that would be experienced by a plane wave propagating in the waveguide along the z-direction at the free-space wavelength. Since the propagating optical mode of a rectangular waveguide must be confined

by the core region in a buried-core waveguide, the condition $n_1 \leq n_{eff} \leq n_2$ must be satisfied. The frequency where the lower boundary of this condition occurs is known as the *cutoff frequency* of the mode. If the optical frequency is lower than the cutoff frequency of a particular mode, then it will be a radiation mode, and hence will not propagate in the waveguide. The normalized propagation constant is related to the effective index, n_{eff}, the core index, n_2, and the cladding index, n_1, by the equation [4]:

$$b = \frac{n_{eff}^2 - n_1^2}{n_2^2 - n_1^2} . \qquad [3]$$

Using the normalized propagation constant, the cutoff condition occurs when b=0, and guided modes occur when $0 \leq b \leq 1$.

Using these two parameters, V and b, it is possible to construct a dispersion curve that shows at what frequencies modes occur in an optical waveguide, permitting direct comparison among different waveguide geometries. Using a finite-element approach that will be described in more detail in Section 3, a dispersion curve for a buried-core silica waveguide with a height, h, of 6μm is shown in Figure 4. This curve is identical to the one found in [4], thus validating our finite-element mode-solving technique.

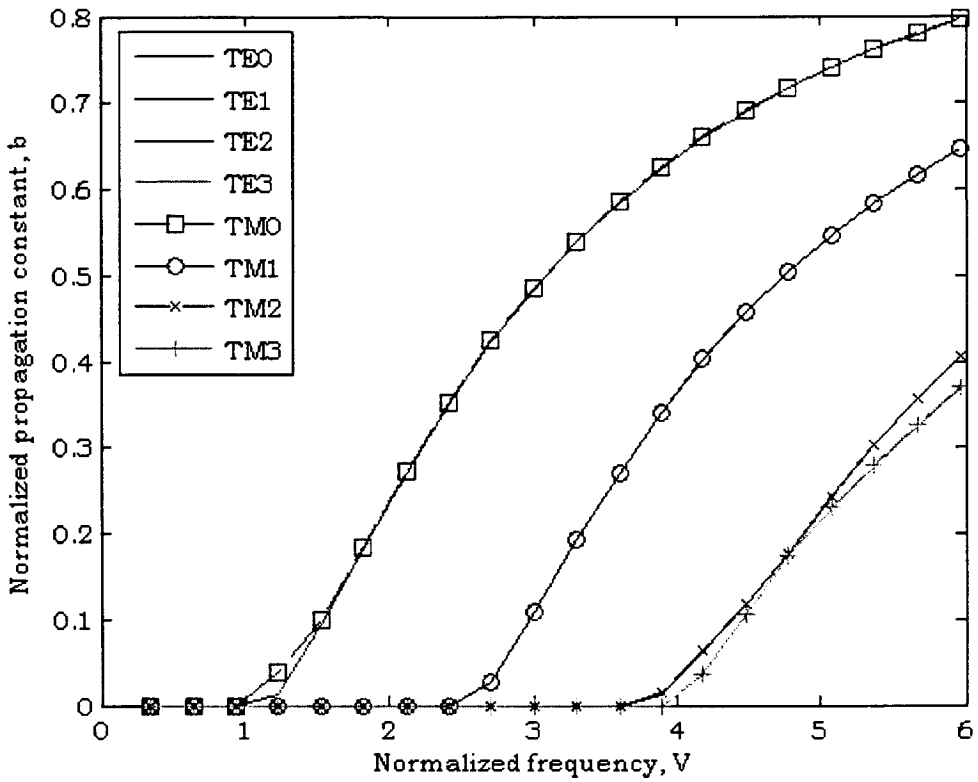

Figure 4 Dispersion curves of a buried-core silica/silicon waveguide, for n_1=1.445, n_2=1.455

Another common planar optical waveguide geometry is the *ridge waveguide.* In a ridge waveguide, shown in Figure 5, the majority of the fundamental optical mode is vertically confined in the high-index core layer, located just underneath the ridge. The horizontal confinement of the mode is provided by the ridge, which in turn has a higher refractive index than the surrounding upper cladding. In Figure 5, the lower cladding and ridge are shown as having the same refractive index (n_1), but this need not be the case in general. All that is required is that the ridge and lower cladding (or substrate) refractive index be lower than the core refractive index, and that the upper cladding refractive index (n_0) be lower than both. Often the upper cladding is simply air, with a refractive index of 1. Since

the propagation modes of a ridge waveguide are almost entirely in the ridge,

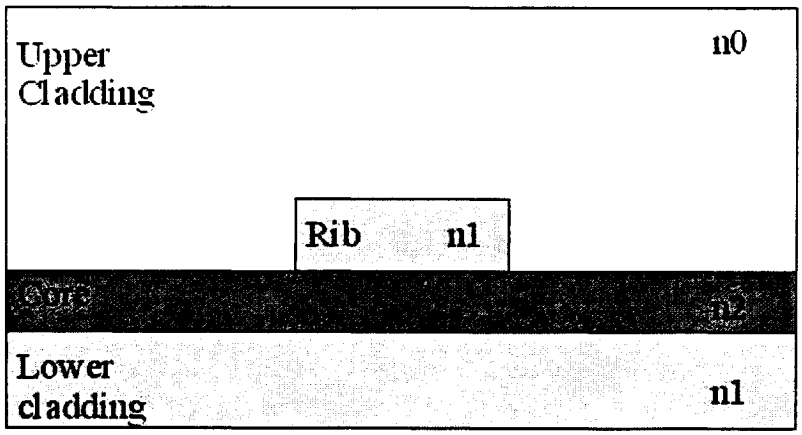

Figure 5 Ridge/Rib waveguide geometry

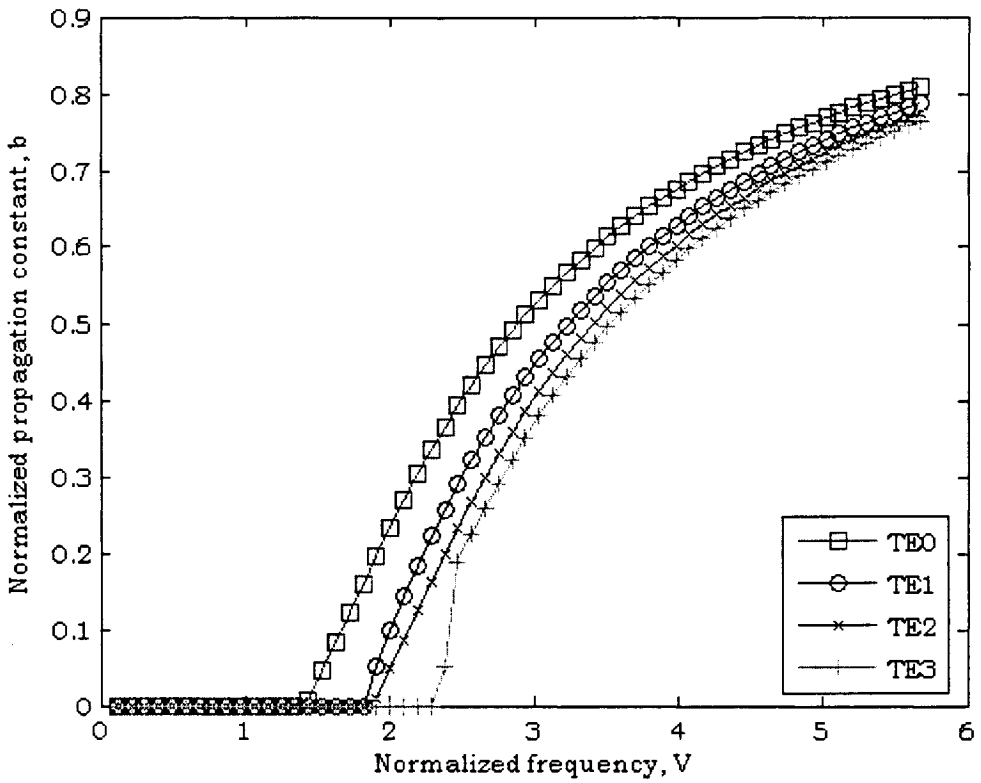

Figure 6 Dispersion curves for a silica/silicon ridge waveguide, with n_0=1, n_1=1.445, n_2=1.455, and a ridge width=2 μm

core, and lower cladding regions, the range of the effective indices of propagating modes is roughly $n_1 \leq n_{eff} \leq n_2$, with the lower cutoff being slightly smaller than n_1. A plot of the dispersion curves of a standard silica-on-silicon ridge waveguide in air are shown in Figure 6.

In the *rib waveguide*, the same geometry as shown in Figure 5 is used, except now the refractive index of the rib layer is larger than the lower cladding and cladding, and larger or equal to the refractive index of the core layer. This has the effect of confining the mode within the rib.

Finally, the *diffuse waveguide*, as the name suggests, is a diffuse region of higher index that acts as a waveguide. It is created through methods such as ion-implantation.

2.2. Optical Modeling Basics

Our assessment of optical transport in the planar lightwave circuitry discussed in this thesis derives from two numerical modeling approaches – finite-element modal analysis and the beam-propagation method, which will be described in more detail in this section.

2.2.1. Finite-Element Analysis

Finite-element analysis is a general method that can be applied to the problem of determining the modal fields of complex waveguide structures.

To apply finite-element analysis to waveguide geometries, we begin with the source-free, homogeneous vector Helmholtz equation for the magnetic field, **H**:

$$\nabla^2 \mathbf{H} + k_0^2 \varepsilon_r \mathbf{H} = 0, \qquad [4]$$

where and $k_0 = \omega/c$ is the free-space wave number (with ω the angular frequency and c the vacuum speed of light), and $\varepsilon_r = n^2$ is the spatially-dependent relative permittivity (which may be complex).

To solve this problem using a finite-element analysis, the problem is first expressed using variational formulation. In the variational method, the solutions to an equation are not solved directly, but instead by finding the solutions that cause a related functional, F(ψ), to become stationary. The stationary condition is given by:

$$\frac{d}{d\varepsilon} F(\psi + \varepsilon\eta)\Big|_{\varepsilon \to 0} = 0 \qquad [5]$$

where ψ is the true solution of the functional (and therefore also of the original equation) and η is an arbitrary function. There are a number of functionals that can be applied to the vector Helmholtz equation with equal success [5-7], however, they are very complex expressions that will not be discussed in detail here.

A simpler example is the functional of the scalar Helmholtz equation. In the scalar equation, only one of the components of the magnetic or electric fields along the axes is determined. For the electric field, if a spatial dependence of $\mathbf{E}(\mathbf{r},t) = \mathbf{E}(x,y)\exp(-i\beta z)$ is assumed, the scalar Helmholtz equation will be

$$\nabla^2\phi + \left[k_0^2 n^2(x,y) - \beta^2\right]\phi = 0, \qquad [6]$$

where φ represents either the x or y component of the electric field. The functional for this equation can then be given by [4]:

$$I[\phi] = \frac{1}{2}\int_{-\infty}^{\infty}\int_{-\infty}^{\infty}\left[\left(\frac{\partial\phi}{\partial x}\right)^2 + \left(\frac{\partial\phi}{\partial y}\right)^2 - \left(k_0^2 n^2(x,y) - \beta^2\right)\phi^2\right]dxdy. \qquad [7]$$

For a complex problem such as finding the modal solutions of a rib waveguide, it is unlikely that a single, tractable analytical function can be found to satisfy the stationary condition for this functional. To simplify the problem, the finite-element method divides the computational domain into a set of contiguous triangles, or finite elements. In each triangle, a trial function (which in our case was linear, but could be of higher order) is defined with unknown coefficients. These coefficients are determined by iterating until the stationary condition, such as the one in Equation 7, is satisfied over the entire computational domain.

The variational formulation, if the functional is properly chosen, ensures that the solutions not only satisfy the Helmholtz equation, but also the boundary conditions specified for the problem. For the case of a buried-core waveguide (see Figure 3), it can be assumed either that the cladding is infinite in extent, or that it is embedded in another material (e.g. air) that is infinite in extent. A computational boundary that goes to infinity is obviously not practical for a numerical solution. For our simulations, the computational domain was bounded by a perfect electric conductor, such that at the external boundaries, the relation:

$$\mathbf{n} \times \mathbf{E} = 0, \qquad [8]$$

was satisfied. In this equation, **n** is the unit vector normal to the boundary. To ensure that the boundaries were not affecting the modal solution, we progressively increased the size of the computational domain until there was no change in the eigenvalue of the solution for larger domain sizes. The same process was used to optimize the number of finite elements used, as described in more detail for the rib waveguides of Section 3.3.2.

The great advantage of the finite-element method is its speed, and it is very accurate for simple two-dimensional problems. However, the finite-element method cannot easily be used to directly model waveguides where there are large variations in the dielectric profile in the z-direction. As will be seen in Section 3, this restriction can be alleviated in certain cases.

2.2.2. Beam Propagation Method

The beam propagation method (BPM) is one of the most commonly used techniques for modeling integrated optical devices [8-11]. The BPM is a relatively simple method that can be readily adapted to include most effects of interest (e.g. polarization, nonlinearities). It gives a fully three-

dimensional model of the propagation of an optical field through a device by assuming that the transverse components of the optical field vary slowly along the direction of propagation of the device.

To derive the BPM for the electric field, **E**, we begin with the time-harmonic wave equation:

$$\nabla \times \left(\mu_r^{-1} \nabla \times \mathbf{E}\right) - k_0^2 n^2 \mathbf{E} = 0, \qquad [9]$$

where it is assumed that n is a function of the spatial coordinates (x,y,z). Since in optical materials it is usually only the permittivity ($\varepsilon=\sqrt{n}$) that differs from vacuum level, with the permeability unchanged, we set $\mu_r=1$. We then apply the vector identity $\nabla\times\nabla\times = \nabla(\nabla\cdot) - \nabla^2$, to obtain:

$$\nabla^2 \mathbf{E} + k_0^2 n^2 \mathbf{E} = \nabla\left(\nabla \cdot \mathbf{E}\right). \qquad [10]$$

Since we will be assuming that the transverse components of the optical field change slowly compared to the longitudinal components along the direction of propagation, it makes sense to divide Equation 10 into separate transverse and longitudinal components. In this model we will assume, as is typically the case, that the z-axis is the direction of propagation and that the x- and y- axes are the transverse directions. Thus, we rewrite the two vectors, **E** and ∇ as:

$$\mathbf{E} = \mathbf{E}_t + \mathbf{z}E_z$$
$$\nabla = \nabla_t + \mathbf{z}\,\partial/\partial z, \qquad [11]$$

where **z** is the unit vector in the z-direction, $\mathbf{E}_t$ is the transverse component of the electric field, E_z is the component of the electric field along the z-direction and ∇_t is the del operator applied to the transverse components. These terms can be substituted into Equation 10, with only the transverse terms considered:

$$\nabla^2 \mathbf{E}_t + k_0^2 n^2 \mathbf{E}_t = \nabla_t \left(\nabla_t \cdot \mathbf{E}_t + \frac{\partial E_z}{\partial z} \right). \quad [12]$$

Assuming that no electric charge is present in the material gives the divergence equation:

$$\nabla \cdot \left(n^2 \mathbf{E} \right) = 0. \quad [13]$$

Equation 13 can then be divided into transverse and longitudinal components:

$$\nabla_t \cdot \left(n^2 \mathbf{E}_t \right) + \frac{\partial n^2}{\partial z} E_z + n^2 \frac{\partial E_z}{\partial z} = 0. \quad [14]$$

If we make the assumption that n, the refractive index, is slowly varying in the z-direction, then the second term in Equation 14 can be neglected. The divergence equation can then be substituted into the final term of Equation 12:

$$\nabla^2 \mathbf{E}_t + k_0^2 n^2 \mathbf{E}_t = \nabla_t \left[\nabla_t \cdot \mathbf{E}_t - n^{-2} \nabla_t \cdot \left(n^2 \mathbf{E}_t \right) \right]. \quad [15]$$

Using the chain rule, the right-hand side of Equation 15 can be simplified, and the first term can be divided into transverse and longitudinal components:

$$\nabla_t^2 \mathbf{E}_t + \frac{\partial^2 \mathbf{E}_t}{\partial z^2} + k_0^2 n^2 \mathbf{E}_t = -\nabla_t \left[n^{-2} \left(\nabla_t n^2 \right) \cdot \mathbf{E}_t \right]. \quad [16]$$

We now apply the slowly-varying envelope approximation to Equation 16, by dividing $\mathbf{E}_t$ into two terms [8]:

$$\mathbf{E}_t(x, y, z) = \boldsymbol{\varphi}(x, y, z) e^{-ikn_0 z}. \quad [17]$$

The first term, $\boldsymbol{\varphi}(x,y,z)$, is an envelope term that only varies slowly along the direction of propagation (z). The second exponential term (where n_0 is known as the reference refractive index) is more rapidly varying along the direction of propagation. Substituting Equation 17 into Equation 16, and eliminating the exponential term from both sides gives the paraxial vector wave equation:

$$2ikn_0\frac{\partial\boldsymbol{\varphi}}{\partial z} = \nabla^2\boldsymbol{\varphi} + k^2(n^2 - {n_0}^2)\boldsymbol{\varphi} + \nabla\left(\frac{1}{n^2}(\nabla n^2)\cdot\boldsymbol{\varphi}\right). \quad [18]$$

This equation is solved separately for the x and y components of the electric field:

$$\begin{aligned} i\frac{\partial\varphi_x}{\partial z} &= A_{xx}\varphi_x + A_{xy}\varphi_y \\ i\frac{\partial\varphi_y}{\partial z} &= A_{yy}\varphi_y + A_{yx}\varphi_x \end{aligned} \quad [19]$$

where the differential operators are given by:

$$\begin{aligned} A_{xx}\varphi_x &= \frac{1}{2n_0k_0}\left\{\frac{\partial}{\partial x}\left[\frac{1}{n^2}\frac{\partial}{\partial x}(n^2\varphi_x)\right] + \frac{\partial^2\varphi_x}{\partial y^2} + (n^2 - n_0^2)k_0^2\varphi_x\right\} \\ A_{yy}\varphi_y &= \frac{1}{2n_0k_0}\left\{\frac{\partial}{\partial y}\left[\frac{1}{n^2}\frac{\partial}{\partial y}(n^2\varphi_y)\right] + \frac{\partial^2\varphi_y}{\partial x^2} + (n^2 - n_0^2)k_0^2\varphi_y\right\} \\ A_{xy}\varphi_y &= \frac{1}{2n_0k_0}\left\{\frac{\partial}{\partial x}\left[\frac{1}{n^2}\frac{\partial}{\partial y}(n^2\varphi_y)\right] - \frac{\partial^2\varphi_y}{\partial x\partial y}\right\} \\ A_{yx}\varphi_x &= \frac{1}{2n_0k_0}\left\{\frac{\partial}{\partial y}\left[\frac{1}{n^2}\frac{\partial}{\partial x}(n^2\varphi_x)\right] - \frac{\partial^2\varphi_x}{\partial y\partial x}\right\}. \end{aligned} \quad [20]$$

Equations 19 and 20 represent a fully-vectorial BPM approach, where the two transverse components of the electric field are coupled and the propagating wave is hybrid. However, this coupling is usually very weak and can be neglected in many cases [8]. In this approximation, known as semi-vectorial BPM, Equations 19 and 20 are still used, except now the coupling terms are set to $A_{xy}=A_{yx}=0$. For our simulations, we performed initial tests on our waveguides using both the fully-vectorial and semi-vectorial formulation and found negligible difference between them. Since the semi-vectorial approach is significantly less computationally intensive, it was used for our BPM simulations.

To implement Equation 19, the finite-difference technique can be used to approximate all the differential operators. The continuous space is replaced by a rectangular lattice structure in the x,y, and z-directions. The initial field is found using a mode-solver for the waveguide structure, and Equation 19 and the finite-difference technique is used to find the electric field at each transverse plane (located at each point in the z lattice) along the waveguide.

BPM is capable of simulating three-dimensional waveguides with considerable variation along the direction of propagation. However, this thesis used finite-element analysis for the majority of the device simulations. The reason for this is that finite-element analysis is considerably less computationally intensive, and therefore faster, than BPM. The modal overlap design process that was used to design the integrated power splitter (described in detail in Section 3.2) relied solely on finite-element simulations, and was validated using BPM for a buried-core waveguide structure. This structure was used for rigorous verification since it was considerably less time-consuming to calculate BPM simulations of buried-core waveguide structures than the more complicated multilayer ridge waveguide (see Figure 7) used in the actual

design. However, the layout for the final design was also confirmed using BPM.

2.3. Waveguide & Material System – This work

The waveguide that was used in the design of the optical switch is a multilayer variant of the simple ridge waveguide. The layer structure of this waveguide is listed in Table 1, and shown in Figure 7. The upper cladding is assumed to be an epoxy material with a refractive index of 1.5. The additional layers are necessary to implement the vertically-integrated active/passive functionality. For example, layer 4, which is between the core region and the ridge, is n-doped, since in the active regions it will sit directly underneath the lateral n-contacts. The majority of the mode is confined underneath the passive ridge, in the core layer.

Number	Layer	Material	Refractive Index	Thickness (μm)
5	N contact II/ridge	InP	3.143948	0.6
4	N-contact I	InP	3.143948	0.25
3	Upper cladding	InP	3.173067	0.15
2	Device waveguide core	InGaAsP	3.23101	0.5
1	Lower cladding	InP	3.173067	1
0	Substrate	InP	3.173067	n/a

Table 1. Single-mode vertically-integrated passive waveguide layer structure

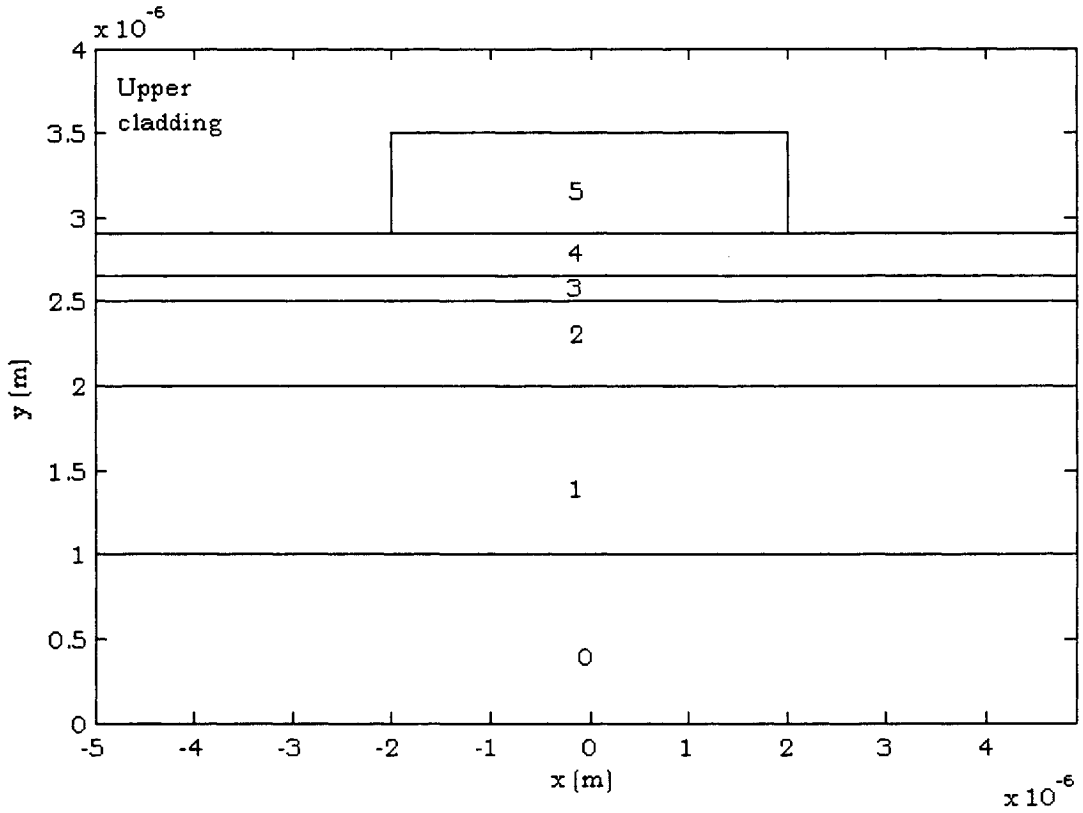

Figure 7 Passive waveguide geometry of the SMVI material system

One major advantage of this material system is that it requires only a single epitaxial step to fabricate. Figure 8 illustrates the basic steps of fabricating this type of vertically-integrated active/passive structure. All layers, active and passive, are first grown on an InP wafer. The lower layers are used for passive waveguiding and consist of an InP upper and lower cladding, a waveguide core layer of InGaAsP with a higher refractive index, and n-doped InP n-contact and ridge layers. The upper layers are used for active waveguiding, and consist of an InGaAsP active layer, and p-contact layers of varying levels of p-doping.

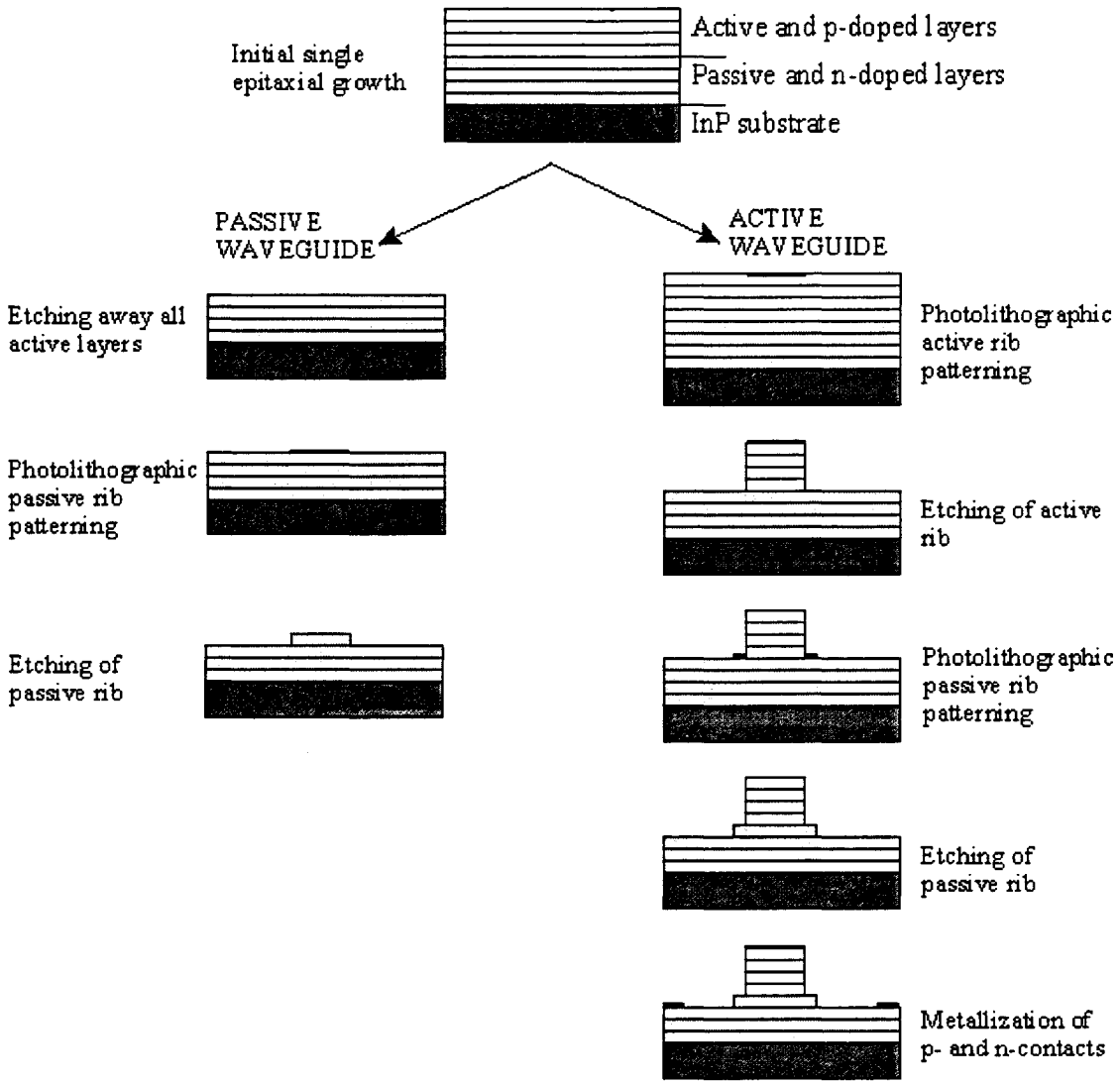

Figure 8 Fabrication of passive and active waveguides in the SMVI material system

Once the layers have been grown, they can be etched away according to what is required. For the passive regions of a chip, all of the upper active layers are first etched away. Then, a mask is used to lithographically define the geometry of the passive waveguide, and a ridge is formed in the n-contact layer to provide confinement of the optical mode. For active regions, the upper layers remain intact, and an active ridge is lithographically defined out of them as well as the n-contact layer in the

passive layer stack. The result, for the active region, is a p-i-n region formed by the upper p-doped layers, the active layer, and the n-doped layers that form the passive waveguide. Finally, metal contacts are added on either side of the ridge to form lateral n-contacts, and on top of the active ridge to form the p-contact.

In what we term the active waveguide, the mode is evanescently coupled to the active layers (see Figure 9), with most of the optical energy remaining within the passive layers. There is approximately 0.5-2% optical confinement in the active layer itself (see Figure 47). This low confinement in the active region means that the passive and active waveguides have very similar guiding properties, allowing light to propagate through the abrupt junction between the two waveguides with almost no coupling loss and back reflection, as will be confirmed later in Section 4.4. Under zero-bias, the active waveguide is absorbing. However, when carriers are injected through the metal contacts, the complex refractive index of the active layer is changed, which in turn affects the complex effective refractive index of the propagating mode. With a sufficiently high concentration of carriers, the imaginary portion of the effective refractive index goes to zero and the propagating mode experiences no loss traveling down the waveguide. This is known as the transparency point. If more carriers are injected, the mode will experience a gain. This carrier injection also affects the real portion of the refractive index. The effect of carrier concentration on the gain or loss of the active waveguide will be modeled in more detail in Section 4.

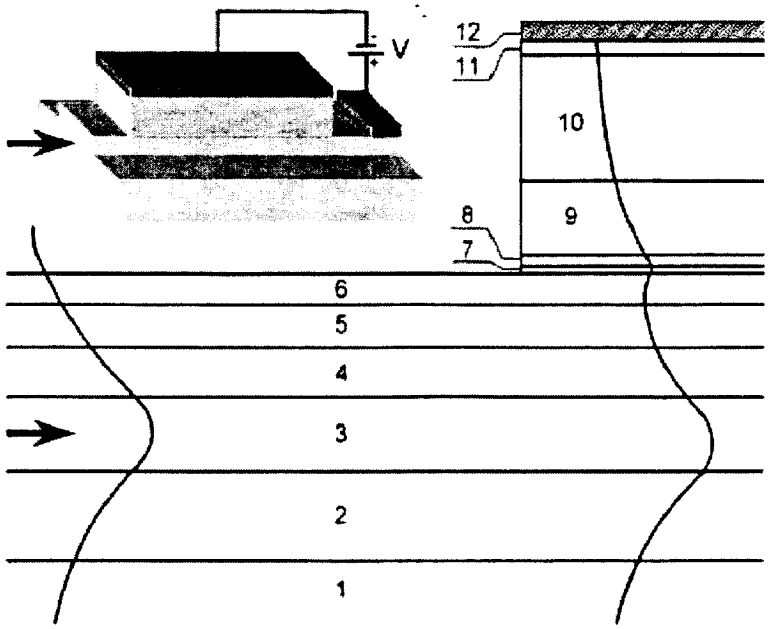

Figure 9 Evanescent coupling of the optical mode into the active layer in a vertically-integrated waveguide (adapted from [12], courtesy of Valery Tolstikhin)

The active region can be used not only as a gain region but also as a variable attenuator or photodetector. This multifunctionality can be exploited to create very useful monolithically integrated photonic subsystems. For example, an echelle grating multiplexer implemented using the passive waveguide can be combined with photodetectors and variable attenuators implemented with the active waveguide. In this design, a DWDM optical signal can be demultiplexed, have the optical power of each individual channel monitored and adjusted to ensure power equalization, and then multiplexed again into a single output signal [12]. This type of dynamic channel equalizer could be realized with a single compact design and be manufactured in a single epitaxial growth step.

2.4. Optical Switch Requirements for ROADM applications

The requirements for this optical switch, shown in Table 2, are based on the demands placed on network ROADMs and the SMVI InP/InGaAsP material system chosen [13].

Parameter	**Specification**
Excess Loss	< 1 dB
Crosstalk	< -30 dB
Polarization dependent loss	< 1 dB
Wavelength range	C-band (1530nm – 1565nm)

Table 2. Desired specifications for the integrated optical switch

- *Excess loss* refers to the optical loss experienced by light propagating through the entire length of the device, neglecting coupling losses due to fibre-waveguide mode mismatch. In an optical switch with multiple nodes there may be numerous distinct paths that light can travel from the input to the output. In this case the loss specification refers to the maximum loss that can be experienced for all paths between the input and the output.
- *Insertion loss* is the excess loss plus the coupling losses.
- *Crosstalk* is due to the undesirable coupling of a signal from one lightpath into another, and is an important measure of switch performance. The majority of system-level crosstalk is a result of poor switch extinction ratios. The extinction ratio of a switch is given by $r=P_1/P_2$, usually expressed in decibels, where P_1 is the optical power measured in a switch output when it is "off", and P_2 is the optical power measured in a switch output when it is "on". Another source of crosstalk is backreflections since it is possible for multiple reflections to be added to an output signal. If the crosstalk signal is of the same nominal frequency and coherent with the desired signal,

it is termed *homodyne crosstalk*; if it is of the same frequency but phase-incoherent, it is termed *homologous crosstalk*. Crosstalk that is uncorrelated in both frequency and phase to the desired signal is called *non-homologous crosstalk*. Our initial crosstalk goal is -30dB for this proof-of-concept design. Later designs using superior fabrication techniques will aim for values of crosstalk of less than -40 dB.

- *Polarization dependent loss (PDL)* occurs when different polarization states experience different losses (or gains) when propagating through a device. It is the difference between the highest and lowest insertion losses over all respective polarization states. In the passive regions it can be compensated for by reducing the birefringence of the optical waveguide. In active regions, strain is often deliberately added to the layers to reduce polarization dependence.
- *The wavelength range* of the device is the telecommunications window in which it would operate. In this case, the C-band (conventional-band) is chosen since it is a popular telecommunications band that encompasses the lowest loss wavelength of silica optical fibers at 1550nm [14].

2.5. Review of PLC-based Optical Switch Architectures

This section will describe the different types of integrated optical switches that have been developed, and rate their effectiveness for the current design problem. There are other switch architectures available, for instance, the micro-electromechanical switch (MEMS), but we will confine our discussion strictly to designs that can be implemented using our integrated semiconductor waveguide technology.

2.5.1. Mach-Zehnder Interferometric Switch

The Mach-Zehnder switch is based on the classic configuration of the Mach-Zehnder interferometer. In the interferometer configuration, a beam of light is split into two different paths. The light in each path travels a different optical path length, and is then recombined. The light in each path will have a different phase at the point when they are recombined, and an interference pattern will result. This interference pattern has been used, for example, to measure small variations in the length of two arms in an interferometer.

This geometry can be easily adapted for use as an integrated switch, as seen in Figure 10. An input waveguide is split into two paths using a 2x2 3 dB splitter. In one path the light passes through a regular waveguide of minimal attenuation. In the other path the light passes through a region of different refractive index, resulting in an optical path length difference of $\Delta n_{eff}L$ between the two arms, assuming the length of both arms is L and the effective refractive index difference is Δn_{eff}. If the difference in optical path length, and hence phase-shift - controlled through varying the refractive index in one sample arm - is chosen correctly, there will be constructive interference at the desired output port and destructive interference at the blocked output port, and the proper switching operation will be achieved. To switch to the other port, the refractive index of one of the paths is changed such that the constructive and destructive interference now occur at the opposite ports. The change in phase, $\Delta\Phi$, due to a change in effective refractive index, Δn_{eff}, in a waveguide of length L, at a vacuum wavelength λ, is given by:

$$\Delta\phi = \frac{2\pi}{\lambda}\Delta n_{eff} L \quad [21]$$

It can be seen from Equation 21 that the phase-shift in the variable refractive index arm, and hence the optical path length change required to achieve low-crosstalk switching, is wavelength dependent. This limits the efficaciousness of the Mach-Zehnder switch to a small band of frequencies, ideally to channel-specific designs.

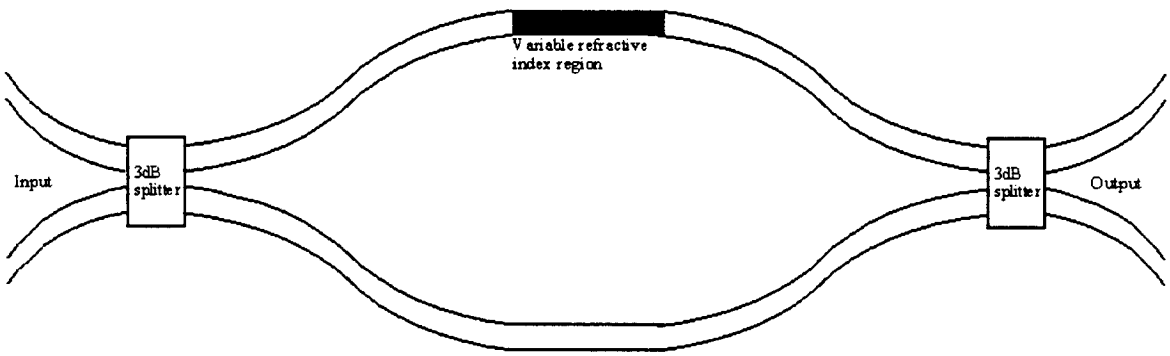

Figure 10 Mach-Zehnder interferometric switch

In 2003 Prasanth *et. al.* described a multiple quantum well phase-shifting region employing strain-balancing to effectively eliminate polarization sensitivity [15]. The quantum-confined Stark effect and carrier depletion effects were used to produce the refractive index change required to induce switching. Their investigation was purely theoretical, but simulations indicated that a cross-talk of -25dB, and polarization-insensitive operation was possible.

A version of the Mach-Zehnder switch by Maat *et. al.*, and published in 2002, incorporated two phase-shifting regions, one to perform the standard phase-shift, and the other to correct for small deviations in this phase caused mainly by variations in doping levels and layer thickness [16]. This design was able to achieve cross-talk values of ~-20 dB, an

insertion loss of 4 dB, and low polarization sensitivity within the pass region.

A state-of-the-art integrated Mach-Zehnder switch design has also been commercialized by Lynx Photonic Networks. These silica-on-silicon devices use thermo-optic effects to change the refractive index of the waveguide. They are capable of being used as power splitters, VOAs, and switches. These switches have been combined into 2x2, 4x4, and 8x8 cross-connects. The 4x4 nonblocking switch has an insertion loss of < 4dB, crosstalk of <-40dB, polarization dependent loss of <0.4dB, and a switching time of 2ms over either the L- or C-band [17]. However, the non-blocking 4x4 cross-connect now available has a large power consumption of 7W. Including the drive circuit, the total power consumption becomes 10W.

The Mach-Zehnder design is capable of offering low cross-talk and insertion loss, particularly in doped-glass PLC. It is exceeding challenging, however, to monolithically integrate active functionality in such a material system and therefore a hybrid approach is usually pursued. It is much more challenging to achieve the crosstalk and insertion loss specifications in active semiconductor material systems. It does, however, require considerably greater design sophistication, both in materials and geometry, to address polarization sensitivities, and to limit the wavelength-dependence to the purely interferometric. Since we desire broadband operation, and have a layer structure [12] constrained by additional integration requirements, the Mach-Zehnder switch geometry is not suitable for our purposes.

2.5.2. SOA-based Switch

An SOA-based switch (see Figure 11) splits the input waveguide into two outgoing paths using a 3 dB power splitter. In each of these two paths there is a semiconductor optical amplifier (SOA). In the waveguide to be blocked, the SOA is reverse-biased so as to attenuate. In the waveguide where the signal is to be passed, the SOA is adjusted for transparency, or possibly amplification, to offset the 3 dB loss from the splitter. The extinction ratio of such a device, and hence effectively its contribution to crosstalk, is directly controlled by the SOA attenuation, which is a function of the reverse-bias voltage and the length of the attenuating region. Detailed calculations of this can be found later, in Section 4.

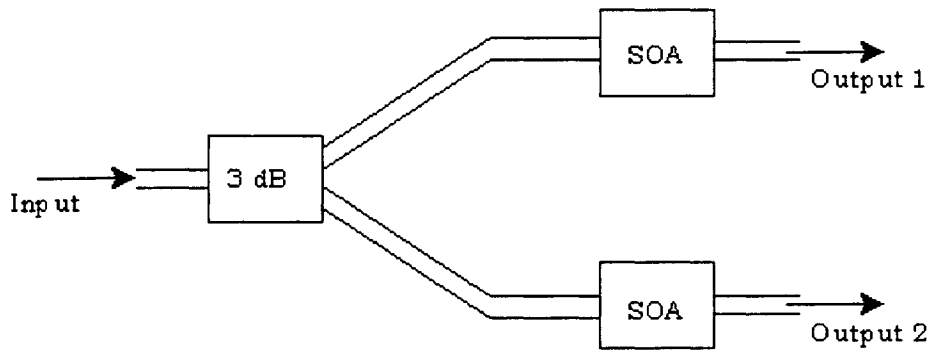

Figure 11 A simple 1x2 SOA-based switch

One example of a 2x2 SOA switch is the design of Burton *et al.* from 1993 [18]. This nonblocking 2x2 switch was constructed using 1x2 building blocks similar to the geometry that will be shown in Figure 48 of Section 5. The design was made more compact by using total internal reflection mirrors (TIR) designed to deflect light 90 degrees at various points within the device, and using right-angle waveguide crossings. This

design was implemented with amplifiers capable of generating 24 dB of gain when turned on, and absorption of 20 dB when turned off. This device had an overall insertion loss of 1 dB, however, mainly due to the low quality of the mirror facets. The mirrors also contributed to a polarization dependent loss of 1 dB, since the TM mode experienced a higher loss during reflection. This was slightly compensated by the fact that the TM mode experienced a higher gain in the amplifying SOA than the TE mode. The gain regions of this chip provided excellent amplification, and the losses of this design could be mitigated through higher-quality mirror facets. However, the monolithic integration used in this design required three separate growth steps, which is too unreliable and expensive to be commercially viable.

Further expansion of the SOA switch architecture was demonstrated by van Berlo *et al.* [19] in a nonblocking 4x4 switch, in which any one of the four input ports could be switched to any one of the four output ports, using the same geometry as shown in Figure 49 of Section 5. To obtain polarization independence, a high gain in the SOA regions and low active/passive coupling losses, the active regions are butt-joint integrated with regrown passive waveguides. This requires a complex, multiple-regrowth fabrication process that, similar to the Burton design mentioned above, is prohibitively expensive and low-yield. The gate switch matrix was designed to meet specifications of PDL < 1dB, insertion loss < 2dB, and crosstalk of < -40 dB. However, irregular regrowth during the complex fabrication process likely caused only 12 of the 16 possible optical paths to meet these specifications. The crosstalk varied widely, from -45dB to -17dB, depending on the lightpath measured, and not all possible optical paths were measured.

Saini *et al.* introduced a simple on-off switch based on their passive active resonant coupler (PARC) platform [20]. This requires mode

evolution from a purely passive waveguide to a wholly active waveguide, where the mode becomes strongly confined to the active region. This was subsequently integrated as a 1x2 switch [21] and then a 2x2 switch [22]. Due to the strong modal confinement, for an active length of 300μm, a maximum gain of about 22dB was achieved in forward-bias, and in reverse-bias a modulation contrast of 30dB for the cross state and 27.5dB for the bar state was attained. The SOA gain region, however, consisted of compressively-strained quantum wells that are highly polarization-dependent, and the device was only tested with TE polarization. The polarization dependent loss of the standard SOA-based design depends mainly on the operation of the SOAs themselves, and is challenging to resolve.

One drawback of this switch implementation is the increased spontaneous emission noise with SOA gain. This can degrade the input signal, especially if the signal passes through more than one cascaded SOA in a larger switch matrix. In contrast to the approach of Saini *et. al.*, the SOAs in our vertically-integrated active waveguide were designed to be polarization independent (at transparency, for this proof-of-concept design), insensitive to spontaneous emission noise, and highly integrable with other active functions.

2.5.3. Total Internal Reflection Switch

Total internal reflection (TIR) occurs when light is reflected at the interface between materials with a large refractive index difference. It is used to provide light containment in optical fibers, and can also be exploited to create an optical switch, as shown in Figure 12. Light that enters the lower arm of the device will normally pass to the upper arm (output1). To cause switching to occur, the refractive index of the middle region of the

device is increased until total internal reflection of the input light occurs, directing the light to the lower arm of the output (output2).

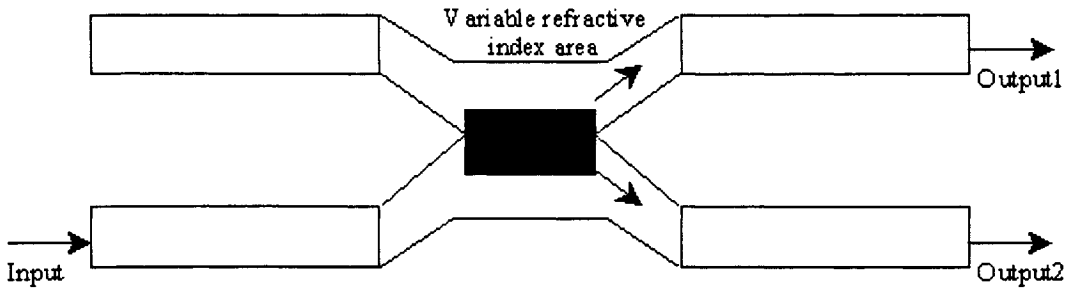

Figure 12 A 2x2 total internal reflection switch

TIR switches have been manufactured as far back as 1986, when Ishida *et al.* fabricated a polarization-insensitive device that had an insertion loss of < 2dB and -20dB of cross-talk, requiring 90mA of current [23]. To keep the refractive index change required low, it is desirable to increase the width of the waveguide and thus lower the modal confinement [24]. This results in undesirably high crosstalk values. In the recent design by Jiang *et. al.*, a photon-induced carrier effect was used to vary the refractive index at the center of an asymmetric Y-branch waveguide. The extinction ratio was measured to be 18dB in the cross state (e.g. when light is switched from the Input as shown in Figure 12 to Output1), and only 8dB in the bar state (e.g. when light is switched from the Input as shown in Figure 12 to Output2). In the low injection current design of Oh *et. al.* of 1994, while only 20mA of current was required, the crosstalk was -9.7dB [25].

The specific reason that such TIR switches are unsuitable for this particular application is the low (0.5-2%) confinement of the optical mode in the active layer of the active waveguide. This active layer is the only layer that experiences a significant change in refractive index with carrier

injection. This means that the index change required in this layer would have to be even larger than in typical TIR designs to cause total internal reflection of the input light. The large amount of index change required would be especially power-intensive and could potentially cause undesirable thermal and non-linear effects. For these reasons, the TIR geometry is not a suitable choice for this switch design.

2.5.4. Digital Optical Switch

The digital optical switch (DOS) is a promising architecture that has the potential for polarization and wavelength independent operation. The DOS has a Y-branch type of geometry with a variable refractive index region in the vicinity of the branching region (see Figure 13). When the variable index regions are unbiased, the switch acts as a power splitter, with the input mode propagating adiabatically down the waveguide structure and splitting into the two output regions. A refractive index change along either the top or bottom output waveguide in the modal evolution region (which begins when the output waveguides begin to separate) perturbs the mode such that light will then propagate into a single output waveguide [26].

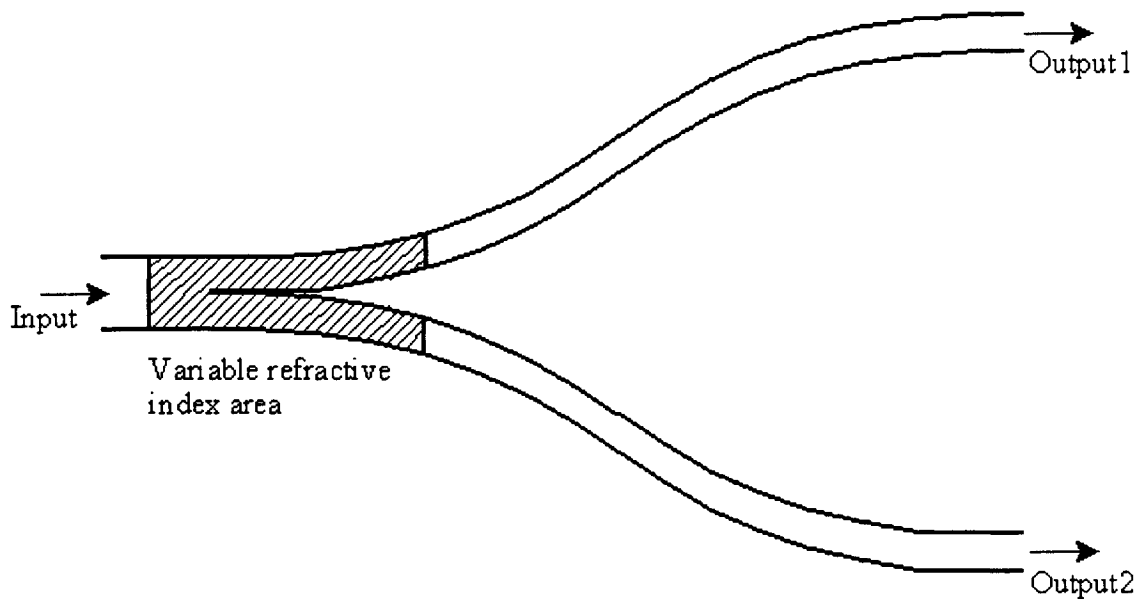

Figure 13 A 1x2 digital optical switch

The DOS of Sneh *et al.* is a typical example of this type of switch. Two straight output waveguides act as the variable index regions, using the electro-optic effect. The switch was implemented on an InP material system and required a 7V reverse bias to induce the refractive index change required using the quantum-confined Stark effect and the electrooptic effect. With this simple design, a cross-talk of -20dB was measured with a wide wavelength range of 45nm [27].

A more recent design minimizes the electrical current requirements of the design [28]. The biasing electrodes were shaped to follow the curved edges of the waveguides in the mode evolution region to more effectively guide light into each output arm. Using a 20mA switching current, a maximum switching contrast of 12dB was achieved with only TE polarization being tested.

The DOS requires adiabatic modal evolution, and, as can be seen in Figure 13, this requires an infinitely small separation between the output waveguides at the beginning of the mode evolution region. There will in practice be a finite minimum separation between the waveguides, creating a discontinuity. This will lead to potential mode mismatch excess loss since the mode is no longer adiabatically evolving at this junction.

As with TIR switches, another difficulty with this design is the refractive index change required to attain reasonably low optical power in the off-state lightpath (isolation) that can adversely affect the crosstalk. The necessary refractive index change is fairly high in designs where the mode is strongly confined in the index change region, but in the active waveguide we are using where there is only 0.5-2% confinement in the active layer, the amount of index change required is prohibitive, making this device unsuitable for our design.

2.5.5. Directional Coupler Switch

If two waveguides are placed close enough to one another so that their fields overlap, then light will be coupled between them. In optical switches or demultiplexers, this can lead to undesirable crosstalk between waveguides. However, like many phenomena that initially seem to be problematic, it is possible to exploit this effect to create useful devices.

In a directional coupler switch (Figure 14), two waveguides are intentionally brought near enough to each other for evanescent coupling to occur. The first symmetric and antisymmetric supermodes interfere either constructively or destructively depending on which waveguide is desired as the output. The interference is changed by varying the optical path length over which the interference occurs (the coupling length). This is done by inserting a variable refractive index region in one or both of the optical waveguides in this region.

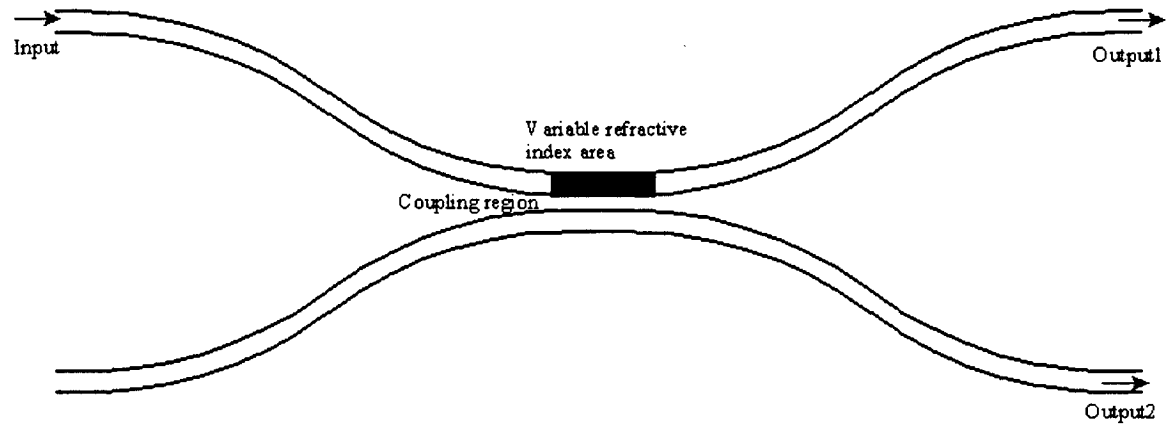

Figure 14 A 2x2 directional coupler switch

The coupling length, the length over which light is switched into either the upper or lower waveguide, is given by:

$$L_\pi = \frac{\pi}{\beta_0 - \beta_1}, \qquad [22]$$

where the propagation constants β_0 and β_1 are for the symmetric and antisymmetric supermodes. These correspond to the propagation constants of the TE0 and TE1 modes shown in the dispersion curves of Figure 6 for the case of a ridge waveguide (or also the equivalent TM modes). As can also be seen from Figure 6, the values of the propagation constants, β_0 and β_1, are highly wavelength dependent. Another difficulty is that the coupling length can be prohibitively long for effective directional coupler switching.

Crosstalk has typically been in the range of -15 to -30dB in directional coupler switches [29]. An early example of a polarization-

insensitive directional coupler switch design by Alferness, for example, achieved -23dB of crosstalk in both switching states [30]. An example of a more sophisticated directional coupler switch is the design of Mak *et. al.* from 1994. In this design, two additional coupling regions and four electrical contacts in the waveguide bends were added to improve the extinction ratio. This design was capable of a 36dB extinction ratio for both bar and cross states with a switching current of 50mA. It required a large length, however, of 16mm [29].

The directional coupler design can be used in more polarization- and wavelength-insensitive structures by cascading two couplers [31] to form a geometry similar to the Mach-Zehnder interferometer. The second coupler is used to cancel out any deviations caused by the first coupler. This, of course, only increases the already long length of a directional coupler device by a factor of two. In common with the TIR and Mach-Zehnder switch geometries, the variable refractive index region required makes it difficult to implement using the evanescently coupled active region in our SMVI material system.

2.5.6. Multimode Interference Coupler Switch

The multimode interference (MMI) coupler design uses the self-imaging principle to produce multiple images of an input optical field at the output. The self-imaging principle, as stated by Soldano *et. al.* is the "property of multimode waveguides by which an input field profile is reproduced in single or multiple images at periodic intervals along the propagation direction of the waveguide." [32]

The length scale over which the multimode interference occurs is known as the beat length of the MMI region. For a multimode region of

effective width W_e, and ridge effective index n_r, and a free-space wavelength of λ_0, the beat length, L_π, can be approximated by [32]:

$$L_\pi = \frac{\pi}{\beta_1 - \beta_0} \approx \frac{4 n_r W_e^2}{3\lambda_0}, \qquad [23]$$

where β_1 and β_0 are the propagation constants of the TE0 and TE1 mode (or TM0 and TM1 mode), the same as in Equation 22.

To illustrate the self-imaging principle behind MMI, assume a two-dimensional multimode waveguide capable of supporting m lateral modes experiences an input field, $\Psi(y,0)$. The input field can be decomposed into a summation of the guided modes, assuming the input field is too narrow to excite radiation modes:

$$\Psi(y,0) = \sum_{v=0}^{m-1} c_v \varphi_v(y). \qquad [24]$$

In Equation 24, c_v is the field excitation coefficient and φ_v is the field profile of the v^{th} mode.

This input will produce a field profile at a distance z, $\Psi(y,z)$, that can be expressed as a superposition of all of the guided mode field distributions:

$$\Psi(y,z) = \sum_{v=0}^{m-1} c_v \varphi_v(y) \exp[i(\beta_0 - \beta_v)z], \qquad [25]$$

where β_v is the propagation constant of the v^{th} mode. The general mode spacing can be approximated from the beat length L_π to be $\beta_0 - \beta_v \approx \frac{v(v+2)\pi}{3L_\pi}$. Substituting this expression into Equation 25 gives:

$$\Psi(y,z) = \sum_{v=0}^{m-1} c_v \varphi_v(y) \exp\left[\frac{iv(v+2)\pi}{3L_\pi} z\right]. \qquad [26]$$

It can be seen that the original input can be completely reproduced (self-imaged) when $\exp\left[\frac{iv(v+2)\pi}{3L_\pi} z\right] = 1$. This condition is satisfied when $z=p(3L_\pi)$, where p is any integer. When p is even, the image will be a direct one, when p is odd, the image will be mirrored. This effect is illustrated in Figure 15.

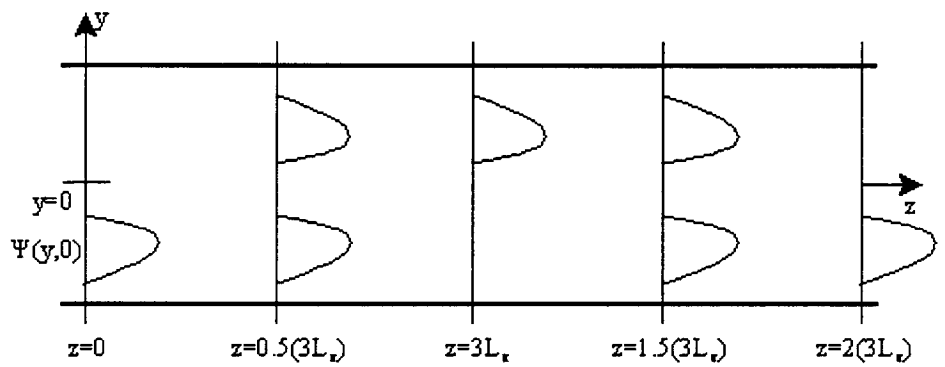

Figure 15 The self-imaging principle producing a mirrored single image at $z=3L_\pi$, direct image at $z=2(3L_\pi)$ and mirrored images at half-integer multiples of $3L_\pi$.

The self-imaging principle can be directly exploited for use as an optical switch. If the MMI region initially produces a mirrored image of the

input field in an output waveguide located at a distance $z=3L_\pi$, output1, then if the refractive index of the MMI region is changed such that the input signal experiences an optical length of $6L_\pi$, the output will instead be a direct image, and can be captured by an output waveguide, output2, that is on the opposite side of the y-axis (see Figure 16) compared to output1. It will also be demonstrated in Section 3.1.3 that MMI devices can operate as power splitters.

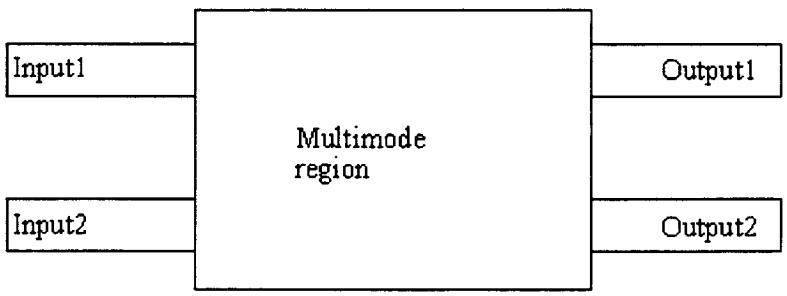

Figure 16 A 2x2 multimode interference geometry

Rajarajan *et. al.* [33] performed a comparison between MMI devices and directional couplers, and demonstrated that MMI devices are less polarization-dependent, less wavelength-dependent, and more robust to manufacturing process variations. The MMI devices also had a shorter length than directional couplers for the same crosstalk limit.

The MMI geometry has a wavelength dependence that can be seen in the equation for L_π. However, it is the refractive index change that is once again the main difficulty in this design. For the reasons outlined in the sections above, it is not possible to achieve a significant effective modal index change with the active waveguide geometry we are using. The MMI design will be considered briefly again, however, in the context of passive optical power splitting.

2.5.7. Microring/Microdisk Resonator Switch

Microring/disk resonator switches use a ring or disk structure between two parallel waveguides. They work in a manner similar to directional coupler switches, except with a more sophisticated design in the coupling region. The ring or disk is calculated to achieve resonance at a particular wavelength. At this resonance wavelength, light passes from the input waveguide, through the ring, and to out to the parallel output waveguide (see Figure 17). To switch to the other port, the refractive index of the ring or disk structure is changed, so that the light is no longer at the resonance wavelength and now passes directly through to the output.

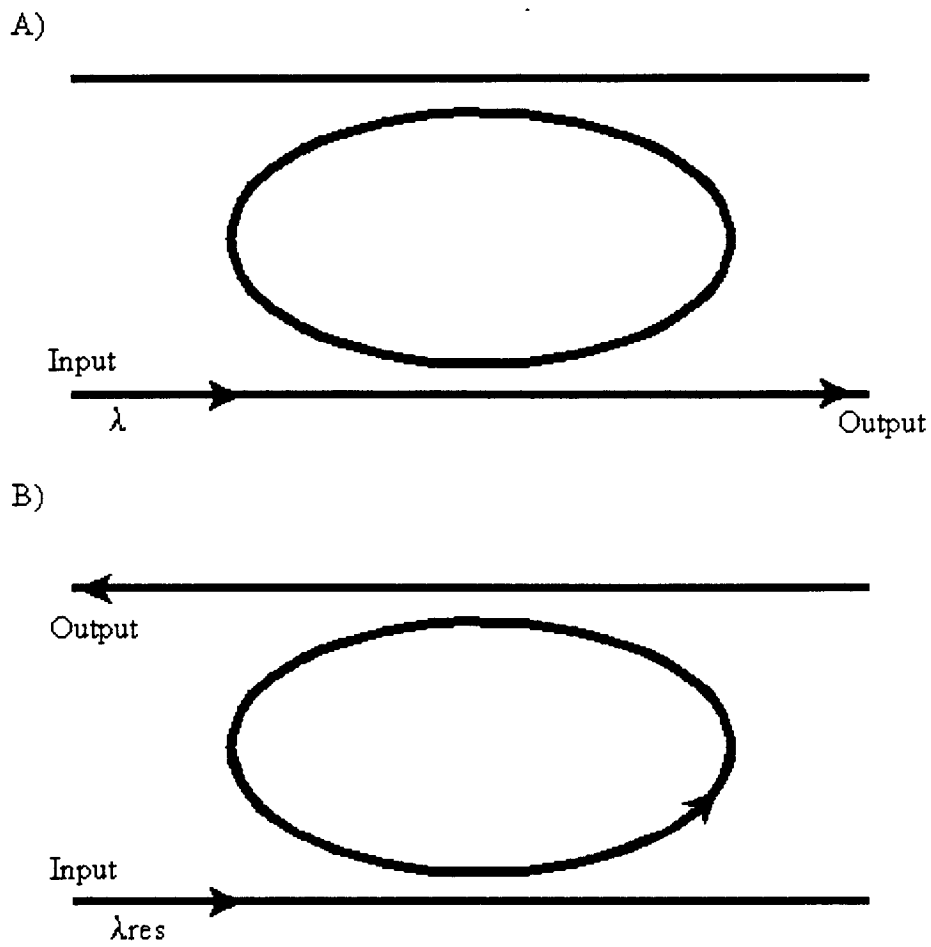

Figure 17 Microring resonator with input light at A) a non-resonant wavelength, and B) a resonant wavelength

This geometry is by design particularly wavelength-sensitive. The carrier-injection microring design of Ibrahim *et. al.* was found to have a negligible PDL. However, the device was useful only over a narrow wavelength range centered on 1543.5nm, with a 3dB bandwidth of only 1.2nm. The crosstalk of this switch was also quite poor, with a measured value of -7dB [34].

Once again, a major difficulty is that the refractive index change required makes this design difficult to implement in the vertically-

integrated platform. This design also requires a strong optical confinement so that light can be guided through the ring structures with minimal loss. As can be seen from Section 2.3, the multilayer ridge waveguide we are using is only weakly confining. This structure is also very sensitive to process variations, making it difficult to exploit commercially.

2.6. Switch Architecture - This work

The vertically-integrated waveguide described in Section 2.3 is a critical factor in our choice of an SOA-based switch architecture for this design. In this variant of the SOA-based design, the passive 3 dB splitter portion of the switch and the SOA regions are monolithically integrated as shown in Figure 9. This is done with a vertically-integrated active/passive waveguide prepared by lithography and etching of a single-growth epitaxial multilayer stack on an InP substrate. In the passive regions of the switch, a multilayer ridge structure provides simple waveguiding. In the active regions, the propagating mode is still concentrated in the passive waveguide core layer, but now it is also has an evanescent tail coupled to the active layer of the active waveguide that can provide gain.

In the active regions, the passive propagating mode is perturbed by the presence of the gain layer (see Figure 9). There is only a small change in the propagating mode between the active and passive regions. This helps ensure low backreflection and coupling losses at the junction of the active and passive waveguides, but it makes it difficult to guide the propagating mode based on changes in the refractive index of the active layer. This makes switching technologies that rely on refractive index variations to change the direction of light propagation impractical for this material system.

For this reason, and also because this design also has the potential of being insensitive to polarization and wavelength, having low loss, a high extinction ratio, and being robust to process variations, it was decided to use the SOA-based switch geometry for this design. It has been shown that SOAs can be integrated into the vertically-integrated active/passive platform [35], making this geometry easily adaptable for use in SMVI technology.

3. Design of an Integrated 3dB Power Splitter

The first portion of the SOA-based switch that must be designed is the passive optical splitter. There are several requirements for this splitter:

- It must be designed using active/passive optical waveguide geometry described in [12].
- The excess loss should be minimal.
- The power in both output waveguides should be equal, with half of the input optical power (3 dB) exiting into each of the output waveguides.
- It should be polarization insensitive.
- It should have a broadband frequency response.
- It should be a robust design that is able to function within the stated requirements despite small changes in dimensions and index arising from fabrication process variation.

3.1. Overview of Integrated Power Splitter Geometries

There are many different integrated optical power splitter geometries that have been designed, but they are mainly variations of three types: directional couplers, Y-branch, and multimode interference couplers.

3.1.1. Directional Couplers

Power splitting using directional coupler structures exploits the fact that when two waveguides are sufficiently close to be evanescently coupled to each other, power will transferred back and forth between them. Figure 18 illustrates a simple 2x2 directional coupler power splitter. The metric used to determine how the power is transferred between the two waveguides is the coupling coefficient, κ:

$$\kappa = \frac{\beta_0 - \beta_1}{2}, \qquad [27]$$

where β_0 and β_1 are the propagation constants of the first symmetric and antisymmetric supermode, respectively, the same as in Equation 22. The coupling coefficient is related to the coupling length of Equation 22 by $L_\pi = \pi/2\kappa$. Along the length of the coupling region, power is periodically transferred between output1 and output2 (as denoted on Figure 18). If an input signal of optical power P_0 is input in the upper waveguide as shown in the figure, the power seen at output1, P_{O1}, and the power seen at output2, P_{O2}, is given by:

$$P_{O1} = P_0 \cos^2(\kappa z)$$
$$P_{O2} = P_0 \sin^2(\kappa z). \qquad [28]$$

The power splitting ratio for a 3 dB splitter can now be calculated from Equation 28:

$$S = \frac{P_{01}}{P_{01} + P_{02}} = \cos^2(\kappa z) = 1/2. \qquad [29]$$

Through simple substitution into Equation 28, it can be seen that to have 3 dB power splitting, the condition $\kappa z = \pi/4$ must be satisfied.

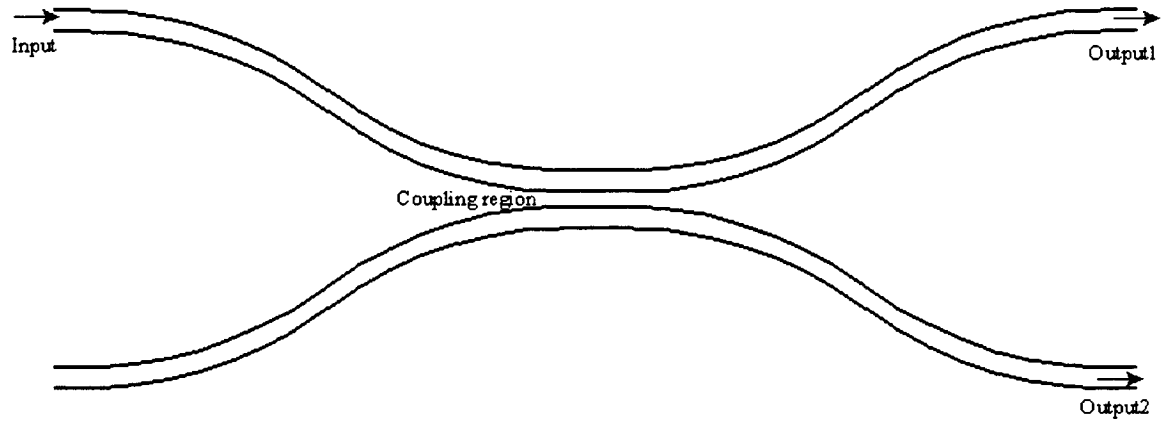

Figure 18 Schematic diagram of a 2x2 directional coupler power splitter

The coupling coefficient, κ, as shown in Equation 27, is dependent upon the propagation constants of the symmetric and anti-symmetric supermodes. As the dispersion curves in Section 2.1 demonstrate, the propagation constants are highly wavelength dependent. Depending upon the birefringence of the waveguide used, they can also be polarization dependent. Another difficulty is the sensitivity to design variations. A sensitivity analysis of the output power to the coupling length, L_π, (that is, finding $\partial P_{O1} / \partial L_\pi$) shows that the directional coupler actually has *maximum* sensitivity to coupling length variations when it is operated at the 3 dB point [32].

A number of approaches have been used to address the wavelength dependencies of the directional coupler design, for instance, using asymmetric couplers, with the waveguides possessing different parameters such as index and width [36], using tapered couplers where the propagation constant difference (and hence κ) changes along the

propagation axis [37], cascading couplers in a Mach-Zehnder type of configuration [31], and using dispersive materials in the waveguides to counteract the wavelength dependencies [38].

3.1.2. Y-branch

The Y-branch design is a deceptively simple power-splitting geometry, with a rich and varied history [39-43]. While the geometry itself is not complicated (see Figure 19) Y-branch designs have typically been optimized using computationally-intensive numerical methods such as BPM.

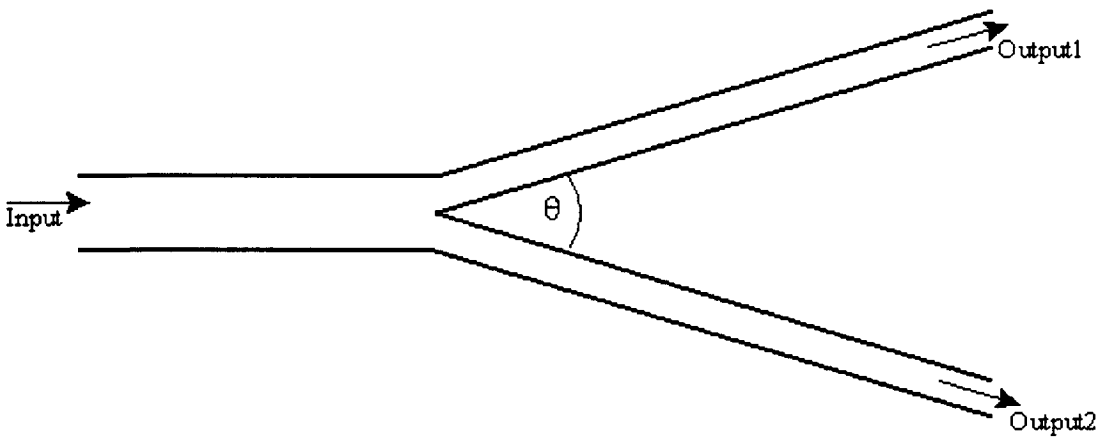

Figure 19 A traditional Y-branch power splitter design

A 3 dB Y-branch power splitter has two output waveguides that separate symmetrically at an angle θ from a single input waveguide. According to an investigation performed by Tsao and Lu, the Y-branch design is less sensitive to wavelength and more tolerant to process variations than the directional coupler, which has a frequency dependence as described in Section 3.1.1 [44].

There are a number of difficulties with the classic Y-branch design, such as the sharp vertex that is impossible to fabricate with perfect precision, and the abruptly tilting waveguides that introduce phase distortion. These will be described in greater detail in Section 3.3, where it will be seen that they can be overcome.

3.1.3. Multimode Interference Splitter

The MMI design described in Section 2.5.6 can be easily adapted for use as a 3 dB power splitter. Recall that Equation 25 described the field profile at a distance z in a multimode waveguide. If instead of integer multiples of the $3L_\pi$ (where L_π, the beat length, is given by Equation 23), we now consider half-integer multiples, where $z = {}^{p}/_{2}(3L_\pi)$, then Equation 25 becomes, according to [32]:

$$\Psi(y, \frac{p}{2}3L_\pi) = \sum_{v=0}^{m-1} c_v \varphi_v(y) \exp\left[iv(v+2)p\left(\frac{\pi}{2}\right)\right]. \qquad [30]$$

The summation in Equation 30 can be separated into even- and odd-numbered modes, assuming mode-field symmetry:

$$\begin{aligned}\Psi(y, \frac{p}{2}3L_\pi) &= \sum_{even} c_v \varphi_v(y) + \sum_{odd} (-i)^p c_v \varphi_v(y) \\ &= \frac{1+(-i)^p}{2}\varphi(y,0) + \frac{1-(-i)^p}{2}\varphi(-y,0). \end{aligned} \qquad [31]$$

Equation 31 shows that for half-integer multiples of $3L_\pi$, two images of the input field, $\Psi(y,0)$, in quadrature and with amplitudes of $2^{-1/2}$, are

produced. This property of MMIs can be exploited to produce power splitting if output waveguides are placed at this half-integer length.

As with directional couplers, the MMI has a frequency dependence, but it is still reasonably broadband [45]. The excess loss will also worsen with deviations from the design frequency in a more balanced manner. Also, in contrast to the directional coupler, the sensitivity to length variations is actually a minimum at optimal values for a 3 dB power splitter, and decreases in a balanced manner away from the design length [32]. MMI designs will also be more compact than comparable directional coupler designs.

A brief literature comparison that was performed by Soldano *et. al.* between an MMI and a single Y-junction splitter showed lower loss in MMI designs, but a lower polarization penalty and a larger bandwidth for Y-junction devices [32]. However, the comparisons of MMI and Y-junction devices that have so far been performed are not up-to-date, since they assume a standard Y-junction design with a sharp vertex, which is a serious limitation for fabrication of traditional Y-junction devices. In the next section a new design and optimization technique for Y-junction devices that addresses this issue is developed.

3.2. Modal Overlap Method for Y-junction Design

3.2.1. Design Considerations

The traditional Y-branch design, as described in Section 3.1.2 and shown in Figure 19, is based on a fixed splitting angle subtending a sharp vertex that demarcates the input single-waveguiding region from the dual output waveguiding region. There are three primary difficulties with this design:

- The sudden discontinuity at the junction between the single waveguide and the two output waveguides results in significant radiation loss for all but the smallest of splitting angles.
- The abruptly tilting output waveguides cause phase distortion of the input wave front, which worsens with increased angle.
- The sharp vertex of the design is not possible to faithfully fabricate, and the truncation of this point results in additional loss and polarization sensitivity, or ad-hoc design variants requiring considerable computational complexity to validate.

There have been many different approaches taken to minimize these losses. In some cases, such as the radiation loss study of Y-branch structures by Kuznetsov [39], these losses are reduced by keeping the branching angle of the output waveguides very small, typically less than one degree. He was able to demonstrate that in the limiting case as the angle approached zero, the loss was minimized. Hanaizumi *et al.* used a higher refractive index in the branching region to bend the input wavefront towards the tilted output waveguides [40], while Safavi-Naeini *et al.* used output waveguides of differing refractive index tilted at Brewster's angle to reduce the phase-front distortion [41]. More recently, microprisms in the branching section [42] and employing wavelength skipping in custom designed structures have been used [43]. Clearly, these design variants require full beam propagation modeling treatments to extract excess loss information, and their optimization by such a modeling process is exceedingly tedious.

The approach to Y-branch design taken in this thesis is to break down the power splitter into its most elemental functional blocks, with a focus on the critical fabrication parameter(s) as the key tolerancing variable(s). We take a fully reductionist approach, where power splitting is

effectively decoupled from spatially redirecting power flows. That is, our input and output waveguides are collinear at the junction (a "zero splitting angle", which eliminates phase distortion), with a gap between the output waveguides, *g*, (see Figure 20) set by the minimum gap width, which we will see is the critical fabrication parameter. If the waveguides used in the Y-branch are all adiabatically tapering and separating, and the dual output waveguides are initially parallel to the input waveguide, then the discontinuity between these two regions is the dominant source of loss in the device, there being no phase-front distortion. In this case it is possible to reduce the design problem to finding the optimal dimensions of the single-core and dual-core waveguides immediately before and after this central discontinuity. Surprisingly, this appears to be a novel design approach, there being no published reports in the literature to date.

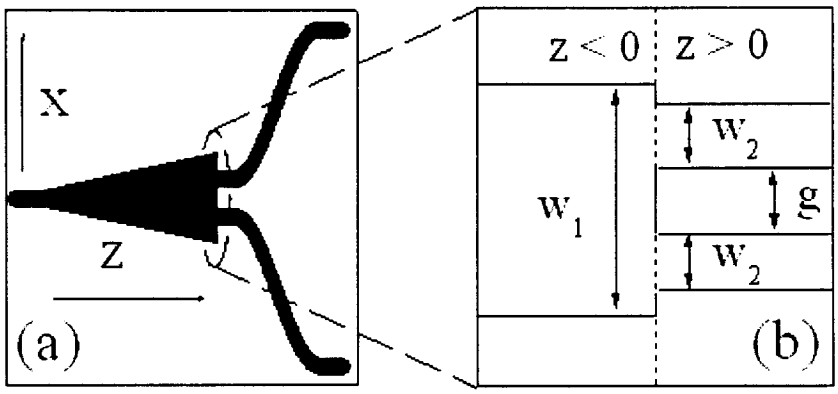

Figure 20 a) Full Y-branch power splitter layout, b) single to dual waveguide junction

The approach described above dramatically simplifies the optical modeling, since the key optimization is restricted to establishing the waveguide parameters at the discontinuous junction. This is akin to waveguide coupling problems, and may be treated using modesolvers rather than beam propagation techniques. BPM techniques are only

required to ensure the adiabaticity of tapered or bending waveguides, and for validation of our approach.

The modal overlap design method focuses on the discontinuity between the single waveguide and dual output waveguides. It is a first-order approximation to the generalized scattering matrix and mode matching technique modal decomposition method [46] that can be applied to different material systems and waveguide geometries. This method is capable of designing optimal, robust and easily manufactured Y-branch power splitters with minimal computational resources. In this thesis, it has been applied to the case of buried-core silicon waveguides and the complex passive ridge structure of the vertically-integrated waveguide we are using in the final design.

3.2.2. Theory

To simplify the problem, the input waveguide is assumed to be a single-mode waveguide that has been adiabatically expanded or reduced in size before the junction (see Figure 20). It is also desired to have maximal coupling into a single guided mode of the dual-core output waveguide. These conditions mean that multiple modes in the input and output waveguide do not need to be considered.

The time-independent electric and magnetic fields in waveguides I (single-core input waveguide) and II (dual-core output waveguide) are denoted as $\mathbf{E}_n^{(i)}$ and $\mathbf{H}_m^{(i)}$, respectively, with n,m=I,II and i=TE,TM.

Using this simplified eigenfunction expansion method, the coupling efficiency is given by the normalized overlap integral:

$$\eta^{(i)} = \frac{\left|\left\langle \mathbf{E}_{\mathrm{I}}^{(\mathrm{i})}, \mathbf{H}_{\mathrm{II}}^{(\mathrm{i})} \right\rangle\right|^2}{\left\langle \mathbf{E}_{\mathrm{I}}^{(\mathrm{i})}, \mathbf{H}_{\mathrm{I}}^{(\mathrm{i})} \right\rangle \left\langle \mathbf{E}_{\mathrm{II}}^{(\mathrm{i})}, \mathbf{H}_{\mathrm{II}}^{(\mathrm{i})} \right\rangle}. \qquad [32]$$

The inner product < , > is given by the time-average flow of optical power:

$$\langle \mathbf{E}, \mathbf{H} \rangle = \iint_S \frac{1}{2} \Re\left[\left(\mathbf{E} \times \mathbf{H}^*\right) \cdot \hat{\mathbf{a}}_z\right] dS, \qquad [33]$$

where $\mathbf{a_z}$ is a unit vector along the waveguide axis, S is the interface, and * represents the complex conjugate.

To implement these equations, the modal fields (**E**,**H**) were first determined by finite-element analysis using the FEMLAB software package from COMSOL Inc [3]. The modal overlap calculation was then performed in a MATLAB post-processing environment from COMSOL Inc [47]. Figure 21 shows an example of a modal solution for the single- and dual-core waveguides.

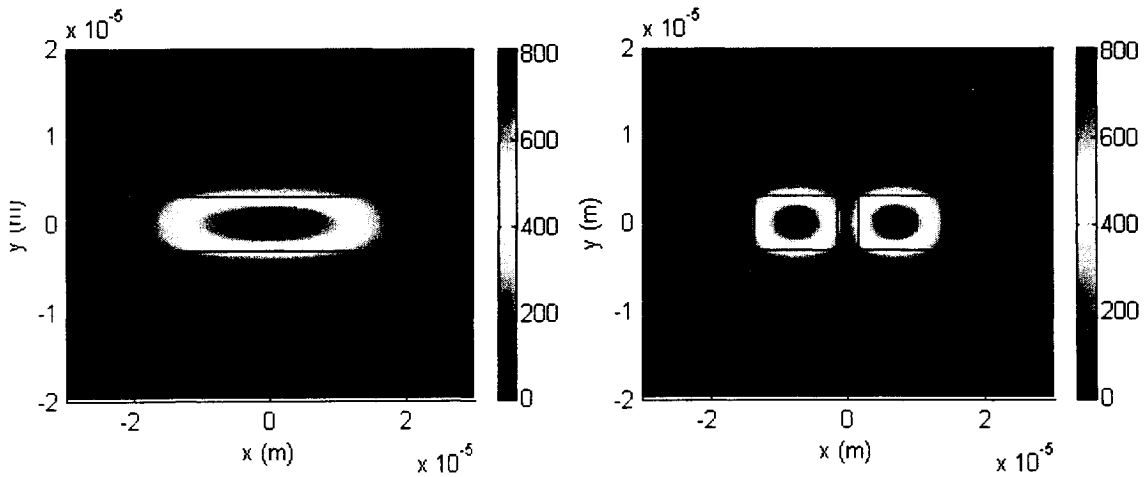

Figure 21 Mode profiles of the single and double core waveguides (calculated using FEMLAB)

3.2.3. Application to Buried-Core Silica Waveguide Geometry

The Modal Overlap Method (MOM) for designing Y-branch power splitters was first applied to the simple case of a lossless buried-core silica waveguide. Silicon-on-insulator photonic integrated circuits show great promise for the development of future optoelectronic devices [48]. A computational area of 70μm x 40μm was used, with an adaptive mesh as small as 0.25μm in the core/gap region. Using these dimensions convergence to five significant figures of the coupling efficiency was obtained. The details of the mode-solving technique using FEMLAB will not be discussed in detail for the simple buried-core geometry, since the complex multilayer ridge structure studied in Section 3.3 provides a better illustration of this method.

The refractive index of the cladding was set at n_{cl}=1.445 and the dielectric contrast, Δ, given by Equation 1 of Section 2.1, was varied from 0.685% to 4.685% in five uniform increments by varying the refractive index of the core. These are typical values for the doped-glass process space from the low-contrast regime, where waveguides are near mode-matched with single-mode optical fiber, to the high contrast regime of active planar waveguiding.

To ensure single-mode operation throughout the device, the waveguide core height, h, (as shown in Figure 3) was chosen so that the normalized frequency of a single-core square waveguide at a free-space wavelength λ_0=1.55μm would be V=2.07094.

As can be seen from the dispersion curves for the dual-core buried silicon waveguide seen in Figure 22 (calculated using FEMLAB), and the dispersion curves for a single-core buried silicon waveguide shown in Figure 4, this normalized frequency falls within single-mode operation.

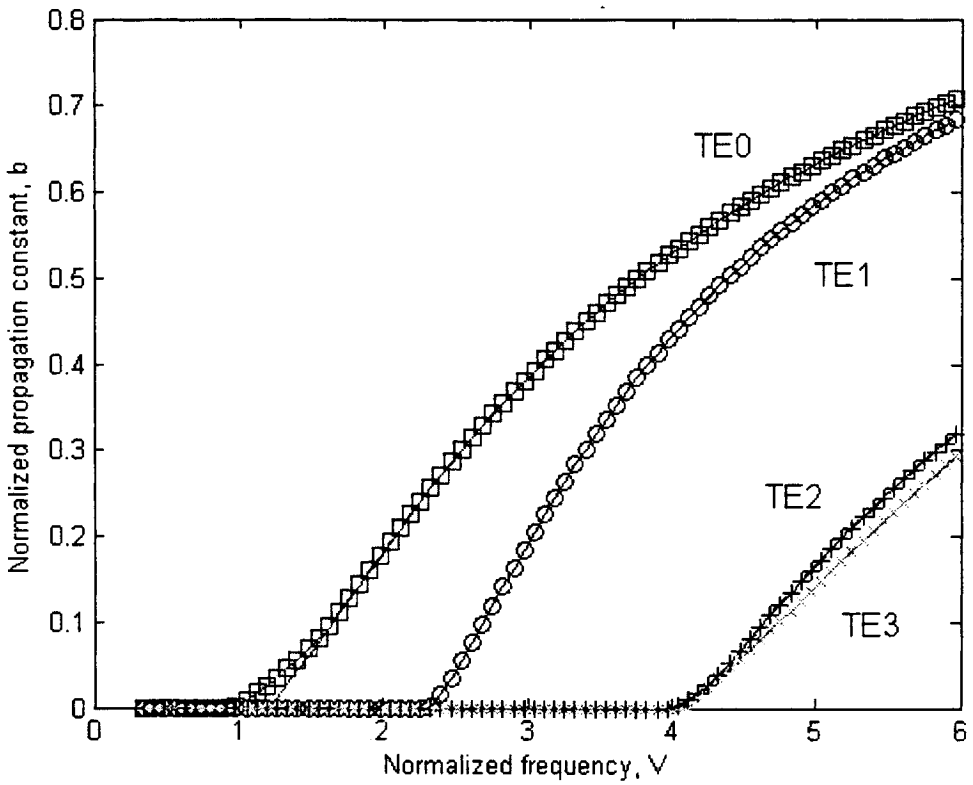

Figure 22 Dispersion curves for a dual-core buried silicon waveguide

The excess loss (the logarithmic form of the coupling efficiency given by Equation 32) vs. single-core width for the lowest contrast TE case is shown in Figure 23. For these results, square dual-core waveguides with varying gaps of 1, 2, and 3μm were simulated at a wavelength of 1.55μm. The solid, dashed, and dot-dashed curves each represent 30 simulation points obtained using the Modal Overlap Method and the markers indicate results obtained using BPM modeling [49].

As these curves show, there is clearly an optimal value of the single-core width for the particular dual-core waveguide geometry chosen. As the shallowness of the curves show, this optimal value is insensitive to small changes in gap or single-core width. As the gap between the two output waveguides is reduced, the coupling efficiency increases. This is to be

expected since the smaller the gap between the two dual-core waveguides, the more closely it approximates a single-core waveguide.

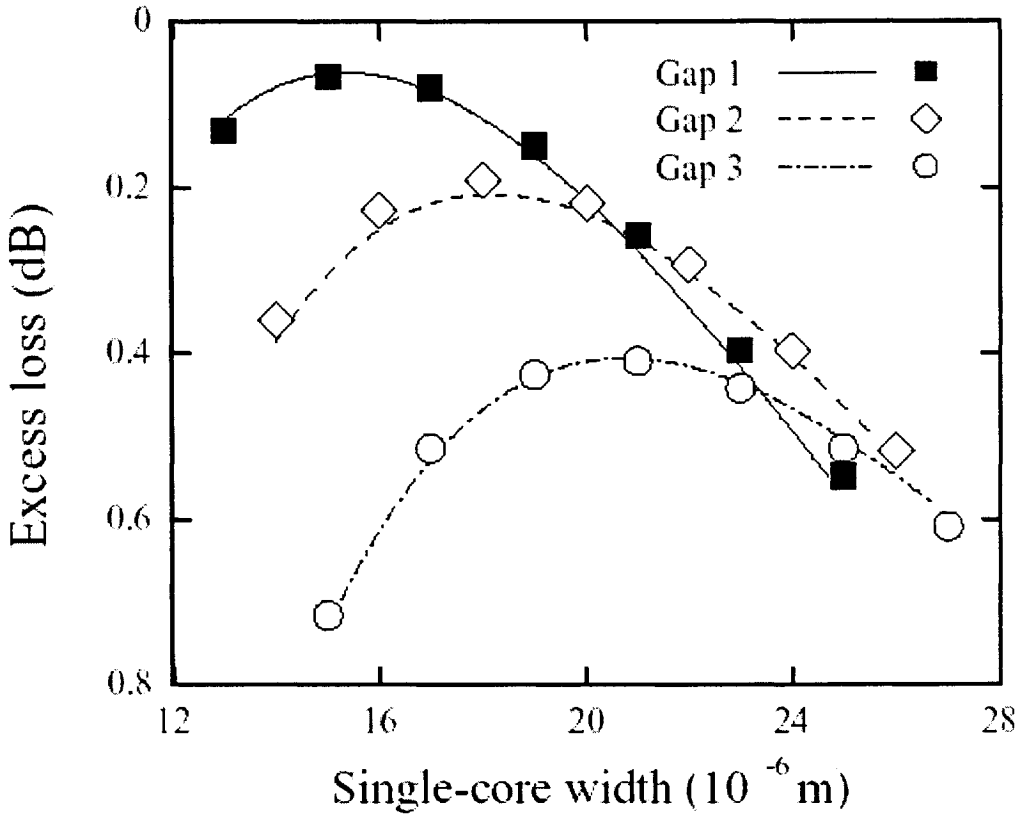

Figure 23 TE Excess loss vs. single-core width for the lowest index contrast and fixed, square 6μm dual-core waveguides for Gap 1 = 1μm, Gap 2 = 2μm and Gap 3 = 3μm. The solid, dashed and dot-dashed curves represent finite-element analysis results, the markers from confirmatory beam propagation simulations

To confirm the modal overlap calculations for this contrast and polarization, the beam propagation method was used. The beam propagation calculations were performed using OptiBPM 6.1 [50] waveguide optics modeling system software [51]. A three-dimensional,

semi-vectorial approach was used on the full Y-branch design including the adiabatic input taper and adiabatically separating output waveguides. To obtain convergence to two decimal places, a grid spacing as low as 10 points/μm in the x-direction was used. All waveguides were assumed to be lossless. To determine the excess loss, the total power in the two output waveguides (normalized to the input power) was calculated, and then added together. The excess loss is the logarithmic value of this combined power.

The BPM results, as seen in Figure 23, are in excellent agreement with those obtained using the Modal Overlap Method. This validates the use of MOM to optimize this Y-branch design. Figure 24 shows an image of one of these BPM simulations for a single-core waveguide width (w1 in Figure 20) of 24μm and two 6μm square dual-core waveguides (w2 in Figure 20) separated by a gap g=2μm. Figure 24 shows very little forward scattered radiation components. While there is scattering at the interface, it is at an angle of more than ±60 degrees from the direction of propagation and so would have a minimal affect on the separating output waveguides.

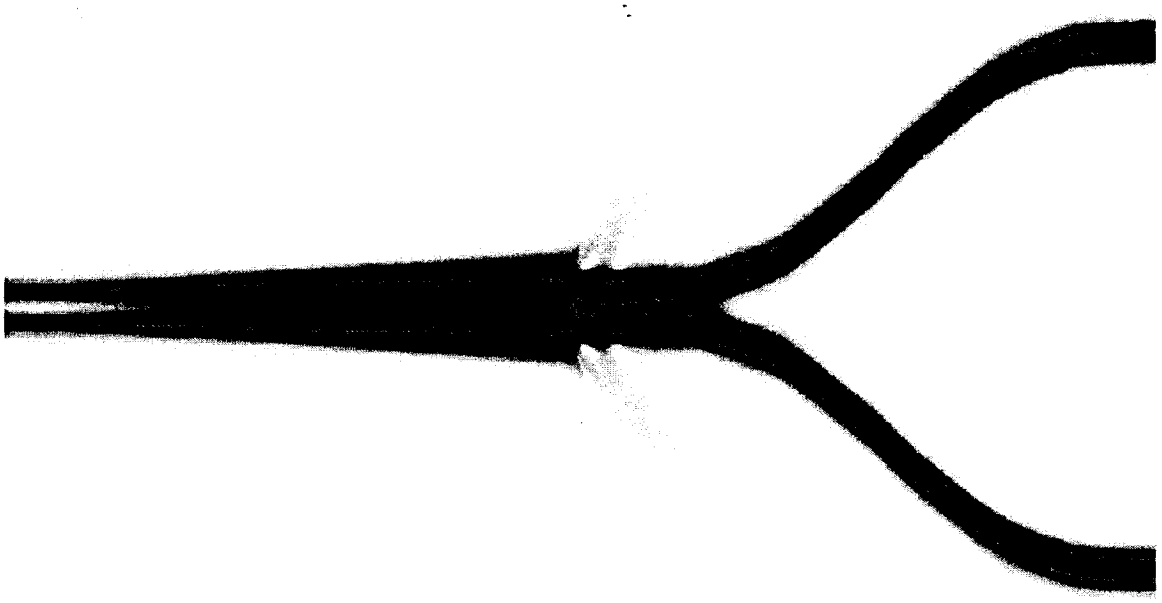

Figure 24 Optical field amplitude for the full Y-branch design

It has been determined that for a particular fixed dual-core geometry there is an optimal value of the single-core waveguide width. The next step was to look at optimal values for the dual-core width. For each different value of the dual-core width, the value of the single-core width was varied and curves similar to Figure 23 were produced. The excess loss for the optimal value of the single-core width for each of these curves was then used as the minimum loss for each individual dual-core width. The result of these calculations is shown in Figure 25 for Δ=0.685% and both polarizations. The index contrast, Δ, is calculated using Equation 1. The vertical dotted line shows the optimal values of the dual-core waveguide width for three different gap widths. For all gap widths, the optimal dual-core width was one-half of the core height. Once again, as the dual-core gap decreases, the excess loss decreases. This implies that the loss can be reduced with improved process control and fabrication. The sharp drop at lower dual-core widths past the optimal width is due to the optical mode becoming progressively less confined.

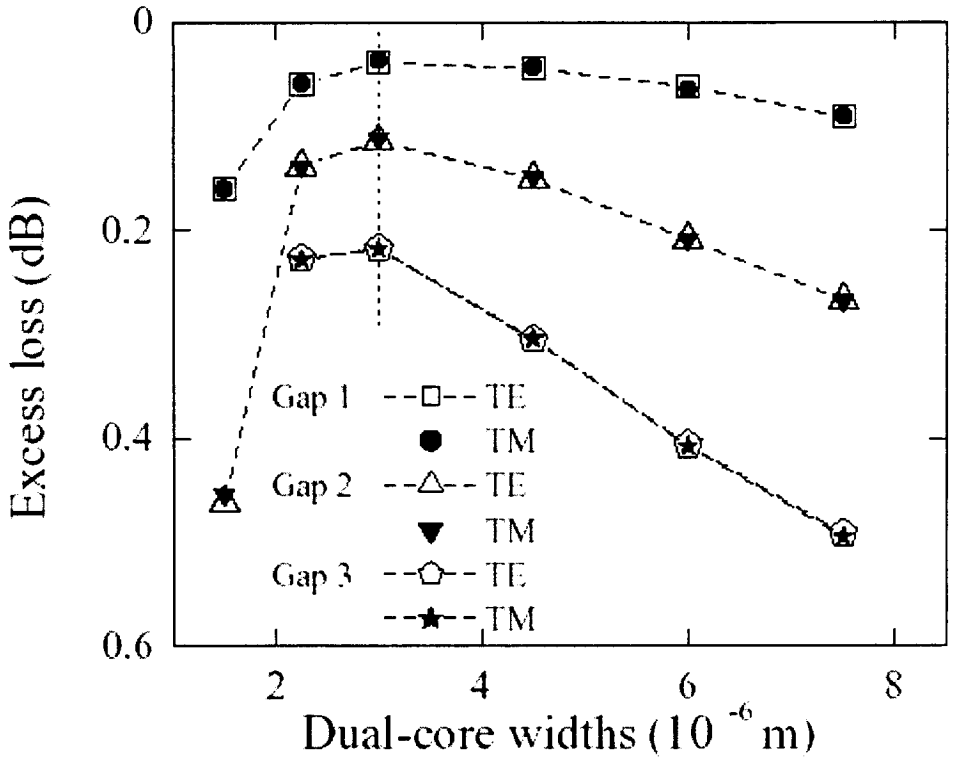

Figure 25 Excess loss vs. dual-core width (using the optimal single-core width value) for the lowest contrast and gaps of Gap 1 = 1μm, Gap 2 = 2μm, and Gap 3 = 3μm. The open symbols represent TE mode values, the closed symbols TM values, while the dotted vertical line represents optimal values

The effect of varying index contrast can be seen in Figure 26. Here the excess loss vs. dual-core width data is obtained in a similar manner to that in Figure 25, except now using different index contrasts and a fixed 1μm dual-core gap. Figure 26a shows the three lowest index contrasts, Figure 26b shows the two highest index contrasts. Once again an optimal value for the dual-core width is found to be one-half the height. As the

index contrast increases, the loss and the sensitivity also increase. There are also what appear to be slightly anomalous values for the thinnest dual-cores at the highest index contrasts, shown in the dashed area of Figure 26b. These secondary peaks represent an inversion of the design shown in Figure 20, where the single-core width is actually smaller than the sum of the dual-core widths and the gap. This is represented in a revised design shown in Figure 27. In this design, the dual-core widths are sufficiently small so that most of the mode is confined between the two cores rather than within them.

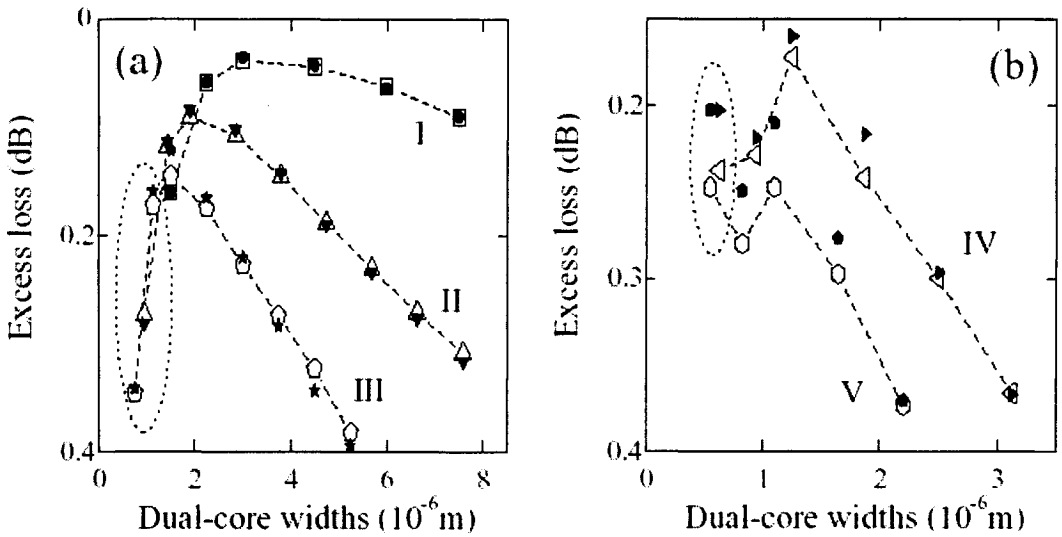

Figure 26 Excess loss vs. dual-core width (using optimal single-core value) for a 1μm gap and a) the index contrasts I=0.685%, II=1.685%, III=2.685%, b) the index contrasts IV=3.685% and V=4.685%; the open markers represent TE mode values and the closed symbols TM mode values

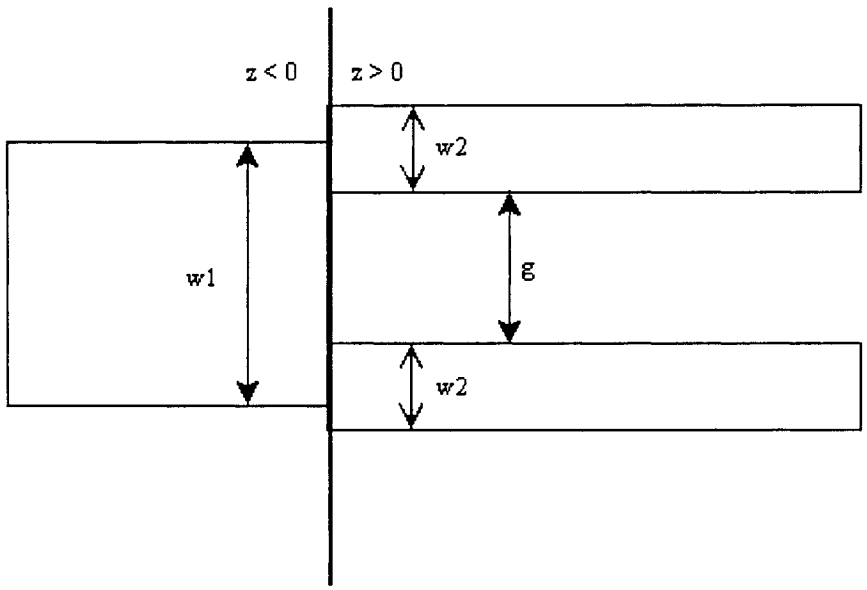

Figure 27 Inverted optimal design for thin dual-core waveguides at high index contrasts

The polarization dependence of this design was determined using the same data illustrated in Figure 26. For each of the points in Figure 26, the PDL was calculated by subtracting the TE and TM mode excess loss. The result is shown in Figure 28, which shows very low polarization dependence for this design of less than 0.02 dB for the lowest index contrasts and a maximum 0.15 dB for the highest index contrasts.

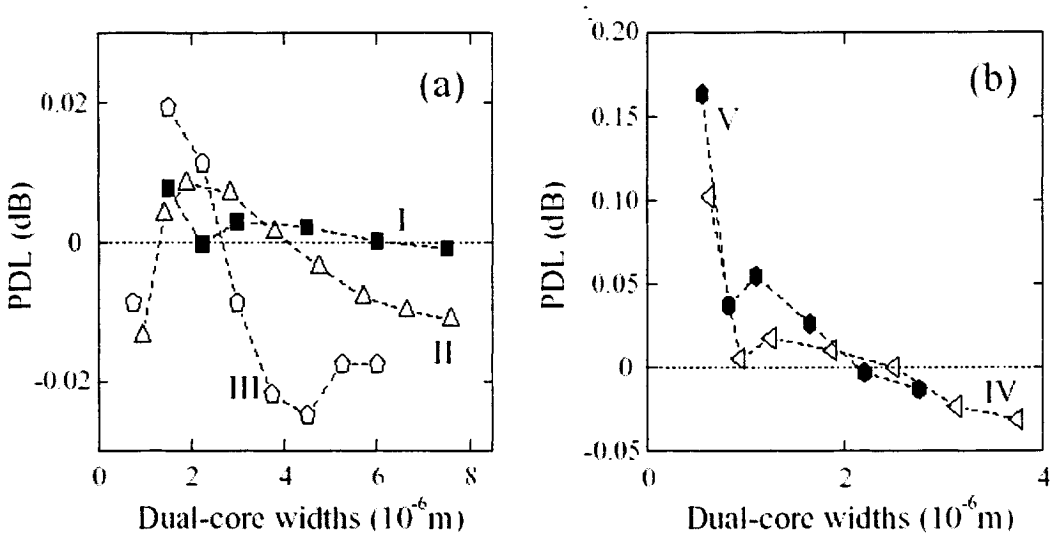

Figure 28 Polarization dependence vs. dual-core width at the optimal single-core value for all contrasts (contrast notation is the same as in Figure 26)

The optimal layout parameters for each index contrast are shown in Table 3 below, along with the corresponding excess loss.

	Contrast (%)	Core index	Gap (μm)	Single-core width (μm)	Excess loss (dB)
I	0.685	1.455	1	8.95	0.036
I	0.685	1.455	2	11.45	0.11
I	0.685	1.455	3	13.95	0.22
II	1.685	1.47	1	6.48	0.084
II	1.685	1.47	2	9.98	0.24
II	1.685	1.47	3	11.3	0.47
III	2.685	1.4854	1	5.88	0.12
III	2.685	1.4854	2	8.38	0.37
III	2.685	1.4854	3	10.88	0.71
IV	3.685	1.5014	1	5.31	0.16
IV	3.685	1.5014	2	7.81	0.48
IV	3.685	1.5014	3	10.31	0.91
V	4.685	1.5179	1	4.98	0.21
V	4.685	1.5179	2	7.48	0.59
V	4.685	1.5179	3	9.68	1.1

Table 3 Optimal silica-on-silicon buried-core Y-branch layout parameters [49]

3.2.4. Summary of Advantages and Disadvantages

The Y-branch power splitter design method described in Section 3.2.3 has four significant advantages:

- *Design Speed* – Since only the junction of the dual- and single-core waveguides are considered in this method, it requires significantly less computational resources to evaluate a particular geometry than performing a full BPM simulation. This in turn gives more freedom to explore the entire design space of the device.

- *Low Loss* – With a more complete exploration of the design space allowed due to the speed of this method, it is easier to find the optimal, lowest loss geometry.
- *Low PDL* – The low PDL of this device demonstrated in Figure 28 is an obvious advantage in the overall switch design
- *Easy to manufacture* – This design features no sharp vertex that would be truncated during manufacture. Instead it incorporates a gap between the output waveguides into the optimization procedure. The shallowness of the optimal curves shown in Figure 23 also indicates that this is a robust design that is not sensitive to minor process variations.

There is one drawback of the design that should be mentioned. The adiabatic tapering and separation of waveguides required for this design could make the device length prohibitive. While this is not a difficulty for the lossless waveguides described in this previous section, in reality, a longer device means higher waveguide losses. For waveguides with sufficiently high absorption coefficients, the benefits of this design could be outweighed by the losses. Also, less compact designs mean fewer devices per wafer, and therefore a higher cost.

In general, however, the Modal Overlap Method applied to the design of a Y-branch power splitter has produced promising results. The main difficulties of traditional Y-branch designs, the sharp vertex and tilting waveguides, have been overcome, and the strengths, such as low polarization dependence and loss, have been retained. It also is applicable to different materials and geometries, such as the vertically-integrated passive waveguide we are using.

3.3. Application of the Modal Overlap Method to the Vertically-Integrated Waveguide Geometry

3.3.1. Design Statement

Given the advantages outlined in Section 3.2.4, we decided to apply the Modal Overlap Method to the design of the 3 dB power splitter based on the InP material platform and the vertically-integrated waveguide geometry. In so doing, only the passive layers of the heterostructure are retained since the active layers are removed by etching for passive optical devices such as the power splitter.

There are three factors that make this Y-branch design using the vertically-integrated passive waveguide more difficult than with the simple buried-core silicon waveguides described in Section 3.2.3. The first is that vertically-integrated material system uses a multilayer ridge waveguide geometry for passive structures. The second complication is that the approximation of a lossless waveguide no longer applies, as the materials used are absorbing. The third factor regards the imposition of manufacturing constraints specific to the foundry and fabrication process chosen for our design. We discuss these in more detail below.

FEMLAB is capable of easily handling multilayer ridge waveguide structures but additional computational time is required due to an increase in the number of mesh elements. More mesh elements are required to accurately address the greater spatial complexity, in particular the increase in the number of layers and consequent refractive index discontinuities. This geometry also requires approximately twice as much time to simulate using BPM, so this complex structure is even more suited to the less computationally intensive Modal Overlap Method.

Treatment of material absorption can be addressed in the modeling by including imaginary terms in the refractive indices of lossy layers when specifying the design in FEMLAB or OptiBPM. With a lossy waveguide, the losses of the full design obtained by BPM simulations will be larger than the junction loss calculated using the Modal Overlap Method. A trade-off between adiabaticity and loss in the waveguide could be required, where the waveguide is shorter than required to achieve the adiabaticity condition in order to offset the losses of a long waveguide.

There are now additional constraints on the optimal design imposed by the manufacturing process used. Since this power splitter design was intended to be manufactured as part of a larger proof-of-concept integrated design including the vertically-integrated active SOA structures, the feature sizes and tolerances were relatively large. The smallest feature size available was 1.5μm with a tolerance of +/- 0.5μm, and no aggressive trenching options were considered. These considerations are more typical of real-world waveguides than the more ideal lossless waveguides of Section 3.2.2. The application of the Modal Overlap Method to the vertically-integrated passive waveguide structure will demonstrate the suitability of this method for practical power splitter designs.

3.3.2. FEMLAB Finite-Element Simulation Results

The first step in applying the Modal Overlap Method is to calculate the modal fields of the 2D passive waveguide structures. The layers of this waveguide are described by layers 0-4 in Table 1 of Section 2.1. The single-ridge geometry is simply the multilayer ridge shown in Figure 7 of Section 2.3. The dual-ridge geometry consists of two ridges of the same width separated by a gap. The gap is a critical fabrication parameter of the Y-branch power splitter device.

The computational area, chosen to provide convergence of the eigenvalue of the modal solution, was 25μm x 6μm. To reduce computational time, the layers were divided into sections of different mesh sizes, with higher mesh densities in the core of the waveguide underneath the ridge where the mode is almost entirely confined. These regions of different mesh density within a layer are shown outlined in red in Figures 29 and 30. The mesh size was progressively decreased until the value of the eigenvalue of the modal solution converged to four decimal places. This resulted in a maximum mesh size in the core area of 0.1μm.

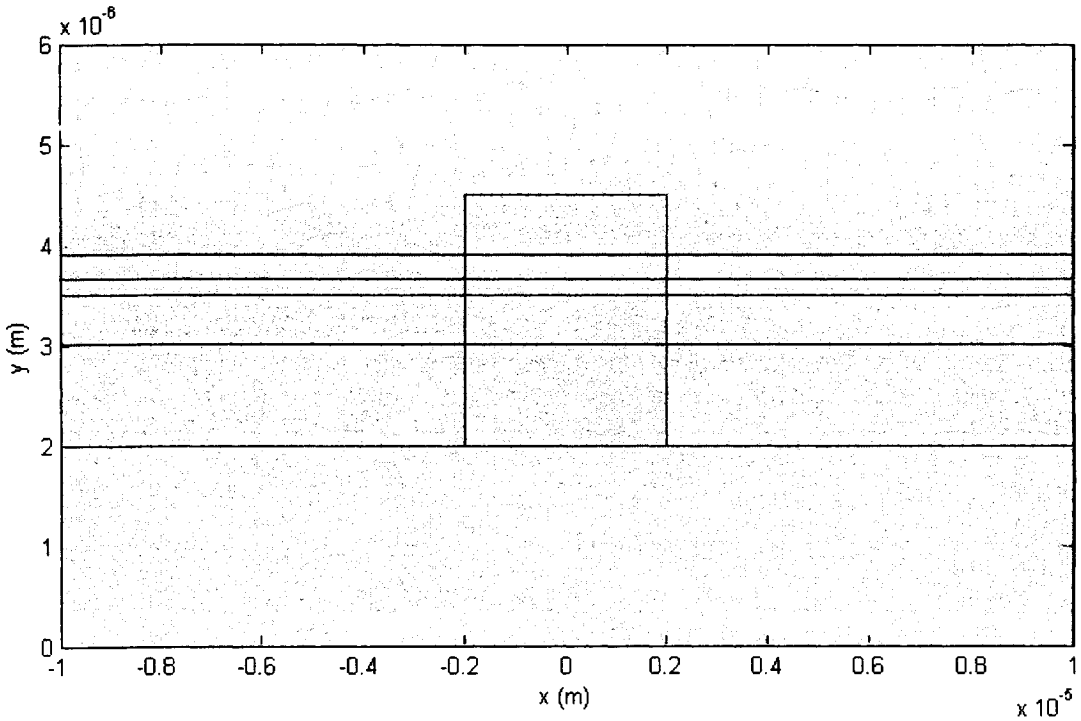

Figure 29 Adaptive mesh used for the vertically-integrated multilayer ridge passive waveguide geometry

It should be noted that the high mesh density in the layer directly underneath the ridge is required to resolve a 0.005μm etch stop layer that

is not visible in Figure 29. This is a consequence of the adaptive mesh capability of FEMLAB which ensures that every layer has a sufficient number of mesh elements to be fully modeled.

Next the mode for the double-ridge waveguide was solved. As with the single-ridge waveguide, the layers were divided into sections of varying mesh densities. Once again, the smallest mesh sizes are found in the areas underneath the ridge sections where the majority of the mode is confined. This adaptive mesh, with a maximum mesh size of 0.1μm in the core region underneath the ridges, is shown in Figure 30.

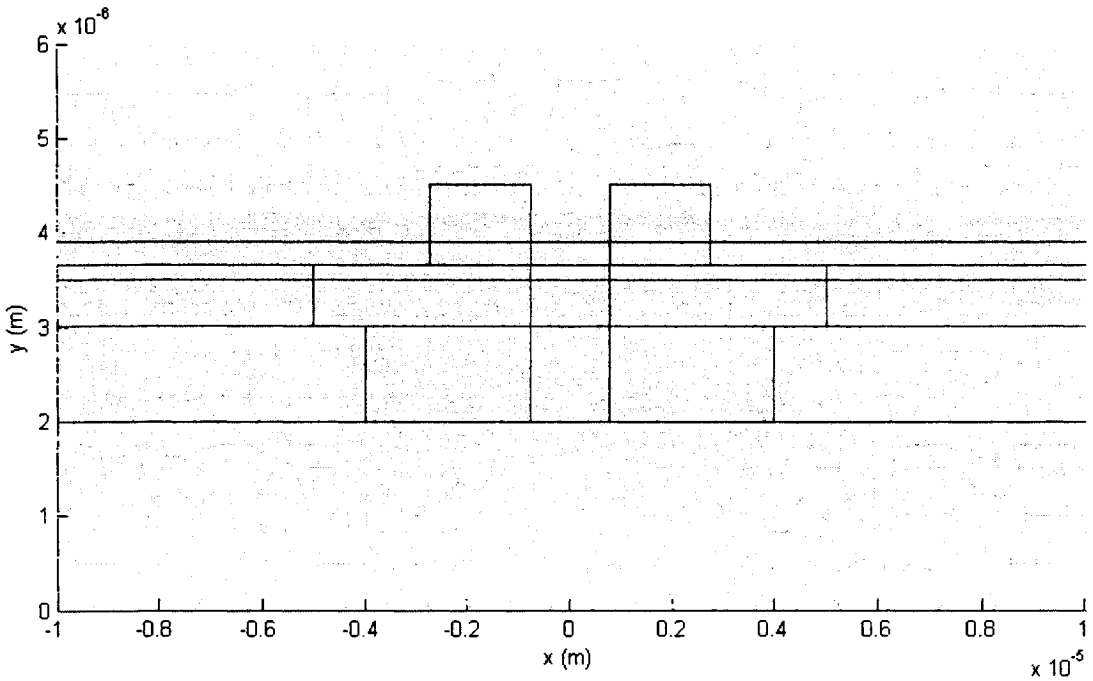

Figure 30 Adaptive mesh of the dual-core vertically-integrated passive waveguides

The TM mode solutions for the single- and dual-ridge vertically-integrated waveguides are shown on a logarithmic scale in Figures 31 and 32.

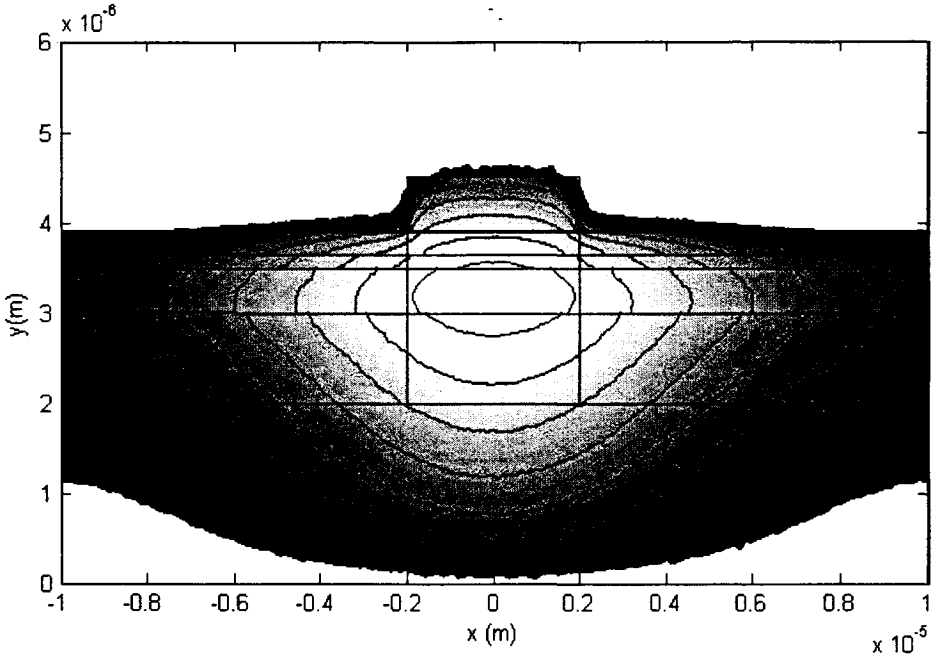

Figure 31 Logarithmic electric-field profile (TM mode) of the single-ridge vertically-integrated passive waveguide (5 dB contours)

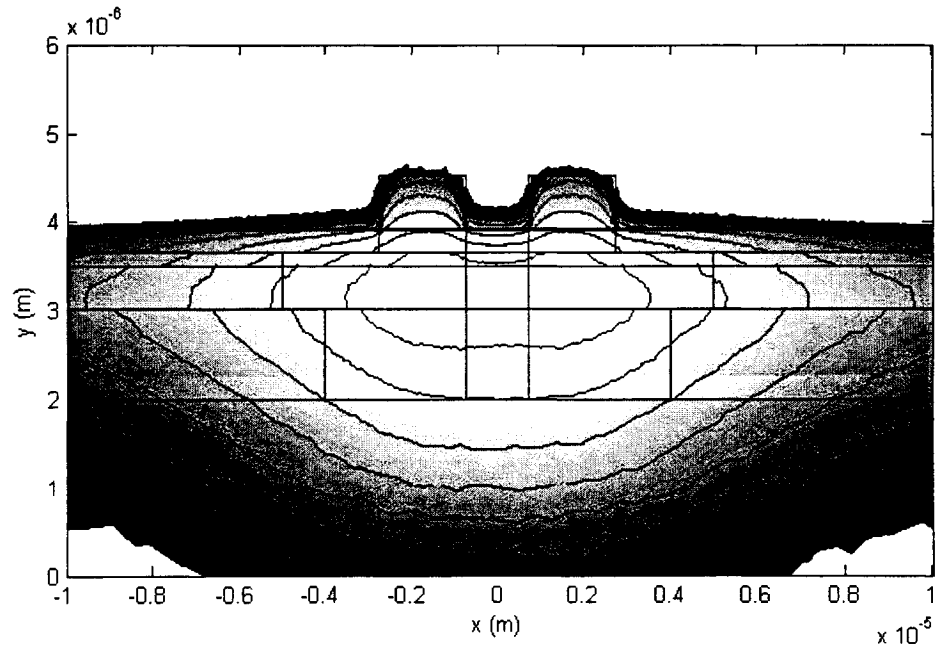

Figure 32 Logarithmic electric-field profile (TM mode) of the dual-ridge vertically-integrated passive waveguide (5 dB contours)

For the single-ridge waveguide shown in Figure 31 with a ridge width of 4μm, the effective modal index is $n_{eff,I}^{TM} = 3.1822 + i4.9 \times 10^{-4}$. For the dual-ridge waveguide of Figure 32, with a dual-ridge width of 2μm and a gap width of 1μm, the effective modal index is $n_{eff,II}^{TM} = 3.1825 + i4.9 \times 10^{-3}$.

Once FEMLAB had calculated these modal fields, overlap calculations could be performed in MATLAB using the same code used in Section 3.2.2. To remain within the manufacturing constraints, a fixed gap of 2μm was used. It has been shown in Section 3.2.3 that the smaller the gap, the lower the junction loss, and 2μm is the smallest gap allowed within the tolerance and feature size constraints. The single-ridge width was varied between 2μm and 10μm, and for each single-ridge waveguide an overlap calculation was performed with a dual-ridge waveguide width of 2μm, 2.5μm and 2.9μm. The results of this calculation are shown in Figure 33 (excluding the 2.9μm results that were noticeably non-optimal).

Using initial results, it was decided to use 8μm as the single-ridge width value. It can be seen from Figure 33 that 8μm is not the optimal value for the single-ridge width. However, our initial calculations past 8μm were complicated by the presence of additional lateral modes. These lateral modes were erroneously used in the modal overlap calculations, giving poor results. This difficulty was not resolved until the optimization of the power splitter using the single-ridge width of 8μm had already begun. There are other considerations, however, that make 8μm a desirable single-ridge width. It is still within a region of relative stability of the excess loss with respect to single-ridge width. Since an 8μm wide waveguide requires a shorter taper than the optimal value at ~10.5μm, the smaller overall length and correspondingly lower absorption loss could compensate for this not being the optimal (minimum junction loss) single-

ridge value. This is in fact the case for this particular waveguide geometry, as will be seen in Section 3.3.3.

At a width of 8μm, the TE mode had minimum loss with a dual-ridge width of 2.5μm, and the TM mode had minimum loss at a dual-ridge width of 2μm. As a compromise between these two dual-ridge values, a value of 2.25μm was chosen for the dual-ridge waveguide. This balanced the junction loss between the TE and TM mode, reducing the PDL.

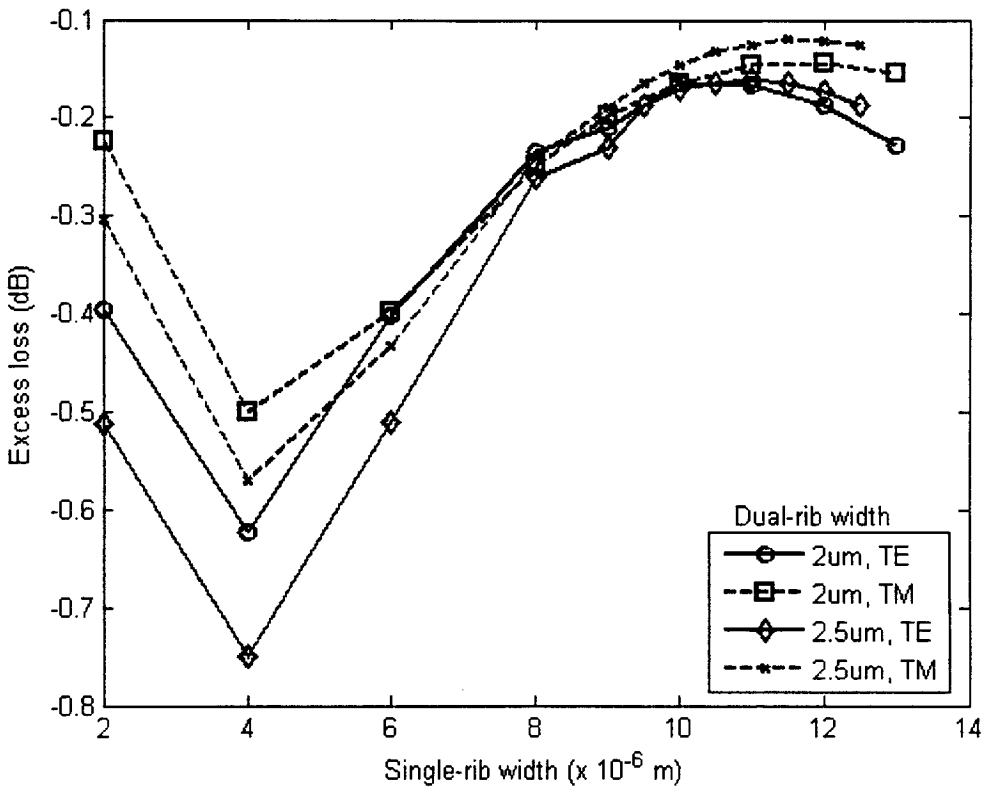

Figure 33 Excess loss vs. single-ridge width for dual-ridge widths of 2μm and 2.5μm

The result of the overlap calculations for these geometrical parameters is an excess loss of 0.244 dB for the TE mode and 0.236 dB for the TM, a nearly polarization insensitive result.

Later modal overlap calculations were performed that more comprehensively explored the single-ridge and dual-ridge values. These calculations showed that the minimum loss for the TE mode was 0.16 dB at a single-ridge width of 10.5μm and a dual-ridge width of 2.3μm, and the minimum loss for the TM mode was 0.13 dB at a single-ridge width of 11.5μm and a dual-ridge width of 2.5μm. It was decided to also perform BPM simulations on a more optimal value of the single-ridge width of 10.5μm and a dual-ridge width of 2.25μm, since these values provided a compromise between low loss and polarization dependence. For this junction geometry, the excess TE loss is 0.16dB and the excess TM loss is 0.14dB.

3.3.3. OptiBPM Beam Propagation Method Simulation Results

For the reasons outlined in Section 3.3.1, it is more difficult to optimize the tapers and bends of this device than the buried-core lossless waveguide device in Section 3.2. It is important to balance the long waveguides required to approach adiabaticity with the resultant larger absorption losses.

All waveguides were analyzed using a 3D semi-vectorial (TE) isotropic simulation, with 40 pts/μm in the x-direction and 45 pts/μm in the y-direction, using the commercial software package OptiBPM 6.1 [50]. The mesh values were determined using a convergence analysis.

To construct the tapers and bends of the device, it was necessary to consider waveguide layout issues. It is well-known that that in curved waveguides the fundamental mode is shifted to the outside edge of the curve [52]. This causes a mode field mismatch between a straight and curved waveguide, creating excess losses [53]. This mismatch is commonly reduced by offsetting the two waveguides at the junction and

possibly increasing the width of the straight waveguide [52]. We use a fourth-order polynomial to parameterize waveguide bends (and tapers):

$$y = \left(\frac{1}{2} t^4 - t^3 \right), \qquad [34]$$

where $t=x/L$, for a waveguide of length L. This equation only describes half of a full curve. The full curve, of length $2L$ and height h, is obtained by a reflection of this equation.

The specific parameterization is determined under the constraint that there should be no discontinuity in the radius of curvature at the junction with the straight waveguide. Thus, we define the curve such that the radius of curvature is infinite at the ends, where the curve joins the straight waveguide. The radius of curvature, R, is given by:

$$R = \frac{\left[x'^2 + y'^2 \right]^{3/2}}{x' y''}, \qquad [35]$$

where x' is the first derivative of x with respect to t, and y' and y'' are the first and second derivatives of y with respect to t. When applied to this waveguide, the radius of curvature is found to be:

$$R = \frac{\left[L^2 + h^2 \left(2t^3 - 3t^2 \right)^2 \right]^{3/2}}{Lh\left(6t^2 - 6t \right)}. \qquad [36]$$

It can be seen that in the limit as $t \to 0$, and $t \to 1$, $R \to \infty$, and there is an infinite radius of curvature at the end points.

The complete curve is described in a piecewise fashion, from $0 < x < L$ and $L < x < 2L$, and the origin is assumed to be in the upper left corner. The first equation is essentially the same as defined in Equation 34 except with a small vertical offset. The second equation is the same except mirrored in the line $x=L$ and $y=-h/2-h1$, where $h=h2-h1$. The exact equations for this curve are:

$$y = \begin{cases} h\left[\frac{1}{2}\left(\frac{x}{L}\right)^4 - \left(\frac{x}{L}\right)^3\right] - h1 & 0 < x < L \\ -h\left[\frac{1}{2}\left(\frac{-x+2L}{L}\right)^4 - \left(\frac{-x+2L}{L}\right)^3\right] - h1 - h & L < x < 2L \end{cases}$$

[37]

This curve is shown applied to the output curve of the waveguide splitter in Figure 34. To apply it to a taper, the lower boundary can be defined with Equation 37, and the upper boundary can be defined as the mirror image along the propagation axis of the lower boundary curve.

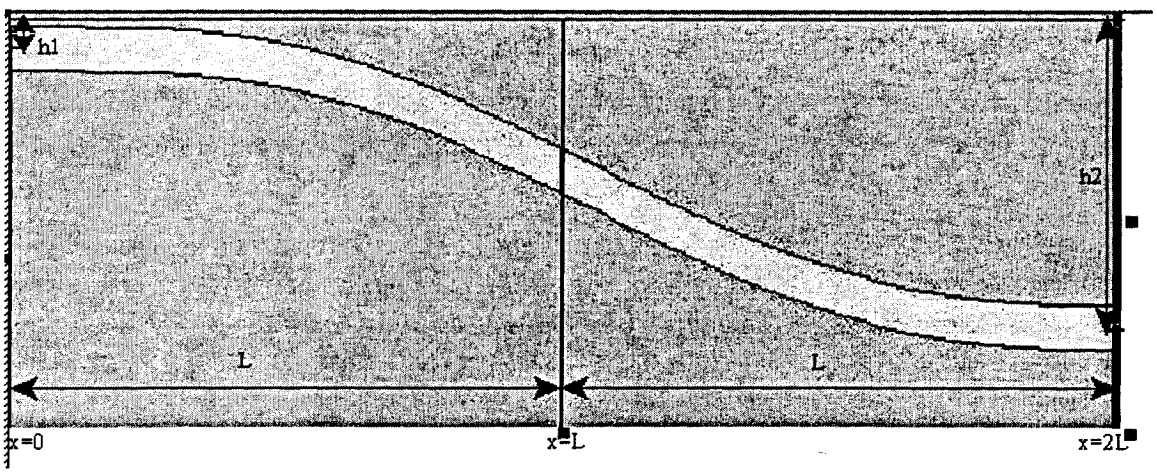

Figure 34 Fourth-order polynomial waveguide

Due to the computational intensity of the BPM calculations, the bends and tapers were optimized in a piecewise fashion. Each bend or taper was created using the fourth-order polynomial described above, and then the length was varied until an optimal (lowest loss) value was achieved, including absorption loss.

The first geometry to be optimized was for a junction with an 8μm wide single-ridge width, a 2μm gap, and 2.25μm dual-ridge widths. Since the 2.25μm wide dual-ridge waveguides at the junction needed to be tapered out to a width of 4μm as well as be separated, it was initially decided to taper and separate the waveguides simultaneously. However, the 2.25μm waveguide ridge was not wide enough to effectively guide the mode around any waveguide bend without large bending losses. Instead, the design was modified so that the 2.25μm waveguides at the junction would taper out to 4μm waveguides before separating. The gap between them would remain fixed at 2μm throughout this taper section. Figure 35 illustrates this dual-ridge taper. When using this taper with output waveguides of 1.5mm length (which had not as yet been optimized for minimal bend loss), the excess loss dropped from 2.7 dB to 1.5 dB, demonstrating the necessity of maximizing optical confinement in the bend region to minimize excess loss. In a series of BPM simulations, this taper length was optimized to 250μm, and the length of the separating output waveguides was optimized to 2750μm. These optimizations were performed by progressively increasing the length of the tapers and bends until a lowest loss value was obtained.

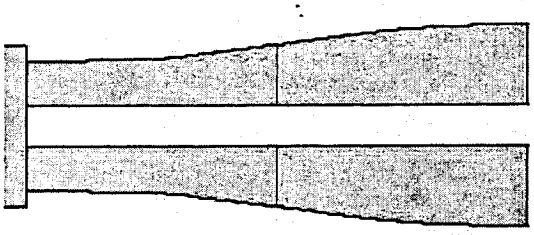

Figure 35 Dual-ridge taper from 2.25μm to 4μm maintaining a constant gap of 2μm

The input taper that increases the width of the single-ridge width from the standard value of 4μm to 8μm was found to have an optimal length of 250μm, giving a loss of 0.05 dB. A complete BPM simulation of the splitter, including all tapers and bends, shows that the total loss is 1.16 dB. A Fresnel calculation of the reflectivity can give a quick approximation of the worst-case amount of reflection at the waveguide boundary:

$$R = \left[\frac{n_{eff,II} - n_{eff,I}}{n_{eff,II} + n_{eff,I}} \right]^2 . \qquad [38]$$

The effective index of the single-ridge waveguide at the boundary is $n_{eff,I}$=3.1832 and the effective index of the dual-ridge waveguide at the boundary is $n_{eff,II}$=3.1817, where the imaginary portion of the index has been neglected for this calculation. These indices result in a Fresnel reflectivity of -72 dB, which shows that the backreflection at this interface will be negligible. With 0.24 dB of the total loss of the device due to the junction loss, this means that the majority of loss in this device (~0.92 dB) is due to absorption in the passive waveguides.

Next, the geometry that gave the optimal junction loss was simulated. This geometry had a single-ridge width of 10.5μm, a gap of

2μm, and dual-ridge widths of 2.25μm. For this geometry, the only difference was the single-ridge width chosen, meaning that the only portion of the power splitter that needed to be optimized differently was the input taper. For this geometry, the optimal input taper length was found to be 450μm, nearly double the previous taper length for the 8μm single-ridge width. The cost of having a larger single-ridge width is that a longer taper is required, and this results in a larger absorption loss.

The overall length of the design using a 10.5μm single-ridge width was 3.45mm, an increase of 200μm. A BPM simulation of this design determined that the total loss was 1.21dB, an increase of 0.05dB compared to the previous design using a single-ridge width of 8μm. This underscores the importance of considering global constraints (in this case, the absorption loss) when optimizing a system locally. The additional absorption loss was greater than the power saved at the modal overlap junction. This additional loss could be mitigated by either decreasing the absorption coefficient of the passive waveguide, or by increasing the confinement of the passive waveguide so that shorter bends and tapers would be required (assuming the absorption coefficient remains constant).

3.4. Overall Design of Power Splitter

The overall design of the low-loss power splitter is shown in Figure 36. The 4μm input ridge waveguide (the standard ridge width) is expanded to a width of 8μm over a length of 250μm. The input taper consists of two fourth-order polynomial curves. After this input taper, two ridges, each 2.25μm in width and separated by 2μm, continue parallel to the input waveguide. The outer edges of these ridges are tapered (again using the fourth-order polynomial curve) over a length of 250μm while the gap between them remains constant, until they are once again at the standard ridge waveguide width of 4μm. Then the two waveguides are separated

from each other using the waveguide shown in Figure 34 over a length of 2750μm. At the output of the device the two waveguides are separated by 50μm. The total design has a length of 3.25mm and the total loss, as calculated by OptiBPM [50], is 1.16 dB. The BPM simulation result is shown in Figure 37.

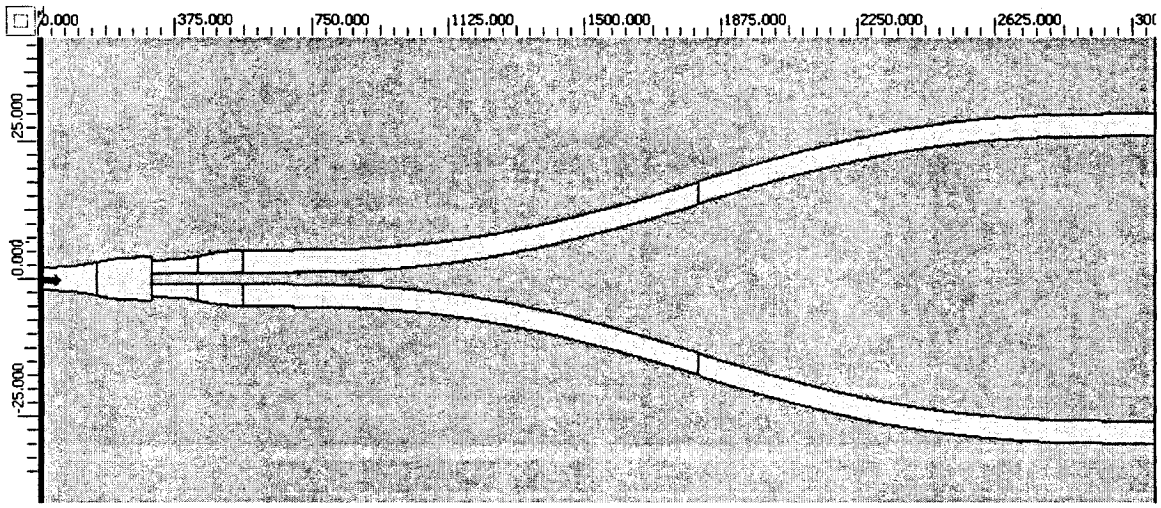

Figure 36 Complete 3dB splitter layout

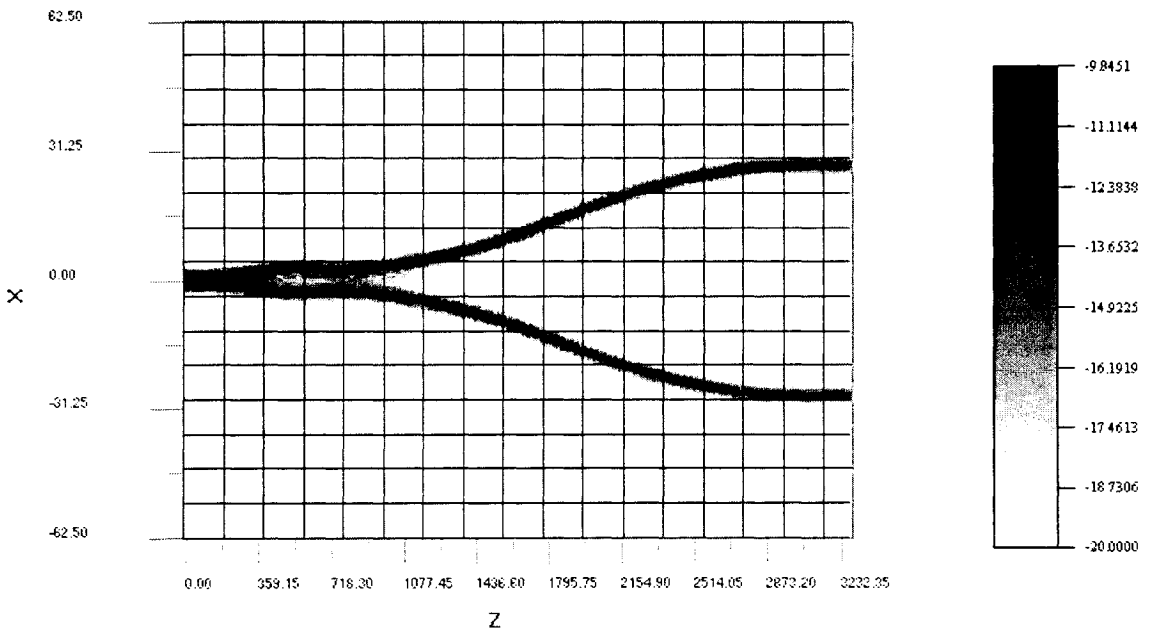

Figure 37 Optical field (in dB) of the complete 3dB power splitter calculated using BPM

4. Modeling the Active Region

To achieve optical switching, the outputs of the 3dB power splitter described in Section 3.4 are amplified or absorbed by straight SOA regions. Figure 38 shows the complete layout of the 1x2 SOA-based switch. If, for example, it is necessary to switch the signal into the upper output waveguide (output 1), the SOAs would be set so that the upper waveguide is amplifying (or transparent) and the lower output waveguide (output 2) is absorbing. Lateral n-contacts and a p-contact on top of the active ridge are connected to a voltage source which provides carrier injection. In this section, the affect of this carrier injection on the SOA regions of the switch are examined in more detail.

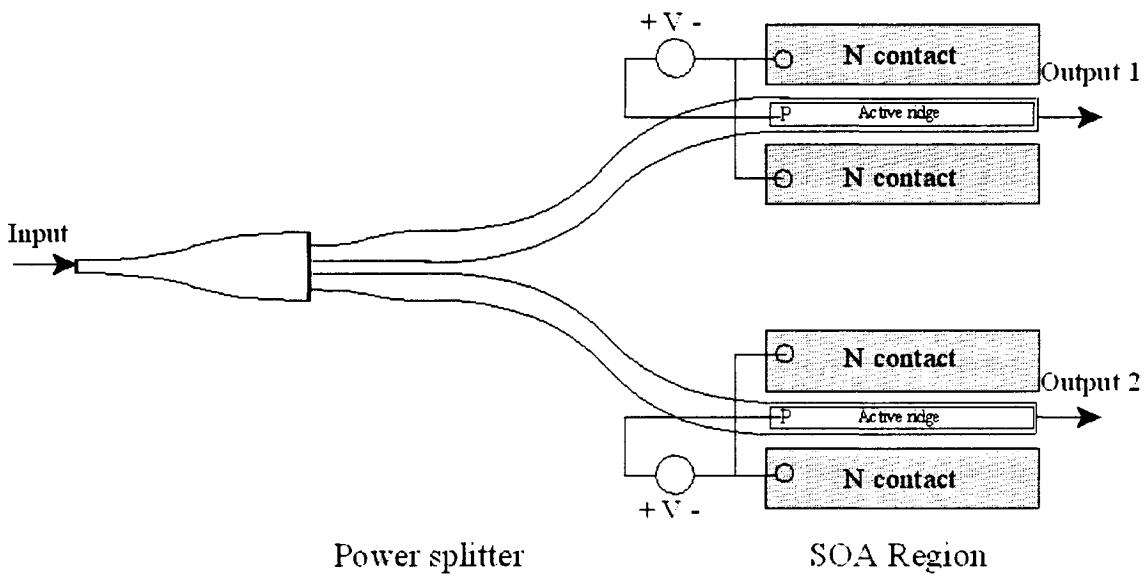

Figure 38 Layout of the complete1x2 SOA-based integrated optical switch

4.1. Carrier Injection in Semiconductor Materials

The goal of carrier injection in this design is to create a modest gain in the active region of the switch. However, when carriers are injected into a semiconductor material, other competing effects will occur. In this section, the various effects and interactions related to carrier injection are described.

4.1.1. Gain Mechanisms

To achieve light amplification in a direct-gap semiconductor medium (such as InGaAsP), it is necessary to have a higher proportion of excited electrons in the conduction band compared to the valence band. This condition, known as population inversion, can occur when excess electrons are injected into the semiconductor material. When it is satisfied, the mechanism of light amplification, *stimulated emission*, becomes predominant.

Stimulated emission occurs when incident radiation induces an electron in the conduction band to fall to a lower energy level in the valence band (or more generally, a particle in an upper energy level falls to lower energy level), releasing the excess energy in the form of a photon of the same frequency and phase as the photon that induced the transition and preserving the original photon. The rate of stimulated emission for a given population of excited particles, N, is:

$$\frac{\partial N}{\partial t} = -B_{21}\rho(\nu)N \,, \qquad [39]$$

where B_{21} is a constant of proportionality known as the Einstein B coefficient (the subscript 21 indicates a transition from a higher energy

state E_2 to a lower energy state E_1), and $\rho(\upsilon)$ is the radiation density of photons of frequency υ. This simple differential equation, of the form of Newton's Law of Cooling, can be solved to yield:

$$N = N(0)e^{-B_{21}\rho(\nu)t}, \qquad [40]$$

where $N(0)$ is the excited particle population at time 0. As can be seen from Equation 40, stimulated emission causes an exponential decay in the population of excited particles. Therefore it is necessary to have continuous pumping of the gain medium (either through an external laser source or by carrier injection) to maintain population inversion.

Another photon-producing mechanism is known as *spontaneous emission*. Spontaneous emission, like stimulated emission, also occurs when a particle in an excited state drops to a lower energy level, releasing the excess energy in the form of a photon. Unlike stimulated emission, however, spontaneous emission is not induced by incident radiation, but occurs naturally as a system of excited states radiatively relaxes to a lower energy level. The photons produced by spontaneous emission have variable phases and propagation directions (and are in practice of broader bandwidth), and hence do not contribute to signal amplification but rather act to reduce the signal-to-noise ratio.

The rate of spontaneous emission, for a population of N particles in an excited state (e.g. electrons in the conduction band), is:

$$\frac{\partial N}{\partial t} = -A_{21}N, \qquad [41]$$

where A_{21}, known as the Einstein A coefficient, is a constant of proportionality, similar to the Einstein B coefficient. As with the equation for stimulated emission, this differential equation can be solved to yield:

$$N(t) = N(0)e^{-\frac{t}{\tau_{21}}}. \qquad [42]$$

where $\tau_{21} = A_{21}^{-1}$ is the lifetime of the spontaneous decay. As can be seen, the number of excited particles, N, decreases exponentially due to spontaneous emission, reducing the number of excited particles available for stimulated emission. Some of the photons produced by spontaneous emission can couple into the desired amplified optical mode, inducing further stimulated emission reactions and generating noise. This effect is known as amplified spontaneous emission (ASE), and can be calculated by the following derivation from [54].

For a gain medium, the intensity of light increases exponentially over distance:

$$I(z) = I(0)e^{\gamma(\nu)z}. \qquad [43]$$

It can be shown that the gain constant, $\gamma(\upsilon)$, for a given lineshape function $g(\upsilon)$, index of refraction n, and frequency, υ, is given by:

$$\gamma(\nu) = N\frac{c}{8\pi n^2\nu^2\tau_{21}}g(\nu). \qquad [44]$$

To calculate the effect of amplified spontaneous emission noise, consider a gain medium of length L and area A, with a population density of N_2 in the upper state and N_1 in the lower state. A beam with power P is input and a photodetector is placed at the output. For an element dz

within the gain medium, the amount of spontaneously emitted power, P_N, at a particular frequency, ν, is:

$$P_N = \frac{N_2 h \nu A dz}{\tau_{21}} \qquad [45]$$

where h is the Planck's constant, h=6.626 x 10^{-34} Joule-seconds. However, only a portion of this optical power contributes to the noise. The noise power emitted by an elemental volume (Adz) must fall within the optical spectrum $\Delta\nu$ and solid angle $d\Omega$:

$$dP_N = \frac{1}{2} \frac{N_2 h \nu g(\nu) \Delta \nu A}{\tau_{21}} \frac{d\Omega}{4\pi} dz \qquad [46]$$

In Equation 46 the one-half term comes from the assumption that half of the spontaneous emission noise is filtered out due to polarizers in front of the photodetector. The smallest solid angle that can be used is the solid angle per mode:

$$d\Omega = \frac{\lambda^2}{n^2 A}. \qquad [47]$$

If this is substituted into Equation 46, and the gain constant given in Equation 44 is also used, the spontaneous emission power generated by an elemental gain medium volume becomes:

$$dP_N = \frac{N_2 \gamma h \nu}{N_2 - N_1} \Delta \nu. \qquad [48]$$

To obtain the total power seen at the photodetector, the power of the amplified signal and the power of the spontaneous emission noise is added:

$$P(z) = P_0 e^{\gamma z} + \mu h \nu \Delta \nu (e^{\gamma z} - 1) . \qquad [49]$$

Here $\mu = N_2/(N_2 - N_1)$, and is known as the population inversion factor. The second factor in Equation 49 represents the spontaneous emission noise. It can be seen that the larger the pumping (represented by μ) and the larger the frequency, the larger the spontaneous emission noise. The noise is also proportional to the gain, $G = \exp(\gamma z)$.

4.1.2. Absorption

Light absorption in a semiconductor occurs when a carrier (electron or hole) interacts with an incident photon and is raised to a higher energy level. This often involves a transition between the valence and conduction band of the semiconductor material, since at thermal equilibrium there are an equal proportion of carriers above and below the Fermi level in the bandgap. However, photon-absorbing intraband carrier transitions are also possible.

There are three major phenomena that affect the absorption of photons in a carrier-injected semiconductor material: bandfilling, bandgap shrinkage, and free-carrier absorption [55].

Bandfilling occurs when there is a high concentration of electrons in the conduction band, as in the case of a large population inversion. When this occurs, the lowest energy levels of the band are filled and photons will require a higher energy (and therefore frequency) to be absorbed. The

effect of bandfilling is to restrict absorption of higher wavelength photons. Bandfilling also occurs for an excess amount of holes in the valence band, but it primarily describes an excess concentration of electrons since there is a lower density of states in the conduction band.

Bandgap shrinkage has the opposite effect of bandfilling – it allows photons with an energy below the bandgap to be absorbed. Shrinkage of the bandgap occurs when a large concentration of electrons (or holes) in the conduction (or valence) band have overlapping wavefunctions. Coulomb effects and the Pauli exclusion principle cause the electrons (or holes) to repel each other, effectively decreasing the energy gap. With a decreased energy gap, lower energy photons are able to be absorbed. For high carrier concentrations, the bandgap shrinkage is inversely proportional to the cube of the carrier concentration. For lower carrier concentrations (for InP, $\sim 10^{16}$ cm^{-3}), the bandgap shrinkage is often approximated to be zero, or determined empirically as a percentage of the bandfilling effect.

Free-carrier absorption, or the plasma effect, is due to intraband absorption of photons as opposed to the interband absorption that is affected by bandfilling and bandgap shrinkage. This effect occurs when free carriers, i.e. electrons in the conduction band or holes in the valence band, absorb a photon and move to a higher energy level within the same band. The absorption change is directly proportional to the concentration of free carriers. The plasma effect is typically smaller than the effect of bandfilling and bandgap shrinkage.

The changes in the absorption of a semiconductor material caused by carrier injection also cause changes in refractive index. This fact has been exploited to design variable refractive index regions for the switch geometries outlined in Section 2.5. The relation between a change in

absorption, Δa , and a change in refractive index, Δn, for a particular radian frequency, ω, is governed by the Kramers-Krönig relation:

$$\Delta n(\omega) = \frac{hc}{\pi} P \int_0^{\infty} \frac{\Delta\alpha(\omega')}{h\omega'^2 - h\omega^2} d\omega' \quad . \qquad [50]$$

Here the P represents the principal value of the integral and ω' is a dummy variable used for integration.

4.2. Active Waveguide Structure

The SOA region of the switch is created by adding layers to the passive waveguide (described in Table 1) to create a p-i-n region. Carriers injected through a p-contact and two lateral n-contacts into the active layer cause this layer to change from an absorbing material at zero-bias, to an amplifying material. When the amplification within this layer is sufficiently high, there is an overall modal gain. Table 4 lists the active layers that are used.

Number	**Layer**	**Material**	**Refractive Index**
9	P-cap	InGaAs	3.516088
8	P-contact II	InP	3.170258
7	P-contact I	InP	3.172363
6	Active	InGaAsP	Variable

Table 4 Single-mode vertically-integrated active waveguide layer structure

The active layer of the vertically-integrated structure consists of an InGaAsP material chosen to provide a small amount of strain when

embedded in the surrounding InP layers. This strain helps to reduce polarization sensitivity. InGaAsP has a bandgap of 1.55μm, which is a useful wavelength for telecommunications purposes since it is the wavelength of minimum absorption for standard optical fibers. Both InP and InGaAsP are direct-gap semiconductor materials. In these materials, an electron can move directly from the valence band to the conduction band without a phonon (quantum of vibrational lattice energy) to facilitate the transition, making this transition much more likely. Figure 39 shows the layer stack for the vertically-integrated active region.

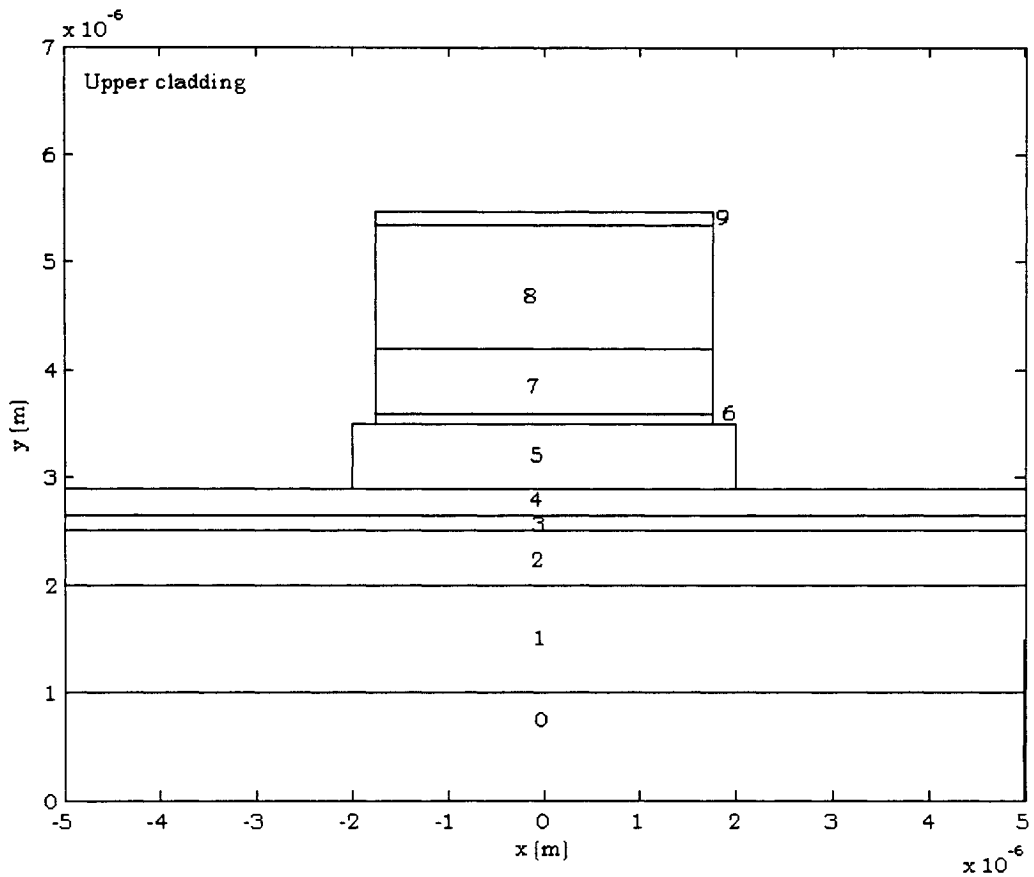

Figure 39 Active waveguide geometry of the SMVI material system

4.3. OptiHS Material Simulation Results

To obtain the overall gain of this active region, it was necessary to first determine the material properties of the active layer. The geometry of the active region was designed so that this active layer experienced the greatest change in refractive index with carrier injection. By determining the effects of carrier injection on this material, it will be possible to estimate the overall modal gain or loss.

The active layer is composed of tensile-strained bulk InGaAsP. The tensile strain reduces the polarization dependence of the gain/loss. To determine the dependence of the complex refractive index (and material gain) on carrier concentration and wavelength, simulations were performed using OptiHS [56].

OptiHS is a heterostructure modeling program that is capable of calculating the effect of carrier injection in a semiconductor material on the complex refractive index. Given the material properties of the active layer, OptiHS first determines the band structure using the Kane and Kohn-Lüttinger models. The band structure includes a non-parabolic conduction band with two side X- and L-valleys, and three parabolic valence bands, the light, heavy and split-off. The bandgap shrinkage and quasi-Fermi levels of the carriers are then calculated self-consistently, while many-body effects (such as free-carrier screening of the Coulomb interaction) are incorporated phenomenologically. Based on this distribution of carriers the rate of direct transitions (spontaneous and stimulated emission) and indirect transitions (phonon-or trap-assisted) is found. These rates can then be used to determine the imaginary portion of the permittivity, and thus the imaginary portion of the refractive index. The real portion of the refractive index is calculated from the imaginary portion using the Kramers-Krönig relation of Equation 50.

Figures 40 and 41 show the dependence of the real and imaginary components of the refractive index on wavelength and carrier concentration. It can be seen that the real part of the refractive index decreases with increasing wavelength and carrier concentration. The imaginary part of the refractive index also decreases with increasing carrier concentration, and converges to nearly zero for all carrier concentrations when the wavelength is sufficiently large. The active material is absorbing when the imaginary part of the refractive index is positive, and provides gain when the imaginary part of the refractive index is negative.

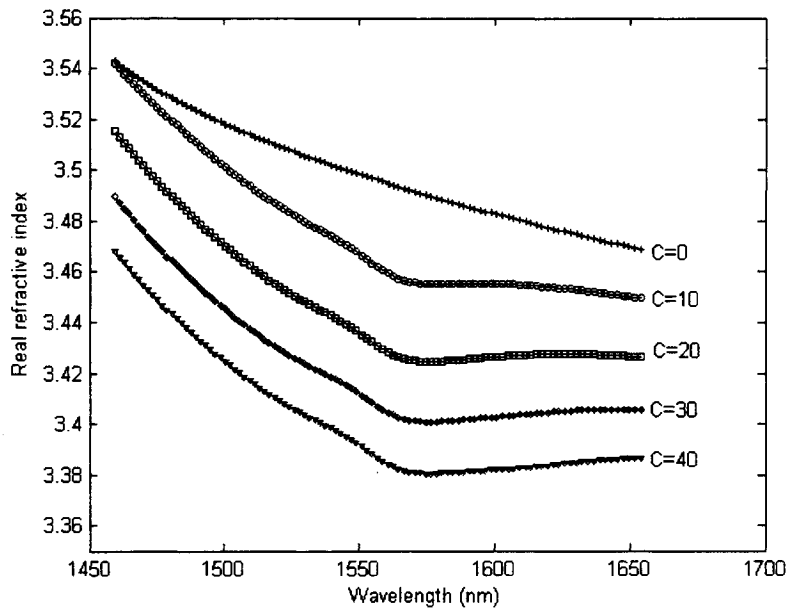

Figure 40 Dependence of the real refractive index on wavelength for carrier concentrations of C=[0,10,20,30,40] x 10^{17} cm^{-3} in the InGaAsP layer

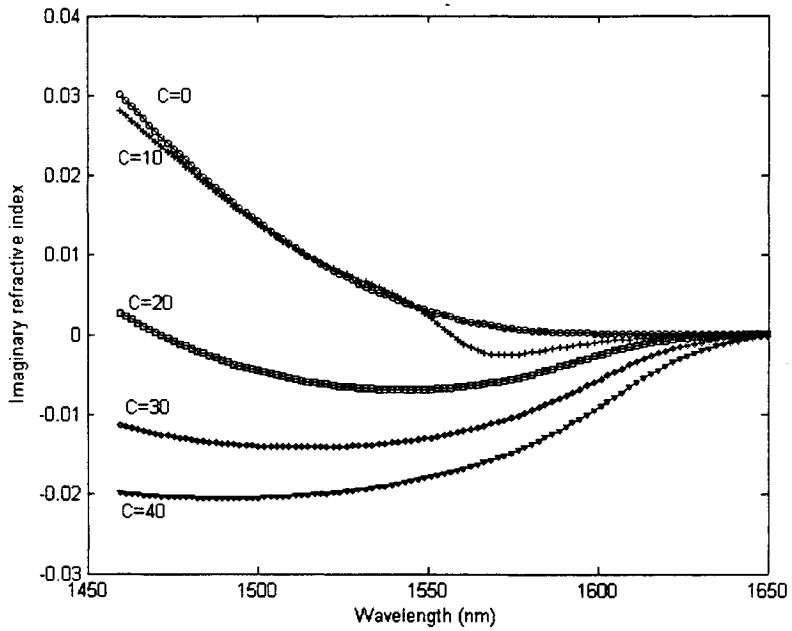

Figure 41 Dependence of imaginary refractive index on wavelength for carrier concentrations of C=[0,10,20,30,40] x 10^{17} cm^{-3} in the InGaAsP layer

The operating wavelength that was assumed for this device was 1550nm, so it is useful to see how the material behaves at this wavelength. Figures 42 and 43 show how the real and imaginary portions of the refractive index change depending on carrier concentration at a wavelength of 1550nm.

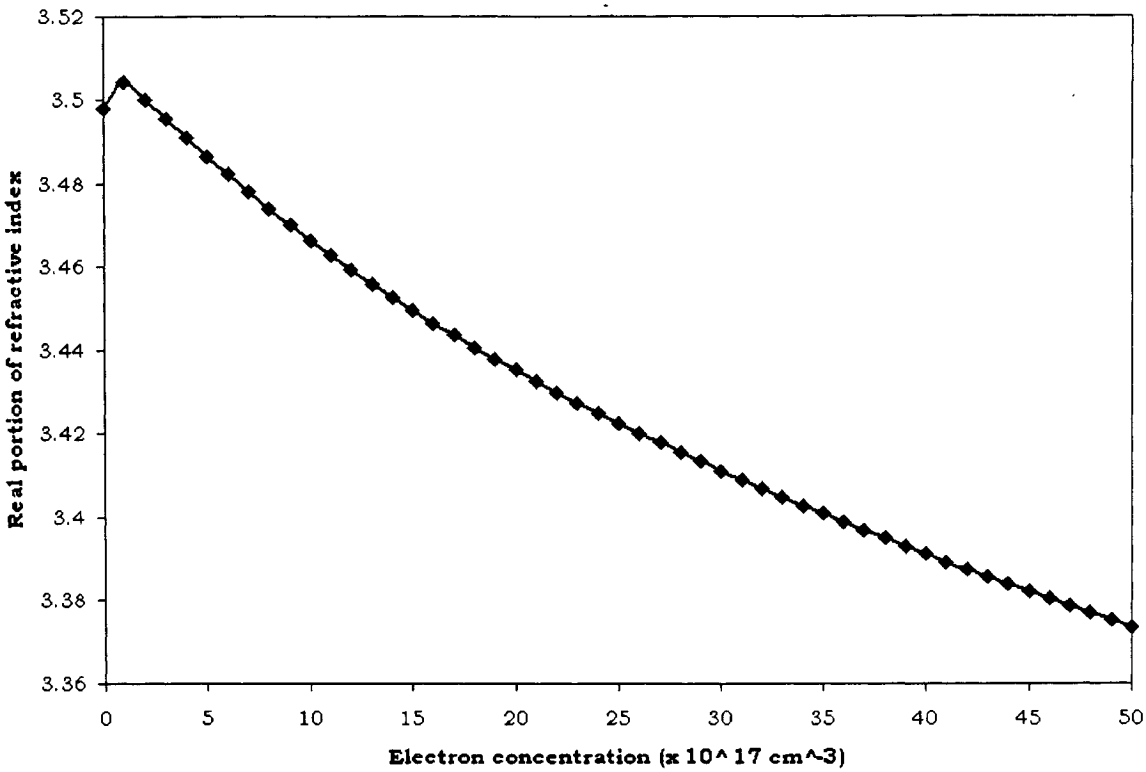

Figure 42 Dependence of the real refractive index on carrier concentration of the InGaAsP active layer at a wavelength of 1550nm

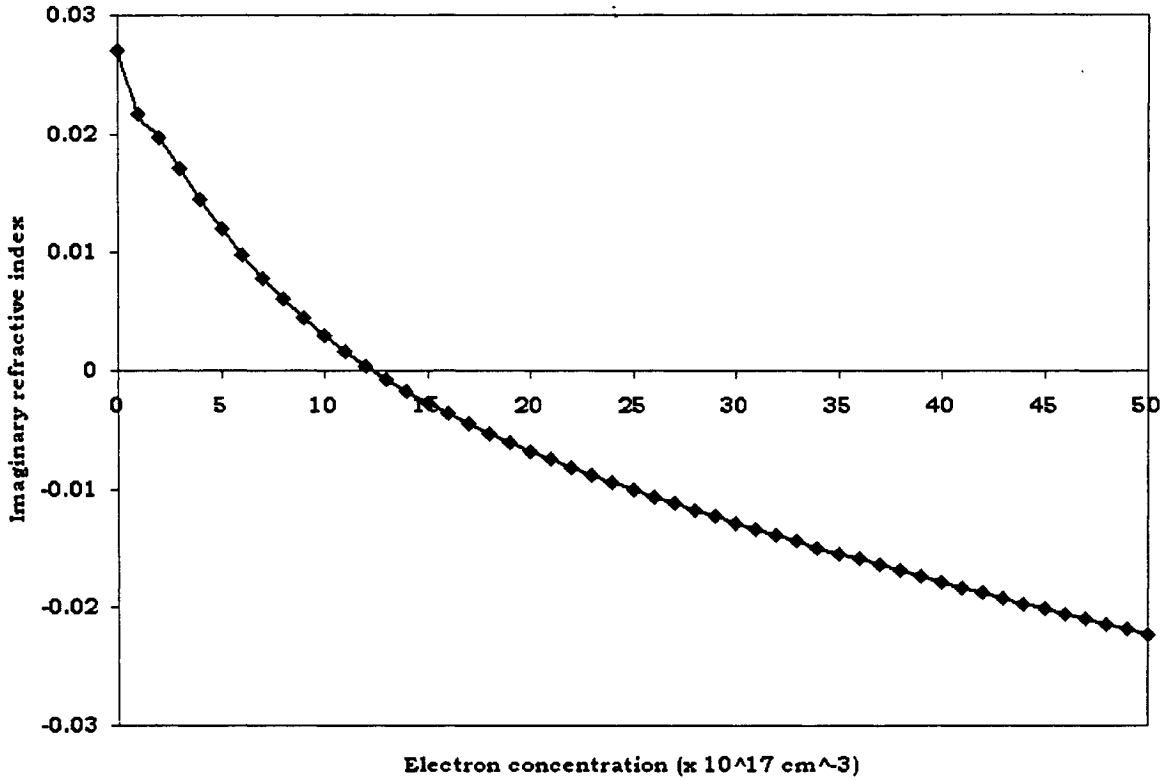

Figure 43 Dependence of the imaginary refractive index on carrier concentration of the InGaAsP layer at a wavelength of 1550nm

At the lowest carrier concentration (approaching zero), the real index (and therefore the modal confinement) and the absorption are the highest. As the electron concentration increases, the real index becomes smaller, and the imaginary index goes from positive to negative values. The point where the imaginary index is zero is the transparency point, where there is no amplification or absorption. This occurs at a carrier concentration of ~12 x 10^{17} cm^{-3}.

4.4. FEMLAB Finite-Element Simulation Results

The data shown in Section 4.3 were now applied to finite-element analysis of the active layer structure using FEMLAB. The complex refractive index of the active material for all electron concentrations of interest (from 10 x

10^{17} to 25 x 10^{17} cm^{-3}) was used in a finite-element modal analysis of the active waveguide.

The layer structure was divided into separate regions of varying mesh density, with the densest mesh (with a maximum element size of 0.1μm) in the centre region under the ridge where the majority of the mode is concentrated. Once again, the number of mesh elements was progressively increased until the eigenvalue of the modal solution converged to five decimal places. Figure 44 shows the adaptive mesh used to model the active structure.

The active layer (Layer 6 in Table 3) is the first layer on top of the passive ridge layer. It has a complex refractive index that will vary with the electron concentration in that layer. The change in index of the active layer was determined using OptiHS (see Figures 42 and 43). For each value of the active layer complex refractive index corresponding to a different electron concentration, the mode of the active geometry was solved in FEMLAB. The imaginary portion of the propagation constant, β, of each mode was used to find the gain or loss, G, of a straight section of that refractive index profile of length z, according to the relation:

$$G = 10\log\left(e^{-2\Im(\beta)z}\right). \qquad [51]$$

An example of a 2D FEMLAB modal solution for the active layer geometry is shown in Figure 45.

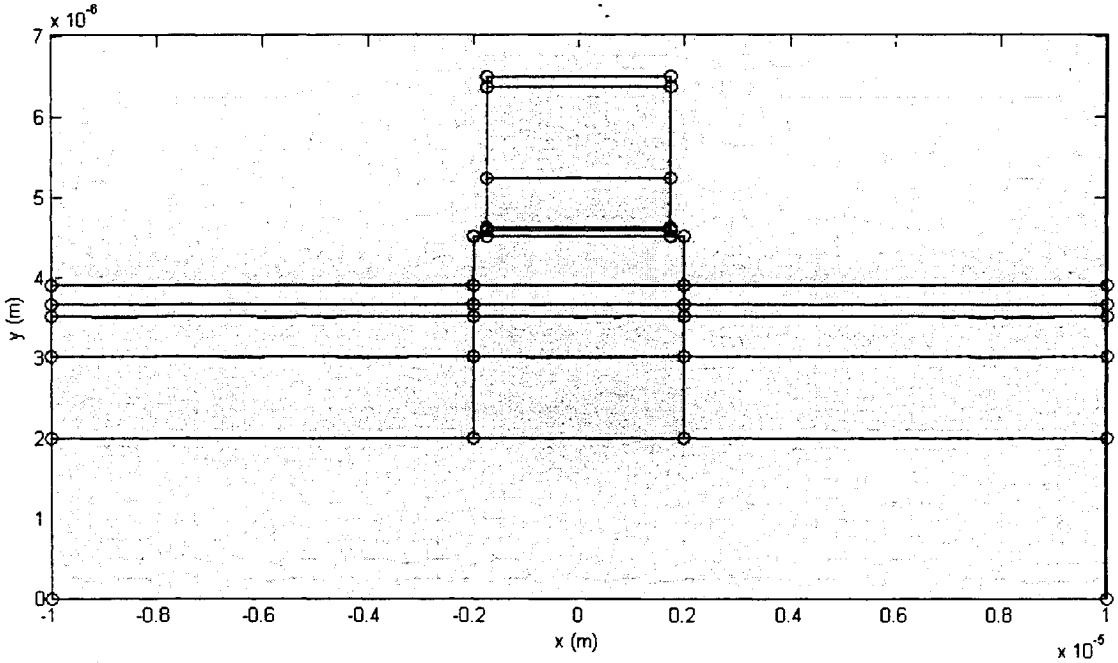

Figure 44 Adaptive mesh used for vertically-integrated active layer geometry

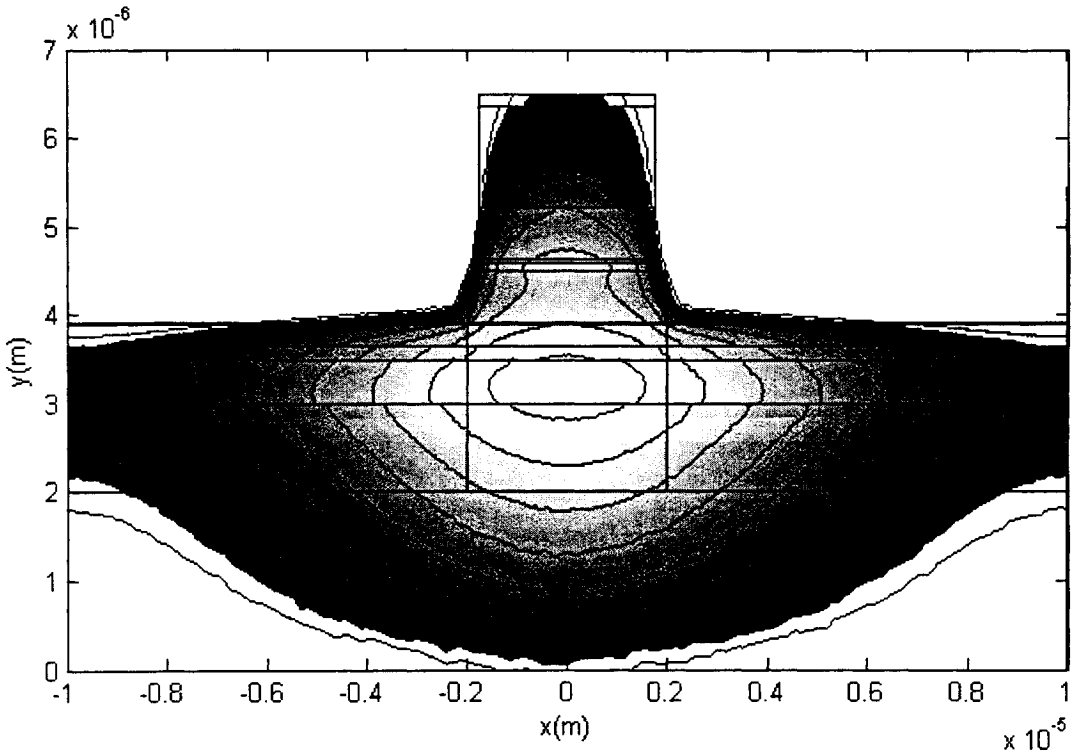

Figure 45 Logarithmic electric-field profile (TM mode) of the vertically-integrated active waveguide (5 dB contours)

The effect of carrier concentration on the gain or loss of the active region as determined by these calculations is shown in Figure 46. Using linear interpolation, the point of transparency is determined to occur at a carrier concentration of 14.68 x 10^{17} cm^{-3} for the TM mode and 15.34 x 10^{17} cm^{-3} for the TE mode. Thus the transparency point is reasonably polarization insensitive. The carrier concentrations required to reach transparency are higher than for the active layer in isolation (12 x 10^{17} cm^{-3}, from Section 4.3), because in this geometry the active layer is now embedded in lossy layers.

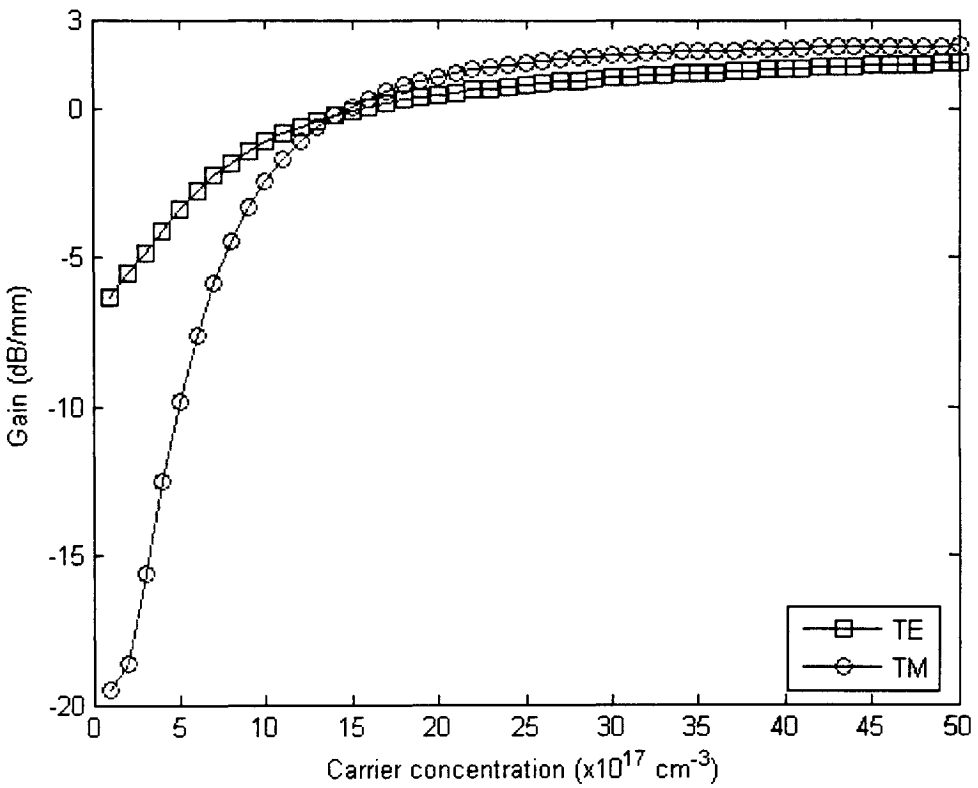

Figure 46 Active region gain vs. carrier concentration for the TE and TM modes

While this graph shows the gain increasing continually up to carrier concentrations of 50 x 10^{17} cm^{-3} (where the TM gain is ~2 dB), in reality phenomena such as thermal effects that become prominent at high carrier concentrations would lower these gain values considerably. This FEMLAB

simulation gives valuable insight into the performance of the active region at lower carrier concentrations, particularly when transparency occurs. However, to properly simulate this active region, a more sophisticated model that includes these effects would be required.

These FEMLAB simulations can also provide information on the confinement of the mode in the active layer. By taking the ratio of the optical power found only in the active layer over the total power of the mode, the active layer confinement, Γ, can be found. Figure 47 shows the confinement for the TE and TM polarizations. It can be seen that the TM polarization has a greater confinement in the active layer, which explains the higher gain and loss for the TM mode, and why the TM mode requires a smaller carrier concentration to reach transparency.

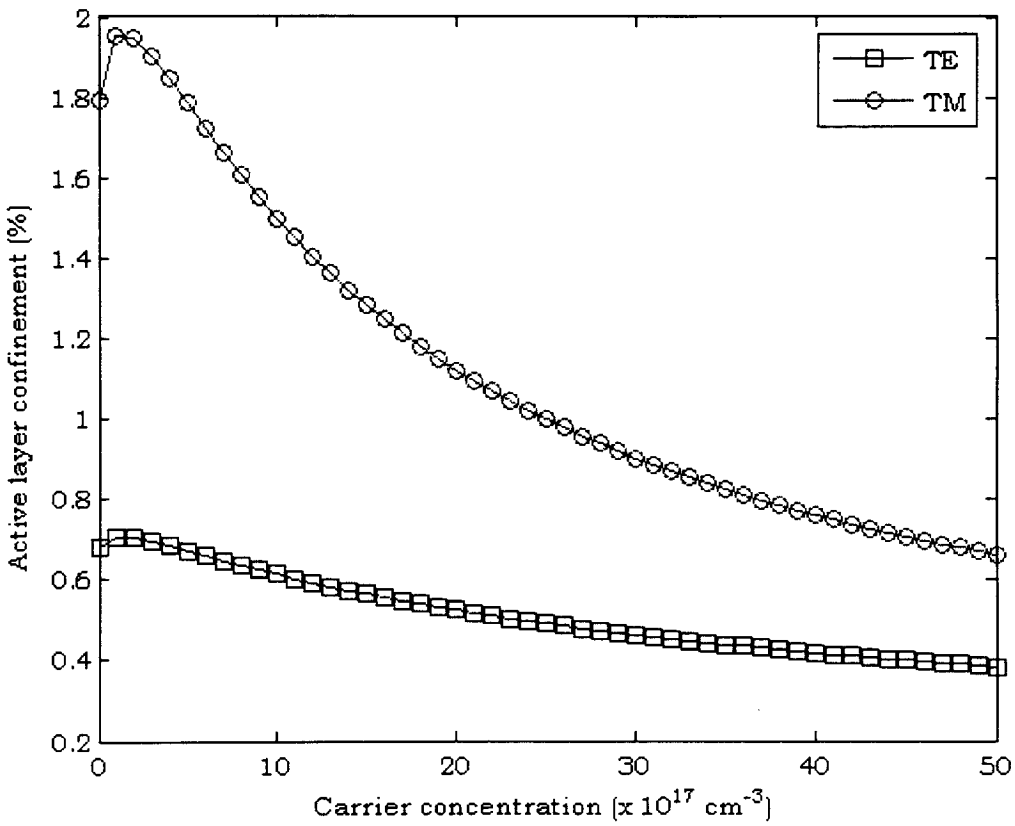

Figure 47 Active layer confinement vs. carrier concentration for the TE and TM modes

It was stated in Section 2.6 that the low confinement of the mode in the active layer resulted in low backreflection and coupling loss at the junction between the active and passive regions. This assertion can now be confirmed by performing a modal overlap calculation using Equation 32 and performing a Fresnel calculation using Equation 38 with the modal solutions of the active and passive waveguide. For a carrier concentration of 15 x 10^{17} cm^{-3}, which is the approximate transparency point for the active waveguide, the excess loss at the junction between the active and passive waveguide was found to be 0.20 dB for the TE polarization and 0.28 dB for the TM polarization. The backreflection for both the TE and TM polarizations was found to be -77 dB. These numbers confirm that the coupling loss and backreflection at the passive/active waveguide interface will not severely affect the performance of the overall device.

5. Increasing Switch Port Count

5.1. Nonblocking 2x2 Switch Architecture

The 1x2 switch that has been designed can now be used as a building block for larger switching matrices. The first that will be examined is the 2x2 switch.

A nonblocking switching architecture allows a connection to be made between any two ports, regardless of what connections have already been established. Nonblocking switches provide the flexibility required for the most recent agile photonic networks. To create a nonblocking 2x2 switch architecture using 1x2 switches, the geometry shown in Figure 48 can be used.

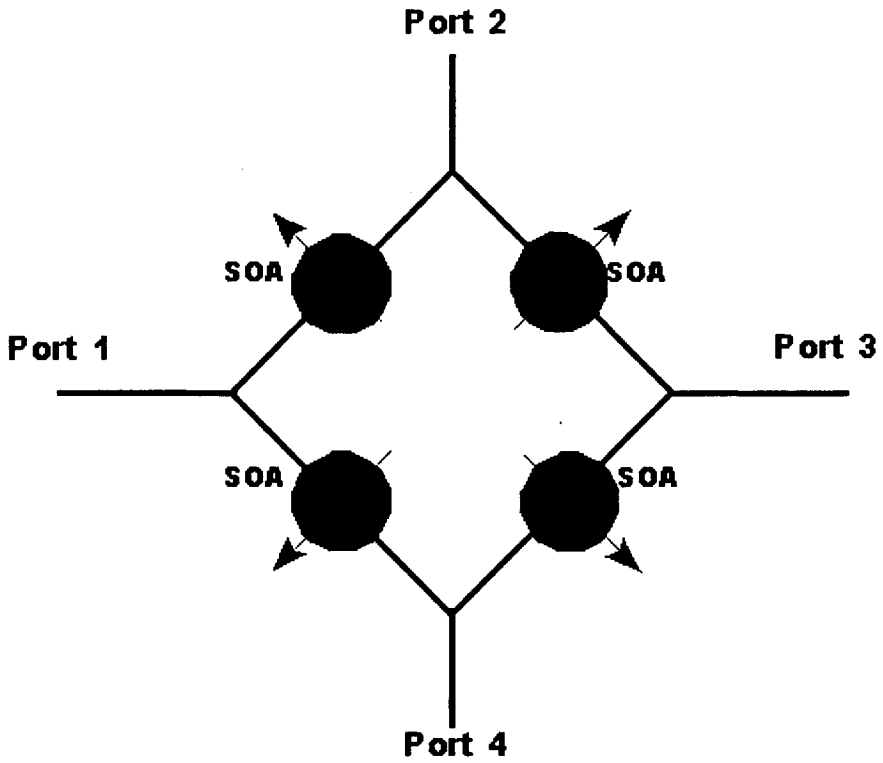

Figure 48 Nonblocking 2x2 switch architecture using 1x2 switch elements

Light entering any of the four ports shown in Figure 48 is split using a Y-branch power splitter and then either attenuated or amplified by the SOAs in the common paths before reaching an output port. While this configuration provides nonblocking operation, the SOAs would need to be set carefully to avoid imbalanced power at the output ports, since either one or two SOAs could be in the connection path. In this configuration, any two ports could be used as inputs and any two ports could be used as outputs.

The large angles implied in Figure 48 of 45 degrees for each of the Y-branches would be impractical to realize with the weakly-guiding waveguide structure being used (see Figure 31). For the Y-branch power splitter designed in Section 3.3, the angle of the output waveguides is only

~0.5 degrees, with a total splitter length of 3.25mm. To extend these waveguides to a 45 degree angle and maintain a minimal bending loss would require waveguides on the order of centimeters in size. To compensate for this, etched mirrors could be used to create the compact 45 degree bending angle required. These mirrors could be placed at the end of the output Y-branch waveguides once the two output modes have been isolated from each other. This configuration is shown in Figure 49.

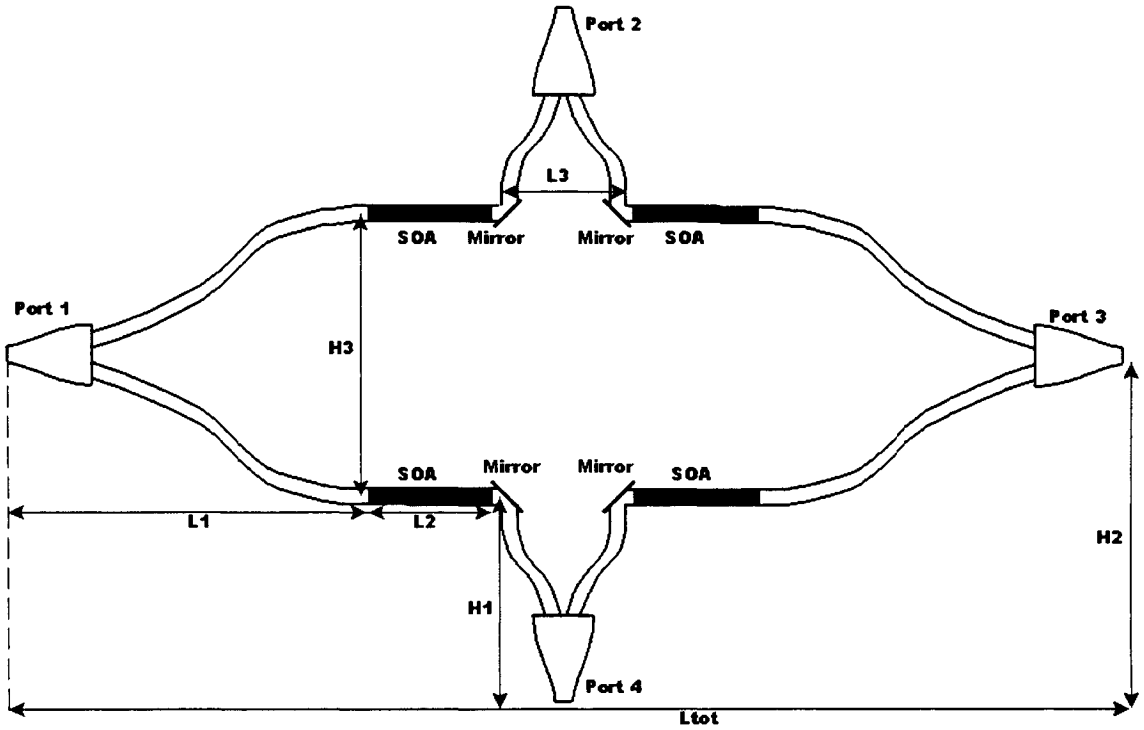

Figure 49 Implementation of a 2x2 switch with SMVI waveguides

The length, L1, of the east/west splitters (ports 1 and 3) is the standard 1x2 power splitter length determined in Section 3.3, and would depend on the length of the straight SOA sections. However, the height of the north/south splitters need not be the same length. Since there are no SOAs required at the end of these power splitters, the separation of the output waveguides is not determined by the size of electrical contacts required, but by the separation required to achieve optical isolation, which would likely be less than 50 μm.

5.2. Nonblocking 4x4 Switch Architecture

A nonblocking 4x4 switch can be realized using either 1x2 or 2x2 switches as building blocks. Figure 50 illustrates how 1x2 switches can be combined to create a nonblocking 4x4 switching fabric.

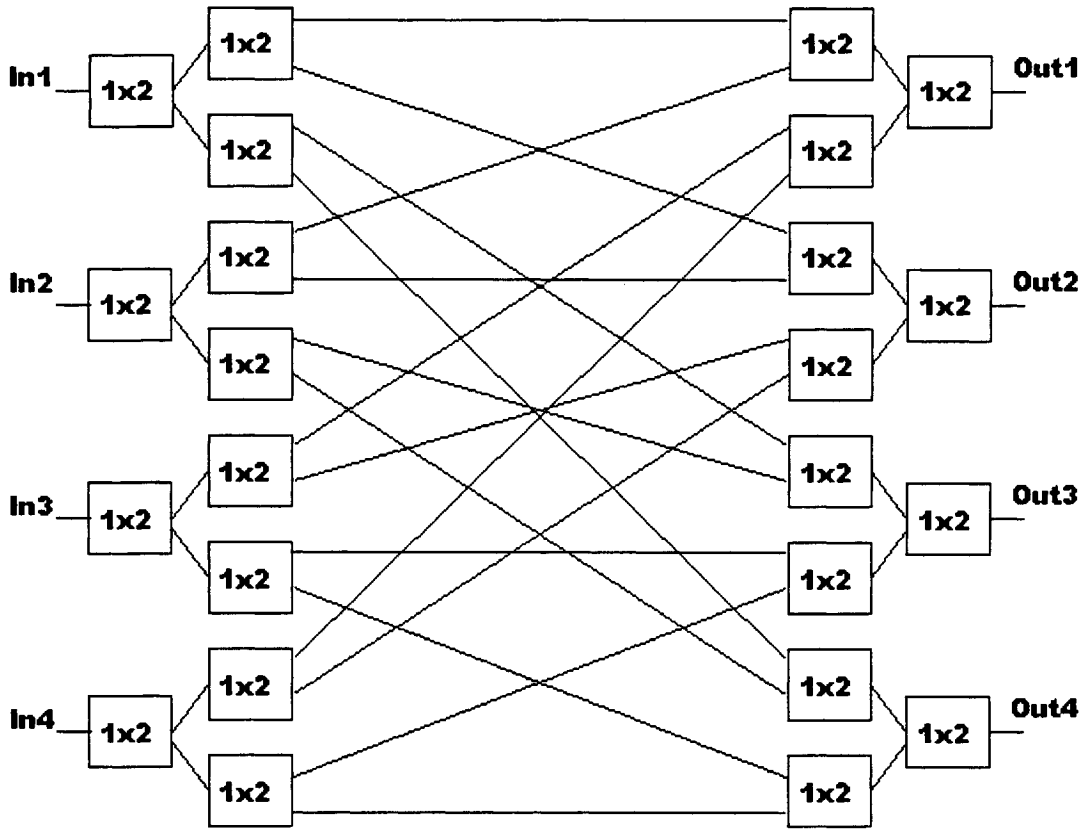

Figure 50 Nonblocking 4x4 switch composed of 1x2 elements

Examination of Figure 50 shows that this implementation of the 4x4 switch requires 24 3dB power splitters and 32 SOAs. This assumes that each connection between 1x2 switches in the middle of the diagram uses one SOA, not two SOAs, one for each individual switch.

While this configuration provides nonblocking operation, with an explicit connection between every input and output port, it is not the optimal design. A nonblocking configuration composed of 2x2 switch

elements can be constructed that requires fewer SOAs. This is done using a 4x4 instantiation of the generalized topology known as the Clos network [57]. This configuration, shown in Figure 51, requires six 2x2 nonblocking switching elements. Since each 2x2 element, as shown in Section 5.1, requires four power splitters and four SOAs, this 4x4 switch would require a total of 24 power splitters and 24 SOAs, a savings of eight SOAs compared to the first design.

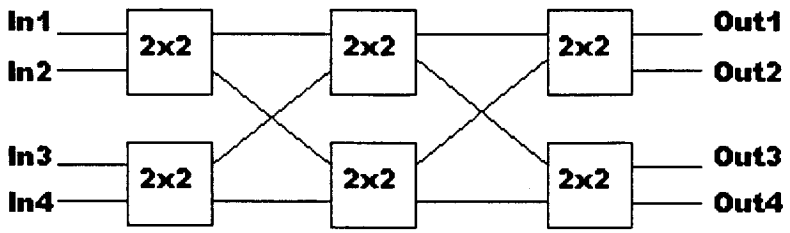

Figure 51 Nonblocking 4x4 switch using Clos network topology

Once again, due to the relatively sharp angles involved, mirrors would be required to make this design practical.

6. Conclusions

This thesis has described the design and final geometry of a monolithically integrated 1x2 optical switch. A new method for designing Y-branch type integrated power splitters has been developed, the Modal Overlap Method, and applied to a simple silica buried-core material system as well as a complex vertically-integrated active/passive waveguide system. The 1x2 switch configuration has been simulated using finite-element and BPM techniques. Possible layouts for a 2x2 and 4x4 nonblocking optical switch using the 1x2 switch as a building block were also explored.

6.1. Switch Performance

The 1x2 switch has not yet been manufactured, but some indications of its performance can be determined from the simulations that have been

performed during its design. The input signal will experience ~4.2 dB of excess loss while propagating through the power splitter portion of the switch. This includes 3 dB of splitter losses and 1.2 dB of excess losses, as measured by BPM simulations. As Figure 46 shows, the SOA regions of the switch are at most capable of providing ~2dB of gain with an active/passive junction loss of 0.3 dB, for a total excess loss of 2.5-3.5 dB. This is higher than the desired value of 1 dB for the excess loss, and not considering additional coupling loss that would occur. It should also be noted that the SOA gain is dependent on the input power, and saturation of the output power could occur for a large input signal. This has not been modeled in Section 4. However, assuming no saturation, these values indicate that the reverse-biased SOA region would require at least 34dB of absorption to achieve an extinction ratio of -30dB. Backreflections should have minimal impact on the crosstalk of this device since they were estimated, using a Fresnel calculation, to be -77 dB at the active/passive interface and -72 dB at the single-rib/dual-rib power splitter interface.

As the FEMLAB simulations indicated, the power splitter section has a very low PDL. If the SOA regions are biased to operate at the transparency point, the PDL will be very low (see Figure 46), and there should be no difficulty in achieving the PDL target of < 1dB. Operating at the transparency point will also ensure that the amplified spontaneous emission noise will be minimized, according to Equation 49.

Finally, this switch was designed to operate at a wavelength of 1.55 μm, in the middle of the C-band. More complete material dispersion data is required to simulate the wavelength dependencies. However, testing of the completed device will show how deviation from this design wavelength affects the performance of the switch.

6.2. Future Work

This switch is currently in the process of fabrication. Once it has been manufactured, it will be tested to see how it performs compared to the specifications laid out in Table 2. These data can be used to further refine this proof-of-concept 1x2 switch design. More simulations are also required to understand how the SOA regions perform when reverse-biased, and to determine how the switch will perform at different optical frequencies.

Next, the 2x2 and 4x4 switches described in Section 5 could be fabricated. To keep the layouts of these switches within a reasonable size, mirrors would have to be developed for the passive waveguiding material system. These mirrors could also perhaps be used for the 3dB power splitter to create a lower loss and compact design.

The performance of the power splitter (and therefore the switch) could be improved by either of two improvements in the passive waveguide material system:

- *Lower absorption coefficient* – The majority of the excess loss in the power splitter is a result of absorption loss in the passive waveguide. Since the device is relatively long (~3mm) any reduction in the loss coefficient of the passive waveguide would cause an appreciable decrease in the total loss of the device.
- *Greater mode confinement* – Since the zero-order mode of the passive waveguide is weakly confined (see Figure 31) the adiabatic tapers and bends are required to be very long. If the mode is more strongly confined, the size of the overall device could be shortened, resulting in a lower absorption loss.

It may also be possible to reduce the size and loss of the 3dB power splitter by using an MMI design, and this is a worthwhile improvement to investigate.

In the SOA region, greater modal confinement in the active layer of the device could improve the switch performance by increasing the overall modal gain or absorption. However, this could come at the cost of greater coupling loss and backreflections at the active/passive waveguide interface.

In conclusion, this thesis describes the design of a monolithically integrated 1x2 optical switch for use in ROADM devices. The vertically-integrated active/passive material system has been successfully used in this application, and it has been demonstrated that this proof-of-concept switch is worth developing and further optimizing. The pending fabrication and testing of this switch will provide valuable feedback on how to best improve upon this design.

7. References

1. M. Howard, "ROADM Equipment and Components Market Outlook," *Market Report by Infonetics Research*, February 2005.

2. OptiHS, Heterostructure simulation software, Optiwave Inc., 7 Capella Court, Ottawa, ON, Canada, K2E 7X1.

3. FEMLAB, Finite-element simulation software, COMSOL AB, 8 New England Executive Park, Burlington, MA, 01803.

4. K. Okamoto, *Fundamentals of Optical Waveguides*, Academic Press, San Diego, CA, 2000.

5. Z.J. Csendes and P. Silvester, "Numerical Solution of Dielectric Loaded Waveguides I - Finite-Element Analysis," *IEEE Trans. Microwave Theory Tech.*, vol. MTT-18, pp. 1124-1131, 1970.

6. T. Angkaew, M. Matsuhara, and N. Kumagai, "Finite-Element Analysis of Waveguide Modes – A Novel Approach that Eliminates Spurious Modes," *IEEE Trans. Microwave Theory Tech.*, vol. MTT-35, pp. 117-123, 1987.

7. B.M.A. Rahman, F.A. Fernandez, and J.B. Davies, "Review of Finite Element Methods for Microwave and Optical Waveguides," *Proc. IEEE*, vol. 79, pp. 1442-1448, 1991.

8. R. Scarmozzino, A. Gopinath, R. Pregla, and S. Helfert, "Numerical Modeling Techniques for Guided-Wave Photonic Devices," *IEEE J. Sel. Topics in Quantum Electron.*, vol. 6, pp. 150-162, 2000.

9. H.J.W.M. Hoekstra, "On beam propagation methods for modeling in integrated optics," *Opt. and Quantum Electron.*, vol. 29, pp. 157-171, 1997.

10. L. Vincetti, A. Cucinotta, S. Selleri, M. Zoboli, "Three-dimensional finite-element beam propagation method: assessments and developments," *J. Opt. Soc. Am. A*, vol. 17, pp. 1124-1131, 2000.

11. W.P. Huang and C.L. Xu, "Simulation of Three-Dimensional Optical Waveguides by a Full-Vector Beam Propagation Method," *IEEE. J. Quantum Electron.*, vol. 29, pp. 2639-2649, 1993.

12. V.I. Tolstikhin, A. Densmore, K. Pimenov, and S. Laframboise, "Single-Mode Vertical Integration of p-i-n Photodetectors with Optical Waveguides for Monitoring in WDM Transmission Systems," *IEEE Phot. Tech. Lett.*, pp. 843-845, 2003.

13. V.I. Tolstikhin, "Single-mode Vertical Integration of Active Devices within Passive Waveguides of InP-Based Planar WDM Components," *IPR '02 Technical Digest, IFC4-1 – IFC4-3*, 2002.

14. J.C. Palais, *Fiber Optic Communications, 4th ed.*, Prentice Hall, Upper Saddle River, NJ, 1998.

15. R. Prasanth *et. al.*, "Compact Polarization-Independent Mach-Zehnder Space Switch Combining Carrier Depletion and the Quantum Confined Stark Effect," *IEEE J. Quantum Elec.*, Vol. 39, 2003.

16. D.H.P. Maat, Y.C. Zhu, F.H. Groen, H. van Brug, H.J. Frankena, and X.J.M. Leijtens, "Polarization-Independent Dilated InP-Based Space Switch with Low Crosstalk," *IEEE Phot. Tech. Lett.*, vol. 12, pp. 284-286.

17. N. Izhaki and N.B. Horin, "Planar Lightwave Circuit (PLC) Switches Answer the Call for Next-Generation All-Optical Switching," *Lynx Photonic Networks White Paper*, 2002.

18. J.D. Burton, P.J. Fiddyment, M.J. Robertson, and P. Sully, "Monolithic InGaAsP-InP Laser Amplifier Gate Switch Matrix," *IEEE J. Quantum Electron.*, vol. 29, pp. 2023-2027, 1993.

19. W. van Berlo, M. Janson, L. Lundgren, A.-C. Morner, J. Terlecki, M. Gustavsson, P. Granestrand, and P. Svensson, "Polarization-Insensitive, Monolithic 4x4 InGaAsP-InP Laser Amplifier Gate Switch Matrix," *IEEE Phot. Tech. Lett.*,vol. 7, pp. 1291-1293, 1995.

20. S.S. Saini, P.J.S. Heim, R.E. Bartolo, F.G. Johnson, D. Stone, H. Shen, J. Pamulapati, W. Zhou, and M. Dagenais, "Mode Expanded Optical Switch in Resonant Vertically Coupled Waveguides," *IEEE Phot. Tech. Lett.*, vol. 11, pp. 1259-1261, 1999.

21. S.S. Saini, Y. Hu, F.G. Johnson, D.R. Stone, H. Shen, W. Zhou, J. Pamulapati, M.N. Ott, H.C. Shaw, and M. Dagenais, "Lossless 1x2 Optical Switch Monolithically Integrated on a Passive Active Resonant Coupler (PARC) Platform," *IEEE Phot. Tech. Lett.*, vol. 12, pp. 840-842, 2000.

22. S.S. Saini, F.G. Johnson, D.R. Stone, W. Zhou, H. Shen, and M. Dagenais, "A 2x2 Crosspoint Switch Fabricated on the Passive Active Resonant Coupler (PARC) Platform," *IEEE Phot. Tech. Lett.*, vol. 13, pp. 203-205, 2001.

23. K. Ishida *et al.*, "InGaAsP/InP optical switches using carrier-induced refractive index change," *Appl. Phy. Lett.*, vol. 50, pp. 141-142, 1987.

24. X.Q. Jiang, J.Y. Yang, H.Z. Zhan, K.J. Chen, Y. Tang, X.H. Li and M.H. Wang, "Photon-Induced Total-Internal-Reflection All-Optical Switches," *IEEE Phot. Tech. Lett.*, pp. 443-445, vol. 16, 2004.

25. K.-R. Oh *et al.*, "A Very Low Operation Current InGaAsP/InP Total Internal Reflection Optical Switch using p/n/p/n Current-Blocking Layers," *IEEE Phot. Tech. Lett.*, vol. 6, pp.65-67, 1994.

26. Y. Silberberg, P. Perlmutter, and J.E. Baran, "Digital Optical Switch," *Appl. Phys. Lett.*, vol. 51, pp. 1230-1232, 1987.

27. A. Sneh, J.E. Zucker, B.I. Miller, and L.W. Stulz, "Polarization-Insensitive InP-Based MQW Digital Optical Switch," *IEEE Phot. Tech. Lett.*, vol. 9, pp. 1589-1591, 1997.

28. S. Ng, S. Abdalla, P. Barrios, A. Delage, I. Golub, S. Janz, R. McKinnon, P. Poole, and B. Syrett, "Low current optical switching by carrier injection induced reconfigurable waveguiding," *Photonics North 2004*, [5579], Ottawa Congress Centre, September 26-29, 2004.

29. H.-M. Mak and H. Yanagawa, "High-Extinction Directional Coupler Switches by Compensation and Elimination Methods," *J. Lightwave Technol.*, vol. 12, pp. 899-908, 1994.

30. R.C. Alferness, "Polarization-independent optical directional coupler switch using weighted coupling," *Appl. Phys. Lett.*, vol. 35, pp. 748-750, 1979.

31. B.E. Little and Tom Murphy, "Design Rules for Maximally-Flat Wavelength-Insensitive Optical Power Dividers Using Mach-Zehnder Structures," *Phot. Tech. Lett.*, vol. 9, pp. 1607-1609, 1997.

32. L.B. Soldano and Erik C.M. Pennings, "Optical Multi-mode Interference Devices Based on Self-Imaging: Principles and Applications," *J. Lightwave Technol.* vol. 13, pp. 615-627, 1995.

33. M. Rajarajan, B.M.A. Rahman, and K.T.V. Grattan, "A Rigorous Comparison of the Performance of Directional Couplers with Multimode Interference Devices," *J. Lightwave Technol.* vol. 17, pp. 243-248, 1999.

34. T.A. Ibrahim, *et. al.*, "All-Optical Switching in a Laterally Coupled Microring Resonator by Carrier Injection," *IEEE Phot. Tech. Lett.*, vol. 5, 2003.

35. V.I. Tolstikhin, F. Wu, Y. Logvin, A. Densmore, K. Pimenov, S. Grabtchak, "InP-based photonic integrated circuits for optical performance surveillance, signal conditioning and bandwidth management in WDM transmission systems," *Photonics North 2004*, [5579C-78], Ottawa Congress Centre, September 26-29, 2004.

36. A. Takagi, K. Jinquji, and M. Kawachi, "Design and Fabrication of Broad-band Silica-Based Optical Waveguide Couplers with Asymmetric Structure," *IEEE J.Quantum Electron.*, vol. 28, pp. 848-855, 1992.

37. K. Kishioka, "A design method to achieve wide wavelength-flattened responses in the directional coupler-type optical power splitters," *J. Lightwave Technol.*, vol. 19, pp. 1705-1715, 2001.

38. K. Morishita, M.S. Yataki, and W.A. Gambling, "Wavelength-insensitive couplers using dispersive materials," *Opt. Lett.*, vol. 12, pp. 534-535, 1987.

39. M. Kuznetsov, "Radiation loss in dielectric waveguide y-branch structures," *J. Lightwave Technol.* vol. LT-3, pp. 674-677, 1985.

40. O. Hanaizumi, M. Miyagi, and S. Kawakami, "Wide y-junctions with low losses in three-dimensional dielectric optical waveguides," *IEEE J. Quantum Electron.*, vol. QE-21, pp. 168-173, 1985.

41. S. Safavi-Naeini, Y. Chow, S. Chaudhuri, and A. Goss, "Wide angle phase-corrected y-junction of dielectric waveguides for low loss applications," *J. Lightwave Technol.* vol. 11, pp. 567-576, 1993.

42. H. Lin, J.-Y. Su, R.-S. Cheng, and W.-S. Wang, "Novel optical single-mode asymmetric y-branches for variable power splitting," *IEEE J. Quantum Electron.*, vol. 35, pp. 1092-1096, 1999.

43. T. Yabu, M. Geshiro, and S. Sawa, "New design method for low-loss y-branch waveguides," *J. Lightwave Technol.* vol. 15, pp. 1376-1384, 2000.

44. S.-L. Tsao and Chun-yi Lu, "BPM Simulation and Comparison of 1x2 Directional Waveguide Coupling and Y-Junction Coupling Silicon-on-Insulator Optical Couplers," *Fiber and Integrated Optics*, vol. 13, pp. 373-379, 1994.

45. P.A. Besse, M. Bachmann, H. Melchior, L.B. Soldano, and M.K. Smit, "Optical Bandwidth and Fabrication Tolerances of Multimode Interference Couplers," *J. Lightwave Technol.*, vol. 12, pp. 1004-1009, 1994.

46. G.V. Eleftheriades, A.S. Omar, L.P.B. Katehi, and G.M. Rebeiz, "Some Important Properties of Waveguide Junction Generalized Scattering Matrices in the Context of the Mode Matching Technique," *IEEE Trans. on Microwave Theory and Tech.*, vol. 42, 1994.

47. MATLAB, Mathematical processing software, COMSOL AB, 8 New England Executive Park, Burlington MA, 01803.

48. B. Jalali, M. Yegnanarayanan, Y. Yoon, T. Yoshimoto, I. Rendina, and F. Coppinger, "Advances in Silicon-on-Insulator Optoelectronics," *IEEE J. Sel. Topics Quantum Electron.*, Vol. 4, pp. 938-947, 1998.

49. R. Millett, H.P. Schriemer, X. Zhang, and M. Cada, "Irrelevance of bending angle in simple Y-branch power splitter design," *Photonics North 2004*, [5577-64], Ottawa Congress Centre, September 26-29, 2004.

50. OptiBPM 6.1.0.328, Waveguide simulation software, Optiwave Inc., 7 Capella Court, Ottawa, ON, Canada, K2E 7X1.

51. X. Zhang, Centre for Research in Photonics, University of Ottawa, *Private communication*, 2004.

52. M.K. Smit, Erik C.M. Pennings, and Hans Blok, "A Normalized Approach to the Design of Low-Loss Optical Waveguide Bends," *J. Lightwave Technol.* vol. 11, pp. 1737-1742.

53. V. Ramaswamy and P.G. Suchoski, Jr., "Power loss at a step discontinuity in an asymmetrical dielectric slab waveguide," *J. Opt. Soc. Am. A.*, 1, pp. 754-759, 1984.

54. A. Yariv, *Optical Electronics in Modern Communications, 5th ed.*, Oxford University Press, New York, NY, 1997.

55. B.R. Bennett, R.A. Soref, and J.A. del Alamo, "Carrier-Induced Change in Refractive Index of InP, GaAs, and InGaAsP," *IEEE J. Quantum Electron.*, vol. 26, pp. 113-122, 1990.

56. J. Taylor, Centre for Research in Photonics, University of Ottawa, *Private communication*, 2004.

57. C. Clos, "A Study of Non-Blocking Switching Networks," *Bell. Sys. Tech. J.*, pp. 406-424, Mar. 1953.